



CZECH TECHNICAL UNIVERSITY IN PRAGUE

Faculty of Civil Engineering

Department of materials engineering and chemistry (K123)

**Magnesium-based and lime-based composites
containing layered nanomaterials**

DOCTORAL THESIS

Ing. Adam Pivák

Doctoral study programme: P0732D260006 - Physical and material engineering

Doctoral thesis tutor: Prof. Ing. Milena Pavlíková, Ph.D.

Prague, 2024



DECLARATION

Ph.D. student's name: Ing. Adam Pivák

Title of the doctoral thesis: Magnesium-based and lime-based composites containing layered nanomaterials

I hereby declare that this doctoral thesis is my own work and effort written under the guidance of the tutor Prof. Ing. Milena Pavlíková, Ph.D.

All sources and other materials used have been quoted in the list of the references.

The doctoral thesis was written in connection with research on the projects:
GA19-00262S; GA20-01866S; GA23-04744S; SGS20/153/OHK1/3T/11;
SGS23/149/OHK1/3T/11; CZ.02.2.67/0.0/0.0/16_016/0002526;
CZ.02.1.01/0.0/0.0/16_017/0002623.

In Prague on

.....
Signature

Acknowledgments

First and foremost, I would like to express my gratitude to my thesis supervisor Prof. Ing. Milena Pavlíková, Ph.D. for her guidance, consultation, advice and above all patience during my studies and work.

I would also like to thank Prof. Ing. Zbyšek Pavlík, Ph.D. and Ing. Martina Záleská, Ph.D. and others for their valuable advice and research guidance. I would also like to thank other colleagues from the Department of Materials Engineering and the Faculty of Civil Engineering for their cooperation.

I must not forget to thank Prof. Ing. Ondřej Jankovský, Ph.D. and his team from the Department of Inorganic Chemistry, UCT Prague for their cooperation in the research projects mentioned below.

Finally, I would like to thank my family and friends for their support throughout my studies, thank you all.

I gratefully acknowledge the support provided:

by Czech Science Foundation projects No.:

GA19-00262S - Reactive magnesia cements-based composites with selected admixtures and additives

GA20-01866S - High-performance composites containing layered nanomaterials

GA23-04744S - Research of heavy metals immobilization in alternative low-carbon composites

by Grant Agency of the Czech Technical University in Prague projects No.:

SGS20/153/OHK1/3T/11 - Development of Advanced Building Materials

SGS23/149/OHK1/3T/11 - Research and development of high performance building composites

by MŠMT OPVVV project support No.:

CZ.02.2.67/0.0/0.0/16_016/0002526 - Obnova infrastruktury laboratoří Stavební fakulty ČVUT

CZ.02.1.01/0.0/0.0/16_017/0002623. „Vytvoření infrastruktury pro inovované doktorské studijní programy Fyzikální a materiálové inženýrství (CZ/ENG)

by Civil Engineering - Scanning Electron Microscope Laboratory, CTU Prague (CE-SEM Lab).

Abstract

At the beginning of the 21st century, nanomaterials have become a research topic because of the possibilities of their application. Today, the most prominent are carbon-based nanomaterials. Many differently shaped 0D, 1D, and 2D nanomaterials were discovered and analysed. Their unique transport, chemical, and mechanical properties found application in nanotechnology, electronics, optics, and other fields of material science. It was demonstrated that carbon-based nanomaterials have a strong reinforcing ability. However, most of the research focused on strength enhancement in cement-based composites, while the possible use of nanomaterials in magnesium-based or lime-based mortars was scantily reported. This thesis focusses on the material properties of mortars and pastes based on reactive magnesia and standardized lime-based mortars. Studies on the technology of nanomaterial application were conducted and mixtures were designed, which were then subjected to measurements of basic micro and macro structural characteristics, mechanical resistance, thermal properties, and water absorption parameters. In the context of composite materials, in the form of pastes and mortars, nanomaterials have been found to have a positive effect, especially on mechanical characteristics. But it is important to determine the optimum size and application procedure of the nano-additive, because inappropriate mixing and applied volume resulted in deterioration of the properties. Based on the results, it was concluded that the use of nano-additives has significant potential in the design and development of advanced composite pastes and mortars with higher performance.

Keywords: *nanomaterials; nano-additive; natural hydraulic lime; lime hydrate, magnesium oxychloride cement;*

Table of Contents

Abbreviations.....	11
Symbols	12
1 Introduction.....	13
2 State of the art	17
2.1 Classification of Nanomaterials	18
2.1.1 Nanomaterial Origin	18
2.1.2 Nanomaterial Dimensionality	19
2.1.3 Nanomaterial Composition	20
2.2 Carbon-based Nanomaterials	20
2.2.1 Graphene	21
2.2.2 Carbon Nanotubes	24
2.2.3 Carbon Nanospheres	28
2.3 Nano-enhanced Composite Materials	28
2.3.1 Nanomaterial Dispersion Technique.....	30
2.3.2 Nanomaterial Chemical Functionalization.....	32
2.3.3 Concentration of Nano-additive	35
3 Main Aims of Doctoral Thesis.....	41
4 Experimental.....	43
4.1 Used Materials	44
4.1.1 Binders.....	44
4.1.2 Aggregate.....	45
4.1.3 Carbon-based Nanomaterials.....	46
4.1.4 Stabilising Chemical Agents	48
4.1.5 Antifoamer.....	50
4.2 Sample Composition and Preparation Methods	51
4.2.1 High-purity MOC.....	51
4.2.2 High-purity MOC – Sample Preparation	55
4.2.3 Standardized Mortars	56
4.2.4 Standardized Mortars – Composite Design	63
4.2.5 Standardized Mortars – Sample Preparation.....	66
4.3 Experimental Tests	68
4.3.1 Raw Material Characteristics	68
4.3.2 Nanomaterial Suspension Characteristics	72
4.3.3 Characteristics of Fresh and Hardened Mortar and Pastes	74
4.3.4 Material Characteristics Analysis.....	76
4.3.5 Mechanical Strength Analysis.....	79
4.3.6 Thermophysical Properties	82
4.3.7 Water Absorption Characteristics	82
4.3.8 Cost-Effectivity of Nano-Additive	84
5 Results and Discussion	85
5.1 High purity MOC	86
5.1.1 Influence of the Two-step Homogenisation Technique	86

5.1.2	Influence of NM's Specific Surface Area.....	95
5.1.3	Influence of NM's Volume.....	102
5.1.4	Combination of 1D and 2D Nano-additives.....	110
5.1.5	Carbon Spheres Nano-additive	115
5.2	Standardized Mortars.....	121
5.2.1	Magnesium Oxychloride Cement Mortars (MOC)	121
5.2.2	Hydrated Lime Mortars (CL)	127
5.2.3	Natural Hydraulic Lime Mortars (HL)	132
6	Conclusion	141
	References	145
	List of Figures.....	164
	List of Tables.....	168
	List of published papers within the researched projects.....	170

Abbreviations

0D	Zero-dimensional
1D	One dimensional
2D	Two-dimensional
3D	Three-dimensional
CAS	Czech Academy of Sciences
CBN	Carbon black nanoparticles
CL	Calcium Lime
CNs	Carbon nanospheres
CSs	Carbon spheres
EDS	Energy dispersive spectroscopy
GHG	Greenhouse gas
GNs	Graphene nanoplatelets
GO	Graphene Oxide
HL	Hydraulic Lime
MIP	Mercury intrusion porosimetry
MOC	Magnesium Oxychloride Cement
MWCNTs	Multi-walled Carbon nanotubes
NHL	Natural Hydraulic Lime
NMs	Nanomaterials
NPs	Nanoparticles
NsM	Nano-structured Materials
PC	Portland Cement
PVP	Polyvinyl Pyrrolidone
rGO	Reduced Graphene Oxide
Rpm	Rounds per Minute
SDBS	Sodium Dodecyl Benzene Sulphonate
SDC	Sodium Deoxycholate
SDS	Sodium Dodecyl Sulphate
SEM	Scanning electron microscopy
SP	Superplasticizer
STM	Scanning Tunnelling Microscope
SWCNTs	Single-walled Carbon nanotubes
TEM	Transmission electron microscopy
TPS	Transient plane source
XRF	X-Ray fluorescence
p.a.	Pro analysis

Symbols

ω	Rotational speed	(rpm)
ρ_s	Loose bulk density	($\text{kg}\cdot\text{m}^{-3}$)
ρ_{mat}	Specific density	($\text{kg}\cdot\text{m}^{-3}$)
SSA	Specific surface area	($\text{m}^2\cdot\text{kg}^{-1}$, $\text{m}^2\cdot\text{g}^{-1}$)
ρ_v	Bulk density	($\text{kg}\cdot\text{m}^{-3}$, $\text{g}\cdot\text{cm}^{-3}$)
m	Mass	(kg)
V	Volume	(m^3)
Ψ	Total open porosity	(%)
Ψ_{Hg}	Porosity from MIP analysis	(%)
F	Maximum force	(N)
l	Support span	(mm)
b,h	Dimensions of sample	(mm)
f_f	Flexural strength	(MPa)
f_c	Compressive strength	(MPa)
v	Ultrasonic wave velocity	($\text{m}\cdot\text{s}^{-1}$)
t	Time	(s)
E	Dynamic modulus of elasticity	(GPa)
λ	Thermal conductivity	($\text{W}\cdot\text{m}^{-1}\cdot\text{K}^{-1}$)
C	Volumetric heat capacity	($\text{J}\cdot\text{m}^{-3}\cdot\text{K}^{-1}$)
A_w	Water absorption coefficient	($\text{kg}\cdot\text{m}^{-2}\cdot\text{s}^{-1/2}$)
m_{24h}	Weight at 24-hour water absorption	(kg)
m_{dry}	Weight in dry state	(kg)
W_a	24-hour water absorption	($\text{kg}\cdot\text{m}^{-2}$)
CPU	Cost per unit	(€)
$f_{control}$	Reference strength value	(kPa)
$f_{enhanced}$	Enhanced strength value	(kPa)

1 Introduction

Nanomaterials (NMs) are a modern type of materials that have been at the forefront of the researchers nowadays. The prefix “nano” originated from the Latin word “nanus”, which means dwarf or markedly small person. Since NMs can be created by natural processes on Earth, evidence of their use can be found as far back as Ancient times or even in the prehistoric era. The very use of fire is the manufacture of nanoparticles in smoke or soot, which was used for cave paintings.

In ancient Egypt, oil lamp soot was used to prepare black pigment for writing. The first traces of metallic NMs were traced back to the 14th century BC in Egypt and Mesopotamia. The red glass manufactured contained nanoparticles of copper (Cu). Mesopotamian pots also contained Cu which produces a glistening effect on the surface. Another example might be the Roman Lycurgus cup made of glass containing silver (Ag) and gold (Au) nanoparticles, which change its colour to green or red-purple when the glass is illuminated directly or the light passes through the glass. Despite the historical use of natural NMs, significant advances were not made until the 19th century in the study and manufacture of nanomaterials [1, 2].

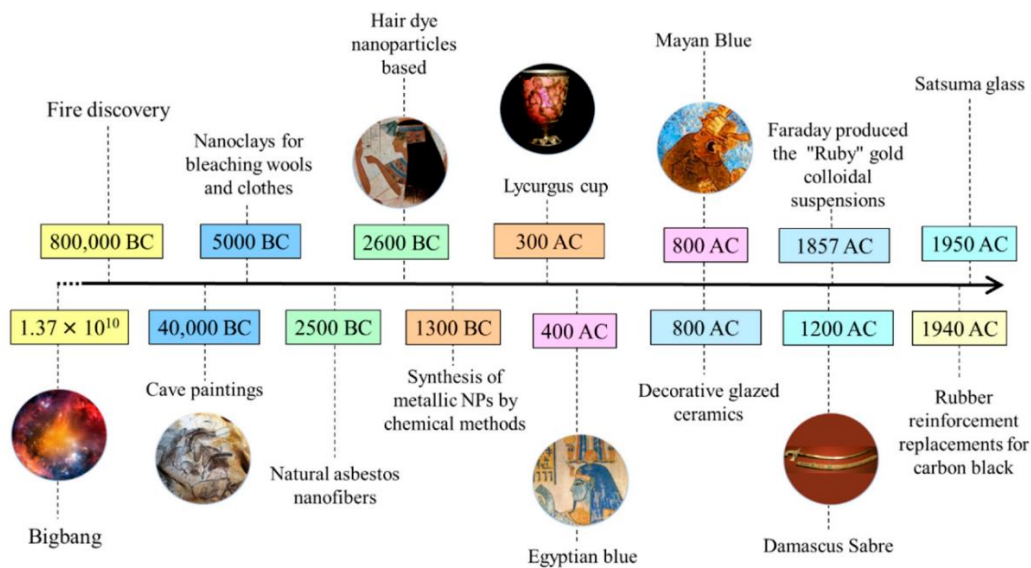


Figure 1: Timeline summarising the use of nanomaterials during ancient times [2].

The technology had developed to the extent that scientists could study materials in scales smaller than 1 μm with the invention Transmission Electron Microscopy (TEM) in 1931 by Ernest Ruska and Max Knoll. In 1959, following this development, Richard P. Feynman presented the vision of studying material structures at the atomic level combined with technology, which could freely manipulate individual atoms and arrange them in specific structures to change and improve material properties [3]. The visions of the possible arrangement of the material's atoms became real in 1990, when scientists Donald M. Eigler and Erhard Schweizer of IBM's Almaden Research Centre

(International Business Machines) were able to move xenon atoms across the single-crystal nickel surface using a scanning tunnelling microscope (STM). The test resulted in the construction of an atomic model of the IBM logo composed of 35 xenon atoms [4], as shown in Fig. 2.

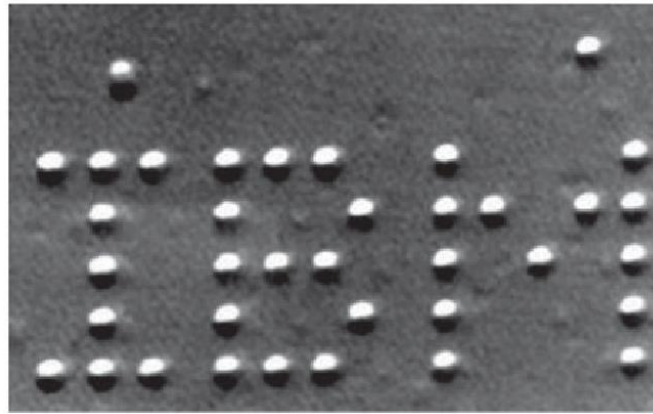


Figure 2: SEM image of the IBM logo composed of xenon atoms [5].

As the requirements on the properties of construction materials grow, the building industry is focussing on the potentially promising incorporation of NMs into building materials and improving their characteristics. In civil engineering, there are several studies focused on improving the mechanical performance of building composites, mostly concrete, by incorporating various types of nano-additives. However, application into other types of building materials, for instance, to magnesium-based and lime-based mortars, was rarely reported. Moreover, given the quantity of applicable combinations of nanomaterial basis, types, volumes, and incorporation techniques, the application into different types of building materials must be appropriately selected and the effect of nano-additive should be properly evaluated to identify the optimum combination of all aspects. Furthermore, while the nano-additive may improve mechanical strength in some cases it may deteriorate the strength properties, as well as structural or thermal characteristics.

This work focusses on the application of graphene nanoplatelets (GNs), multi-walled carbon nanotubes (MWCNTs), and carbon nanospheres (CNS) into mortars based on light-burnt magnesia, natural hydraulic lime, and hydrated lime. The aim is to determine the optimum procedure for the application of different volumes of these nanomaterials in mortars and their influence on the material properties to obtain the best possible combination of the nanomaterial and mortar type.

2 State of the art

2.1 Classification of Nanomaterials

NMs are materials reaching dimensions close to the size of atoms, i.e., 10^{-9} m, or nanometres. This assumption has become a common description of this type of material worldwide. According to the 2011 European Commission Recommendation [6], a nanomaterial is defined as “natural, incidental or manufactured material containing particles, in an unbound state or as an aggregate or as an agglomerate and where, for 50% or more of the particles in the number size distribution, one or more external dimensions is in the size range 1nm - 100nm.” Although there is no regulation or legislation that specifies the parameters of materials that can be identified as NMs, industry and researchers around the world have unified the categories to distinguish materials with different origins, shapes, and other characteristics, which is appropriate for further study and improvement of nanomaterial science.

2.1.1 Nanomaterial Origin

On the basis of their origin, the NMs can be described as naturally occurring, incidental, engineered, or bioinspired nanoparticles. Natural nanomaterial formation is caused by natural physio-chemical processes that occur on the Earth [2], such as mechanical erosion, thermal combustion, chemical (nucleation), and photochemical reactions (sunlight). The natural sources of NMs are included in all earth spheres, for example, the troposphere, soils, rocks, and lava from the lithosphere, lakes, and groundwaters in the hydrosphere or biosphere [7, 8].

Engineered nanoparticles are intentionally synthesised in laboratory conditions by controlled chemical, physical, and biological processes inspired by natural processes. Manufactured NM can be produced with specific characteristics and controlled chemical purity comparable to or exceeding the properties of natural NM [2, 9].

Incidental nanoparticles are nanoparticles manufactured as a by-product or waste material during industrial manufacturing and mechanisation or unintentional processes of everyday living that have an impact on the environment and human health. Among those nanomaterials are, for example, carbon-based particles, metal nanoparticles, or nanoplastics released by traffic exhaust fumes, due to abrasion or metal corrosion [10, 11].

2.1.2 Nanomaterial Dimensionality

Due to the wide variety of manufacturing methods used to produce NMs in different shapes, the morphology and dimensional characteristics must be taken into consideration, as it highly affects the final material characteristics and possible application. Therefore, the NMs were characterised and classified by dimensionality [2, 12]:

1. Zero-dimensional nanoparticles (0D-NPs): This category covers materials with dimensions less than 100 nm, i.e. nanoparticles or nanoclusters. They can be amorphous, single-crystalline, or polycrystalline, composed of single or multiple elements. NPs in higher-dimension categories are manufactured by modification and shaping of 0D-NPs.
2. One-dimensional nanoparticles (1D-NPs): NPs with two dimensions shorter than 100 nm fall into this category, i.e. nanotubes, nanofibers, nanowires, and nanorods.
3. Two-dimensional nanoparticles (2D-NPs): In this category, only thicknesses reached nanometre scales and include nanofilms, nanosheets, and nanoribbons.
4. Three-dimensional nanoparticles (3D-NPs): Nanomaterials are generally known as bulk NMs that have all three dimensions beyond 100nm, such as bulk solids, nanocomposites, or nanocrystalline materials.

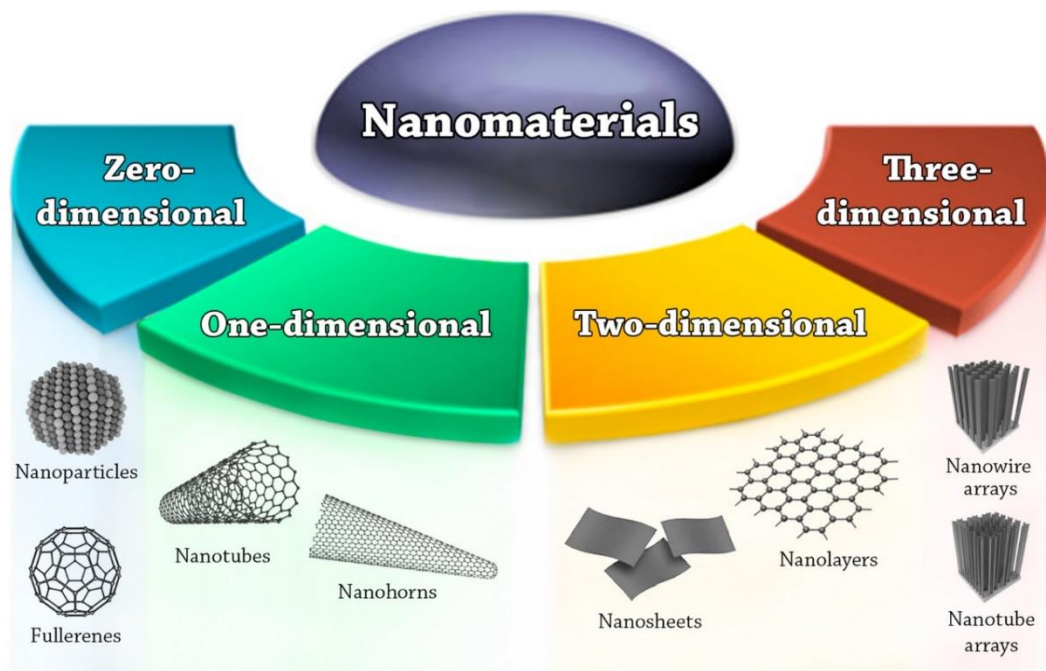


Figure 3: Dimensionality classification of nanostructures [12].

2.1.3 Nanomaterial Composition

The particles originating from natural and engineered processes represent a wide spectrum of elements and compounds that fall into four groups [7, 8, 13]:

1. Inorganic-based nanomaterials: This group covers naturally obtained and engineered metal oxides, for example silica (SiO_2), ferric oxide (Fe_2O_3), aluminium oxide (Al_2O_3), titanium dioxide (TiO_2), metals and alloys, such as silver (Ag), copper (Cu), zinc (Zn) or pyrite (FeS_2) and silver sulphide (AgS) as part of metal sulphides.
2. Organic-based nanomaterials: These NMs are made mostly from organic matter, including lipids (e. g. lecithin, stearic acid) and polymers (for instance, alginate, chitosan, or Hydroxymethyl cellulose). Carbon-based nanomaterials are excluded from this category.
3. Carbon-based nanomaterials: It is a large group of NMs composed of carbon particles. This category is further divided by its dimensionality and morphology. Widely known instances are fullerenes, carbon nanofibers (CNFs), carbon nanotubes (CNTs), graphene oxide (GO), and graphite oxide (GRO).
4. Composite-based nanomaterials: This category covers all possible combinations of multiple phases of NMs. For instance, combination of metal-based with organic-based or carbon-based materials, combination of materials with different morphology. This category also includes multiphase materials composed of multiple NMs or composites consisting of nanoscale-sized NM with a larger or bulk-type material.

2.2 Carbon-based Nanomaterials

The most prominent types of materials studied today are NMs based on carbon particles. For example, natural graphene is a potentially ecofriendly and sustainable solution to material modifications [14]. Because of the unique conductive, chemical and mechanical properties of carbon-based NMs, they found application in nanotechnology, electronics, optics, or other fields of material science. A large number of differently shaped 0D, 1D, and 2D nanomaterials were discovered and analysed, such as fullerenes, graphitic onions, nanohorns, graphene, graphite oxides, and nanotubes. This study is focused on graphene nanoplatelets (GNs), multi-walled carbon nanotubes (MWCNTs) and carbon nanospheres (CNs).

2.2.1 Graphene

Graphene, graphene oxides and graphite oxides (exfoliated graphite oxide) are part of the 2D-NPs group. All formed by pure carbon atoms arranged in a single layer of one atom thick that forms a hexagonal (honeycomb) lattice, shown in Fig. 4. with lateral dimension in the size range exceeding 100 nm.

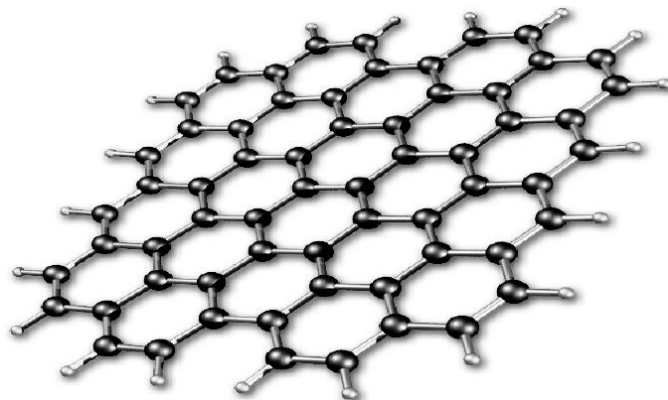


Figure 4: Schematic of hexagonal graphene lattice [15].

Graphene has high tensile strength, approx. 130 GPa, Young's modulus of elasticity 1000 GPa [14], and a very high surface area, reaching $2630 \text{ m}^2\cdot\text{g}^{-1}$. Carbon atoms of graphene are bonded with covalent sp^2 -bonds with a single free electron, which can move only in two dimensions and is forbidden from leaving the graphene plane [4]. These electrons have high electron mobility at room temperature, which affects the electrical conductivity of the material [14]. Which is approx. $6500 \text{ S}\cdot\text{m}^{-1}$ [16]. However, conductivity is highly dependent on the method of preparation of graphene [17]. Graphene has several applicability options, for instance its use as an additive for anticorrosive coatings [17] or as an active layer in solar cells [18].

Despite the excellent properties of graphene, the applicability and stability of a single-layer pure carbon sheet is limited due to the difficulty in homogenising it into the matrix of the material because it forms large-scale structures [19], due to agglomeration or poor solubility. However, graphene can be modified with oxygen-based functional groups.

Graphene is synthesised using a broad spectrum of methods, generally divided into two main types of route, the 'top-down' and 'bottom-up' route. The top-down route includes all destructive methods which produce graphene layers, namely mechanically or chemically induced exfoliation and reduction of large starting material. Another method, the bottom-up route, is based on the assembly of graphene layers from smaller carbonaceous elements. This includes chemical vapour deposition (CVD), epitaxial growth, and other methods [20, 21].

2.2.1.1 Top-down Route

Mechanical exfoliation:

Mechanical exfoliation represents the use of mechanical force in natural graphite, single-crystal graphite, or highly orientated pyrolytic graphite. The graphene layers are then peeled due to normal or lateral forces that overcome van der Waals forces, typically around $300 \text{ nN}\cdot\mu\text{m}^{-2}$. Mechanical exfoliation methods differ in their dependence on a particular peeling procedure caused by different sources of mechanical force [21].

Micromechanical cleavage, also known as the Scotch tape method, is based on the recurrent cleaving of the pyrolytic graphite top layers using the adhesive tape. The adhesion of graphene to the tape is stronger than the van der Waals forces between the graphene layers, and the tape could be peeled off with multiple graphene layers remaining on it. Repeating this process will further thin the graphene layers until a few-layer or single-layer graphene with high quality and almost no defects is obtained. This method is technically easy; however, the production rate of this method is low and is used only for fundamental scientific tests rather than commercial purposes [20, 21].

Exfoliation is also possible with explosive force. The shockwave energy applied to graphite is sufficient to rapidly dissociate approximately 10 layers thick graphene sheets. The evaluation of the magnitude of the applied force is crucial for this method. If the explosion is uncontrolled and the magnitude is much higher, the resulting graphene sheets can be damaged [21, 22].

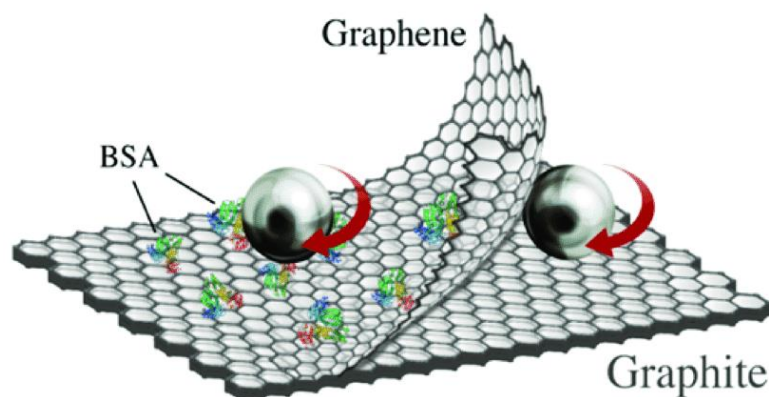


Figure 5: Exfoliation of graphene sheets [23].

For the commercial production of few-layer graphene, the continuous mechanical cleavage method is more promising. Exfoliation can be conducted, for instance, by grinding with balls [22] grinding [24] or by oscillating with ultra-sharp wedge grinding [25]. The first instance is based on a common powder milling method, which involves breaking down graphite layers in the dry state in an isolated environment due to oxidation of

graphene, or in the wet state in solution with solvents. In the second instance, graphite and adhesive are placed between rolls, and the exfoliation is caused by shear forces.

Although this method is faster, it is more difficult to separate milled graphene sheets from residual adhesives. The latter example is based on the sectioning method used in biological sample preparations. The small piece of pyrolytic graphene is mounted in epoxy resin and the cleaved with a diamond wedge with a sharpness of less than 20 and an angle of 35 °.

Chemical exfoliation:

Compared to mechanical exfoliation, chemical exfoliation reaches higher productivity. The method is based on the intercalation of the compound particles between the graphene layers and their subsequent separation. Chemical exfoliation methods are considered for liquid phase exfoliation (LPE) and supercritical fluid exfoliation.

In the LPE technique, graphite is dispersed in ionic liquids or water with a surfactant or polymer additive and then sonicated. There are two effects that overcome the interlayer forces of graphene and break the graphene layers from each other during sonication, namely shear forces and cavitation. The surfactants are then adsorbed in the graphene layer plane, which prevents flocculation and stabilises the suspension when sonication ends [21, 26].

The supercritical fluid exfoliation technique utilises the expanding effect of supercritical fluids, the substance in conditions above its critical temperature and pressure, in saturated graphite. The fluid, most commonly CO₂, is pressurized and intercalated between the graphene layers during sonication. Then the pressure of the substance decreases, the supercritical CO₂ reverts to its subcritical state, expands and forces rapid separation of the graphite layers. Both techniques are suitable for high-yield production of graphene. The only downside is the use of chemicals necessary for suspension stabilisation [21, 27].

Electrochemical exfoliation:

The last commonly used method is electrochemical exfoliation. The electrochemical method is based on an electrolytic process. The experimental setup contains a dilute mineral acid or aqueous salt as the electrolyte, a working electrode composed of pyrolytic graphene, a platinum wire counter electrode, a reference electrode, and a power supply. An electric current causes the movement of ions in the electrolyte and attracts them into the interlayer space of graphite. Intercalated ions increase the interlayer spacing between graphene sheets and cause subsequent exfoliation. The electrochemical exfoliation method has high productivity at lower costs, with no additional purification of

the final product [28, 29]. Additionally, it is possible to functionalise graphene during its synthesis and is considered a 'one-pot approach' to GO production [21].

2.2.1.2 Bottom-up Route

Epitaxial growth:

Method of low-scale production with controlled number of layers for electronic applications. Silicon carbide (SiC) is heated under vacuum conditions or in an inert atmosphere to high temperatures (more than 1400 °C) when Si is evaporated while the remaining carbon is rearranged to form a thin graphene film [21, 30]. Furthermore, thermal decomposition of ethylene to produce high-purity graphene is also possible [20].

Chemical vapour deposition (CVD):

CVD is the most widely used method to produce high-quality, large-area graphene. Chemically reactive hydrocarbon gas is pumped into a reactor where various chemical reactions are performed in a controlled environment. The type of reactions is highly dependent on reactor setup, environment temperatures and pressures, gas intake ratio, etc. [31]. The solid products of the chemical reaction, namely graphene sheets or carbon nanotubes, are deposited on the metal substrate, commonly nickel (Ni) or copper (Cu) [32], while other by-products and gases are drawn out of the reactor [33]. The main advantages of CVD are its low-cost and potentially eco-friendly production with easy experimental setup [34, 35].

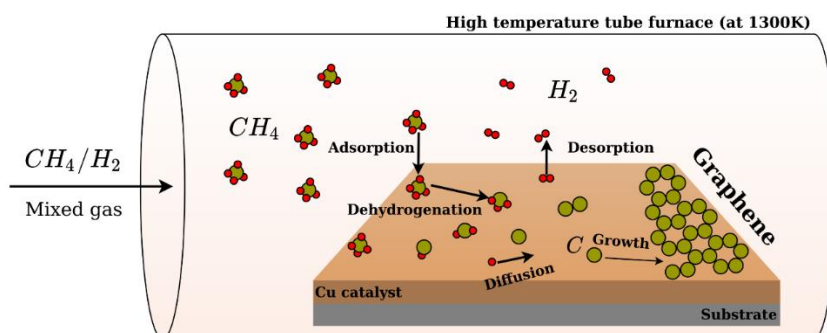


Figure 6: Example of the CVD procedure for graphene synthesis [36].

2.2.2 Carbon Nanotubes

Carbon nanotubes (CNTs) are cylindrical shaped 1D-NMs with hollow inner structure and a surface with hexagonal arrangement of atoms, similar to graphene, discovered in the year 1991 [37]. According to the structural formation, CNTs can be composed of one

graphene layer only or multiple layers (Fig.7). CNTs with single layer, named single-wall carbon nanotubes (SWCNTs), reach a diameter between 0,4 and 3 nm and a length exceeding 100 nm, even up to a few μm . Double-walled carbon nanotubes (DWCNTs) and multi-walled carbon nanotubes (MWCNTs) are composed of more than one rolled sheet of graphene. The diameter of the hollow inner tube is between 0.34 nm and 3 nm wide, and the outer diameter diverges from 2 to 100 nm depending on the number of layers with interlayer distance greater than 3 Å wide. The structures of DWCNTs and MWCNTs can be further specified into two categories depending on the number of graphene sheets used for the formation of CNTs. If every CNT layer is constructed using a separate graphene sheet, it is called the 'Russian doll' model. Simply put, one thinner tube is inside another tube with a larger diameter. The second model refers to multiple layers made of a single larger graphene sheet which is basically rolled and wrapped around itself. This is called the 'parchment' model [37–39].

The CNTs have extraordinary properties to graphene, from which the nanotube is made, and orientation of hexagonal carbon lattice with respect to the rolling axis of the graphene sheet. The change in rolling axis affects the arrangement of carbon atoms in the cross section of CNT. Final structures can be chiral, armchair, or zigzag structure [40].

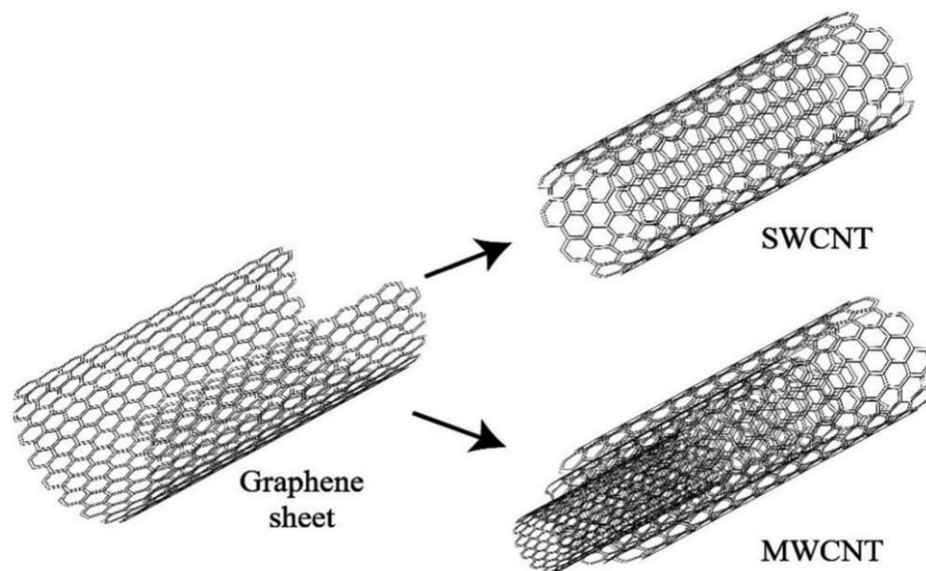


Figure 7: Example of the CVD procedure for graphene synthesis [41].

According to studies, the specific range differs considerably between SWCNTs ($400\text{--}900\text{ m}^2\cdot\text{g}^{-1}$) and MWCNTs ($200\text{--}400\text{ m}^2\cdot\text{g}^{-1}$). There is also a difference in mechanical strength which ranges from 50 to 500 GPa and modulus of elasticity around 1,4 TPa in the case of SWCNTs while the strength of MWCNTs ranges from 10 to 60 GPa with

modulus of elasticity up to 1 TPa. On the other hand, both SWCNTs and MWCNTs have nearly the same electrical conductivity, approximately $100 \text{ S}\cdot\text{cm}^{-1}$ [39].

2.2.2.1 Carbon Nanotube Synthesis

Although graphene sheets can be obtained naturally or synthesised using methods based on natural events, the CNT can be obtained only by chemical reactions using a laboratory setup. There are three main, commonly used CVD synthesis methods, laser ablation, and the arc-discharge technique. All three methods are used to produce both SWCNTs, with the addition of a catalyst (Fe, Co, or Ni), and MWCNTs without any addition [42]. The most used method, CVD, is described in a previous chapter. Among advantages, in addition to the above mentioned, is also the control of CNT growth. With the right experimental setup, the specific procedure and substrate, it is possible to grow CNTs in specific alignment or multiple directions simultaneously, as shown in Fig. 8 [43].

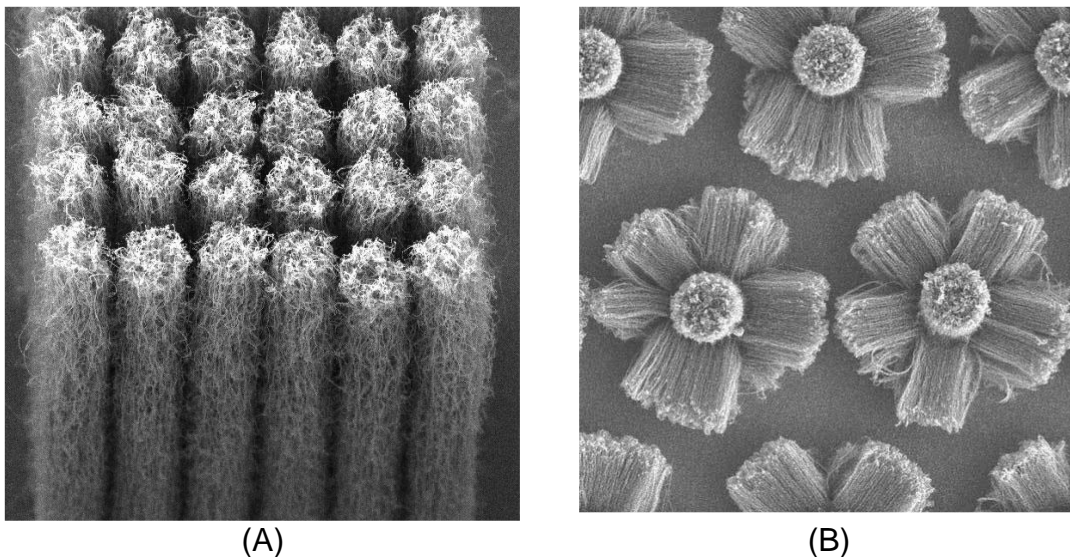


Figure 8: Controlled nanotube structures: A) aligned CNT arrays; B) 3D MWCNT pattern – Daisies [43].

Electric-arc discharge:

The oldest of the methods mentioned above is an electric-arc discharge method. The setup consists of two graphite electrodes separated with a 1mm gap between them in a chamber filled with inert gas and a power source to generate a direct power current, which produces an electric arc between graphite electrodes. The arc ionises carbon atoms of the pure carbon anode and produces carbon cations and plasma. These cations are moved to the cathode and, through reduction and deposition, grow as CNTs on it.

As the CNT grows, the electrodes move to always retain the 1 mm gap between the electrodes. This method will ensure the production of MWCNTs and SWCNTs with the use of catalyst nanoparticles (Fe, Co, and Ni). Further purification is needed to obtain the pure form of CNT [37, 41, 43].

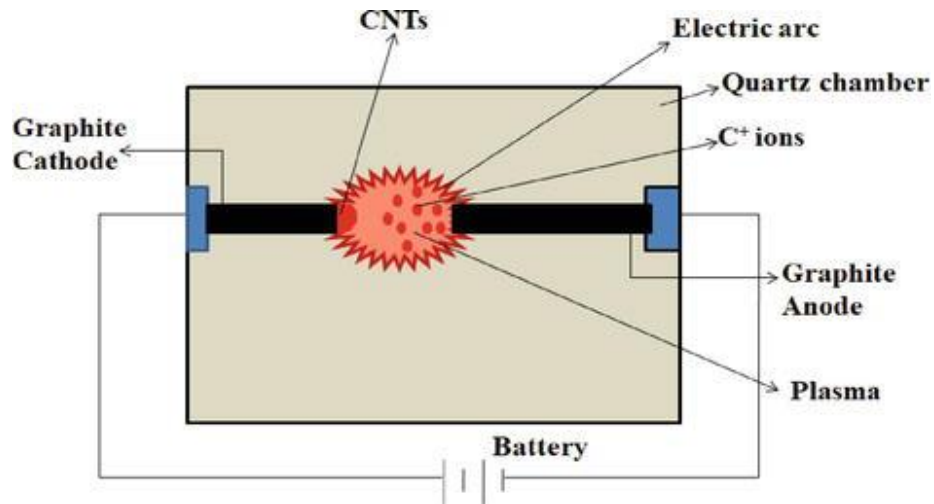


Figure 9: Scheme of the electric-arc method [42].

Laser ablation:

Laser ablation is a more advanced method compared to the arc-discharge technique. Graphite is placed inside the quartz chamber filled with inert gas and a temperature of 1200 °C. Carbon atoms are vaporised using a continuous flow of gas of inert gas on a cooled copper collector, where the atoms are deposited, resulting in the growth of CNTs. If the vaporisation occurs with pulsing laser beam, the amount of produced CNTs can be monitored. Similarly to the previous method, with this method, both SWCNTs and MWCNTs are produced, but not in pure form [42, 44].

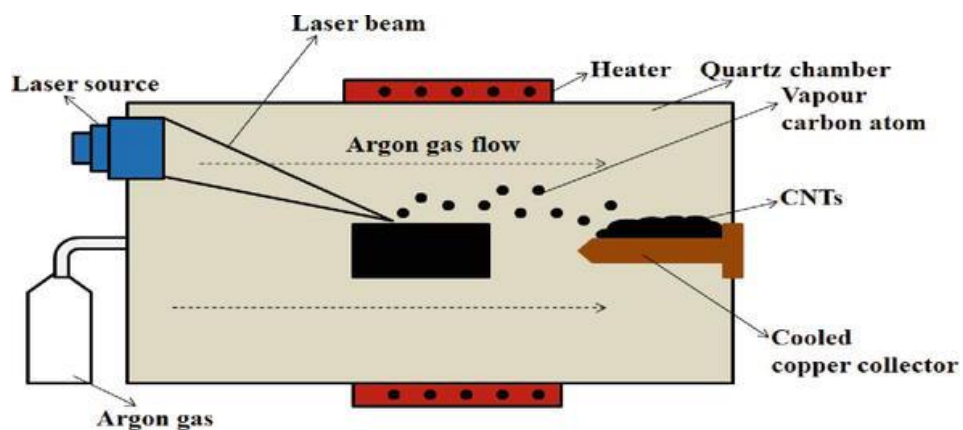


Figure 10: Scheme of the laser ablation method [42].

2.2.3 Carbon Nanospheres

Among carbon-based NMs, carbon nanospheres are another type of unique nanostructure suitable for application in industry due to their chemical and electrical stability [45] or the possibility of production as solid, hollow, or core-shell spheres even with different particle sizes. The material is applicable in drugs for drug transport, such as gas adsorbers or in microelectronic technology as energy storage [46].

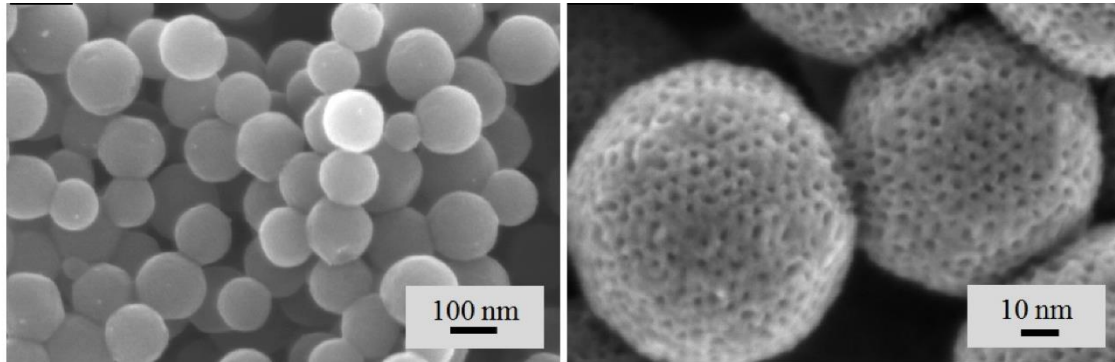


Figure 11: Scanning electron microscopy (SEM) images of porous CN [47].

2.2.3.1 Carbon Nanospheres Synthesis

Generally, there are many methods to produce CNs. Selecting the most suitable and efficient method is essential for the CNs with specific characteristics, i.e. porosity, size, etc. In addition to CVD method, mentioned in the previous chapter,

CNs may be synthesised directly as a by-product during the pyrolysis of waste materials, such as waste plastic, the template method in an inert gas chamber, hydrothermal treatment, hydrothermal treatment, or Stober method [46, 48].

2.3 Nano-enhanced Composite Materials

The growing population and the demand for quality accommodation leads to increased urban development and building construction, which go hand in hand with the increased consumption of building materials. According to studies [49], the total consumption of raw materials used in civil engineering ranges between 30% and 50% in Europe. The most widely used building material is currently Portland Cement-based concrete (PC). The IEA estimated that the total demand for Portland Cement in 2020 would be 1.6 billion tonnes [50]. This represents a serious burden on the environment due to greenhouse gas (GHG) emissions from PC synthesis, which accounted for approximately 7 % of global emissions of man-made CO₂ [51]. Potentially promising

routes to reduce cement consumption may be: 1. efficient design of building elements with lower material consumption and increased durability to ensure long-term use of the structures. Or 2., the use of alternative materials that achieve properties at least comparable to Portland cement concrete.

The other materials commonly used in the building industry are lime mortars and plasters used in modern and historic buildings. In the case of historic buildings, mortars and plasters intended for repair are required to meet strict performance criteria defined, for example, by WTA Directive 2-9-04/D [52], such as mechanical strength (1.5-5 MPa), porosity (>40 %) or water absorption properties (>0.3 kg·m⁻²).

Given the low overall performance of lime-based mortars, increased demands on building materials with respect to their impact on the environment and extended service life, the incorporation of NMs into the composite matrix may represent one way to improve the mechanical strength and other functional parameters of building composites.

The resulting performance of the composite material will be affected not only by the properties of the NMs used but also by the level of distribution in the composite material, which might be complicated. Synthesised nanoparticles tend to form clusters held by weak attractive van der Waals forces and bonds in the dry state or even in solution [53] as shown in Fig. 12.



Figure 12: Agglomeration of CNTs in aqueous solution.

When uniformly dispersed NMs are applied into the material mix, the formed agglomerates create weak spots of low interaction, which decrease mechanical strength. Therefore, these forces must be overcome for proper distribution of NMs and their incorporation into the material mix. Therefore, the effectivity of the applied nanomaterial depends on the technique of NM dispersion and eventual chemical stabilisation, the volume of applied nanomaterials, and possible surface modification of nanomaterials.

2.3.1 Nanomaterial Dispersion Technique

Regarding the dispersion technique of NMs, methods based on the principle of ball milling, mechanical mixing (stirring or high-speed homogenisation), and dispersion by using an ultrasonic bath are mostly used. The research studies of these methods to date are shown in the Tab. 1.

Table 1: Overview of the most common methods of nanomaterial dispersion techniques.

Ref.	Method	Principle	State
[54–57]	Ball milling	Mechanical separation using ball shear friction and impact	Dry, Wet
[58–60]	Stirring	Low speed mixing	Wet
[61–63]	Homogenizer	High-speed shear mixing	Wet
[64–71]	Ultrasonication	Ultrasonic waves	Wet

Similarly, to the exfoliation of the graphene, ball milling is one of the cost-effective and eco-friendly methods of dispersion of NM. This method is based on the separation of NM by the energy induced by the impact and shear friction of ceramic, steel, or rubber balls in a rotating cylindrical shell. Also, this technique is suitable for preparing the NM dispersion in both dry and wet states with additives. However, this technique is time-consuming due to long milling, difficult removal of balls or dispersed material, and long cleaning time. Furthermore, there is a high possibility of NM contamination, damage to particles or nanotubes, and reagglomeration, especially after dry grinding [55–57].

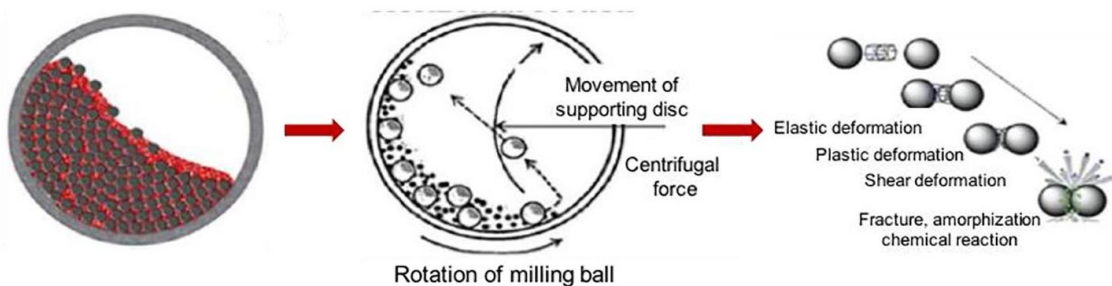


Figure 13: Principle of the ball milling technique [56].

There are basically two types of grinding operation: direct and indirect grinding depending on whether the rollers grind the NM particles directly or if the kinetic energy is first transferred to the grinding medium inside the mill. These mills are the most widely used in the field and can be divided into tumbler ball mills, vibratory mills, and planetary

mills. The effectivity of the grinding is based on the size of the ball mill cylinder, i.e., the diameter of the cylinder with the higher falling height of the balls, and specifically on the rotational speed or vibration frequency [56].

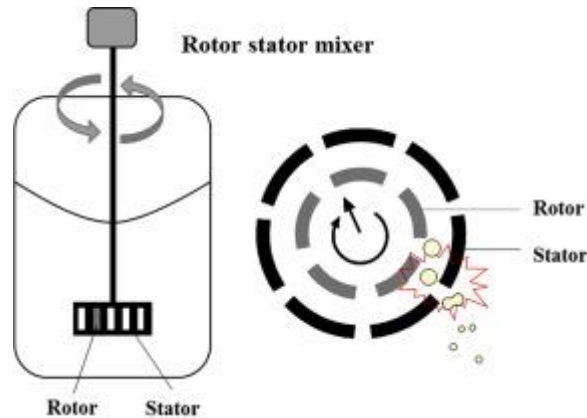


Figure 14: Schematic of rotor-stator type homogenizer [72].

Mechanical or magnetic stirring is a more basic method of preparing the NM dispersion. This technique is used mainly when a high mixing speed is not required and at the same time additional chemical agents must be diluted to improve dispersion, modify the surface of the nanomaterial or even stir in the whole composite mixture [58, 59]. On the other hand, studies have shown that stirring could in some cases be more effective than the commonly used sonication method [60]. Also, with respect to the ecotoxicity of NMs, there are fewer toxic substances released from NPs during stirring compared to, e.g., the ultrasonic method. However, this depends on the type of NM and the power of the ultrasonication and/or the energy of stirring [73].

The most used methods are high-speed homogenisation and ultrasonication. Shear homogenization is carried out by means of a rotating force generated by the mixer rotor creating high shear forces in close-clearance gap between the rotor and stator. This causes separation of the NMs. As in the previous case, it is possible to disperse nanomaterials both in solution with chemical additives and throughout the composite mixture, but only when a sufficient rotational speed ($\omega > 9000$ RPM) is maintained [61–63].

The ultrasonic method is based on the transmission of ultrasonic waves through the medium in which the NMs are dispersed. When the waves reach the NM clusters or bundles, the shock forces start to disrupt their surface layers and separate individual NPs from clusters; thus, they overcome van der Waals forces. The sonication technique is divided into two types: a direct (probe) or indirect (ultrasonic bath, vial tweeter) ultrasound source. The probe ultrasonication has higher efficiency; there is a danger of

contamination through the probe and through the open surface of the uncovered vessel. The degree of homogenisation of the NM depends on the time and amplitude of the ultrasonication, the medium in which the NMs are dispersed, and the volume of the vessel. Although prolonged dispersion using ultrasound can improve the homogeneity of the nanosolution, it can, as in the case of previous methods, distort and tear the nanoparticles. Additionally, heat is produced during ultrasonication, which can be a potential problem due to evaporation of the solution and when volatile solutions are used. Therefore, in these cases, the solution must be cooled [64, 65]. The dispersion of NMs using an ultrasound probe / bath to achieve the best homogenisation can be tens of minutes [66, 67], hours [68–70], or even days [71].

2.3.2 Nanomaterial Chemical Functionalization

The homogeneity of the nanomaterial dispersion and its stability can be further improved by altering the surface characteristics of the NPs, in addition to choosing a suitable dispersion method. Functionalised NPs obtain surface charge (positive or negative), causing the particles to be repulsive and oppose van der Waals forces, leading to better dispersed NPs in solution [74].

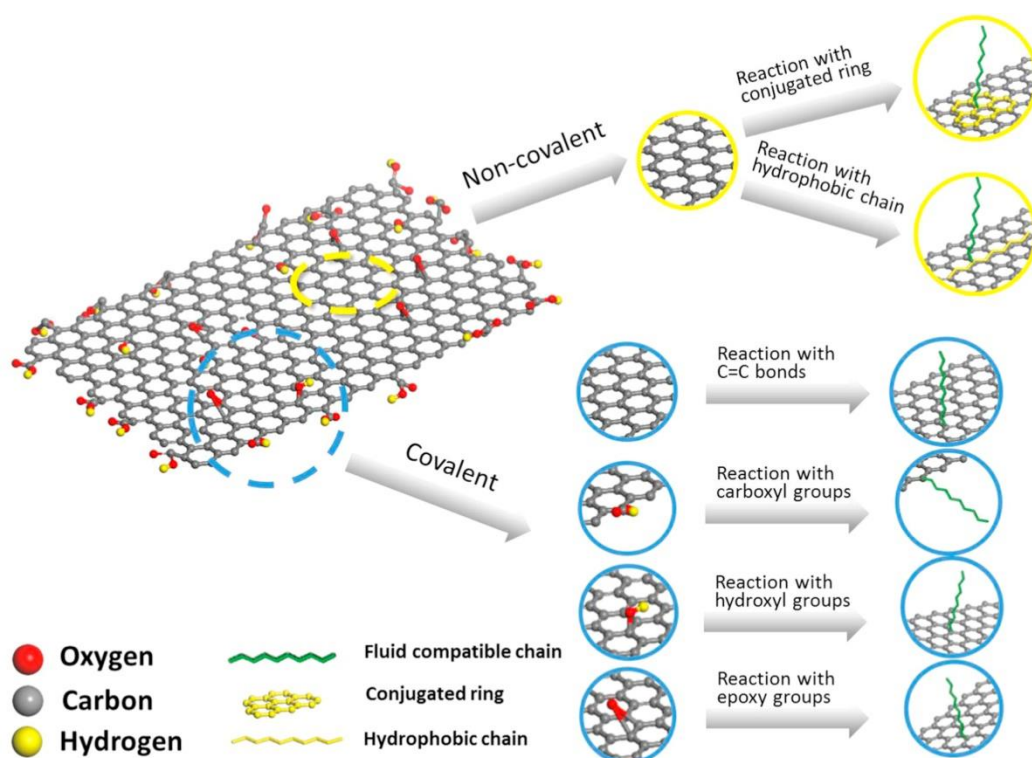


Figure 15: Schematic showing non-covalent and covalent surface modification of carbon nanomaterials [75].

Surface modification methods are divided into covalent and noncovalent functionalisation. The schematic of both methods is shown in Fig. 15.

The first method, covalent functionalization, involves the formation of chemical covalent bonds between functionally reactive molecules and the surface of NPs. These functional groups cause hydrophobicity of the surface and increase dispersing effectivity, high colloidal stability, and change other properties such as electric conductivity or increase interfacial bonding to other materials, e.g., polymers. The other advantage of covalent functionalisation is the strength of the bond in comparison to noncovalent functionalisation. In the case of carbon-based NMs, the common functional groups are hydroxyl (-OH), carboxyl (-OOH), and amine (-NH₂) groups formed in a high acidic environment. [65, 76–78]. An overview of other possible functional groups is shown in Fig. 15.

Noncovalent bonds are based on enhancement using chemical agents such as hydrocarbons, biomolecules, surfactants, or solvents, to create bonds through van der Waals forces, hydrogen bonding, charge transfer, and π - π interactions. These interactions achieve weaker bonding strength compared to covalent functionalization. However, noncovalent functionalisation is technically less difficult because it does not change the carbon nanostructure. Thus, dispersion effectivity is enhanced while the physical properties of NMs are preserved [65, 79].

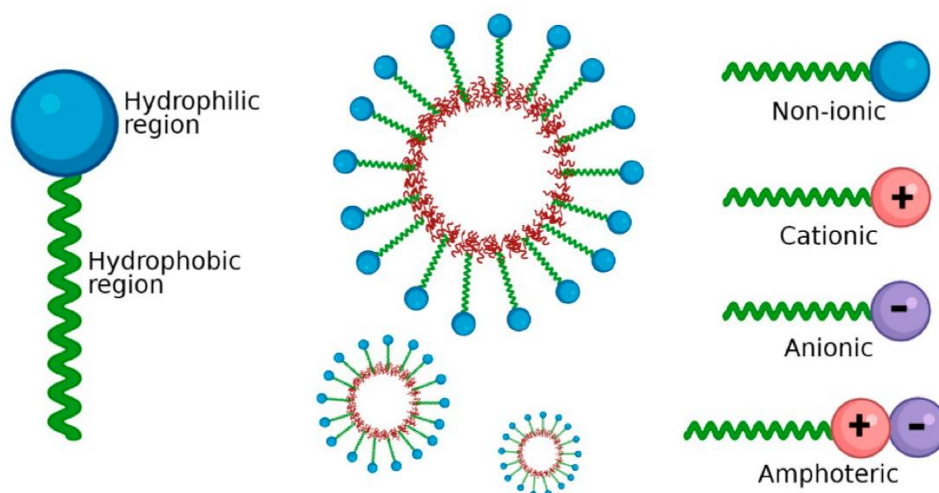


Figure 16: Structure of surfactants [74].

The most widely used chemicals for non-covalent bonding are ionic and non-ionic surfactants. In this case, the amphiphilic molecule of the chemical agent is divided into two segments. The hydrophobic segment (tail) is linked to the NM surface, whereas the hydrophilic segment (head), which can be charged (ionic) or neutral (nonionic), interacts with the surrounding particles and solution. [74, 80, 81]. The arrangement of a typical surfactant molecule is shown in Fig. 16.

Studies investigating the stability of nano-solutions agree that despite the proven positive effect of surfactants on NM dispersion, it is necessary to test and determine their maximum or optimum concentrations, respectively. If a surfactant concentration is too low, a suitable distribution of nanoparticle dispersion will not be achieved because of an insufficient number of amphiphilic molecules. In contrast, at higher concentrations, the surfactant does not dissolve in solution [82]. Thus, a further increase of the surfactant dose is economically inefficient. Too much surfactant can also have an adverse effect on nano-solution properties such as thermal properties, viscosity, surface tension, excessive foam formation and stabilization or affect the hardening process of composite materials [83, 84].

Table 2: A selection of studies dealing with surfactant-aided NM dispersion.

Ref.	Author & year	NMs	Surfactant	Surfactant / NM ratio	Findings
[85]	C. Selvam et al. (2017)	GN	Sodium deoxycholate (SDC)	1.5 - 3.75:1	Enhanced thermal conductivity by 29 %.
[86]	D. Sidhartha et al. (2019)	GN	Gum Acacia	0.5:1	Enhanced thermal conductivity by 17 %.
[87]	M. Mehrali et al. (2016)	Nitro doped GN	Triton X 100	0.4 - 0.25:1	Increased thermal conductivity, no agglomeration was observed.
[88]	D. K. Agarwal et al. (2016)	GN	Oleylamine Oleic acid Tween-20	0-3 – 1.2:1	Optimum ratio: 0.6:1.
[89]	S. U. Ilyas et al. (2020)	GN	Sodium Dodecyl Sulfate (SDS)	0.5 – 2:1	Optimum ratio 1.5:1: was stable for 72 hours.
[90]	A. C. Zaman et al (2020)	MWCNT	Sodium dodecyl benzene sulfonate (SDBS)	4 – 20:1	The nanofluid in ratio 7:1 was stable for more than 6 months.

It is apparent that a large variety of chemical agents can be used as surfactants. At the same time, it is very important that their concentration is optimally designed for the most efficient dispersion of NMs. A list of some of the investigated substances and their optimal concentrations is given in Tab. 2.

The other effective chemical agent supporting the dispersion of NM in cement-based composites is superplasticizers (SP). SP is commonly used for ordinary or high-performance concrete to improve the workability of the mix and water reducer. The mixtures produced achieve a higher compressive strength. SP works on the principle of electrostatic repulsion on steric hindrance. When SP is added to the mixture, it is absorbed in the cement grains and disperses them because of the repulsive forces of their negatively charged anionic groups. This increases the flow characteristics of the dispersion of the concrete and cement grains. The same effect is applied when a plasticizer is applied to the NMs. This procedure can improve both the flow characteristics of the concrete and the dispersion of the NMs, which disperse both NMs and cement grains [91–94].

2.3.3 Concentration of Nano-additive

In addition to the method of preparation and the chemical additives used, the homogeneity of the NM dispersion is also influenced by the concentration of NMs. Excess concentration may lead to an improvement in the final properties of the composite material or, in some cases, degraded compared to a composite material without additives. Therefore, it is necessary to select the optimal concentration of NMs in the composite material from the point of view of material and financial efficiency [95]. This phenomenon can be mainly caused by two factors.

When the volume of applied NPs increases, these nanoparticles have a higher tendency to aggregate with the help of van der Waals forces, i.e. low dispersing ability. When stabilizing chemicals are used, this tendency can arise when an inappropriate concentration of surfactant is used, and thus, insufficient surface modification occurs. NPs form aggregates and clusters with a low binding capacity to the material matrix and to each other, i.e., weak spots that are responsible for the low mechanical resistance of the composite material [96].

The second factor effect is influenced by the binding of the contact surfaces of the individual particles and the composite material matrix. When surface area is increased, better interaction can be achieved, which can cause a more advantageous effect of 2D nanomaterials compared to their 1D counterparts [97]. Over the years, many studies have been published on the effect of NM concentration on various properties of the

material, ranging from mechanical properties [95–102] to hygric properties or gas permeability [103], especially polymers and Portland cement-based composites. Unfortunately, there are not many studies dealing with the application of NMs in lime-based mortars. A selection of some of these is listed in the Tab. 3.

Table 3: A selection of studies dealing with cement-based composites with variable concentration of NMs.

Ref.	Author & year	NMs	Studied volume	Best volume	Mechanical strength improvement
[95]	Y. Chen et al. (2021)	GNP	0.02 - 0.1 wt%	0.04 wt%	28 %
[96]	X. Song et al. (2017)	CNT	0.05 - 0.25 wt%	0.25 wt%	3.5 %
[97]	P. T. Dalla et al. (2020)	GNP CNT	0.2 - 1.2 wt%	1.0 wt% GNP 0.8 wt% CNT	26 % 10 %
[98]	W. Dong et al. (2020)	MWCNT	0.25 wt% 0.5 wt%	0.25 wt%	15 %
[99]	T. Manzur et al. (2016)	CNT	0.05 – 0.5 wt%	0.3 wt%	15 %
[100]	A. Chaipanich et al. (2009)	CNT	0.5 wt% 1.0 wt%	1.0 wt%	9 %
[101]	Z. Ge et al. (2021)	GNP	0,05 - 1.0 wt%	0.1 wt%	12 %
[102]	Y. V. Jeevanagoudar et al. (2017)	MWCNT	0.2 – 0.8 wt%	0.4 wt%	16 %
[104]	A. Gholampour et al. (2017)	GO	0.01 – 0.5 wt%	0.1 wt%	77 %

As can be seen in Tab. 3, the results vary considerably from study to study. This is due to both the different methods of preparation of the nanomaterials and the

characteristics of the NMs themselves. Surprisingly, it is also the case that some studies achieved overall lower results, even assuming the use of a suitable dispersion method and chemical stabilising agents.

For example, in the study by Jeevanagoudar et al. [102] MWCNTs were applied to cement-based mortar. Prior to the mixing procedure, the NMs were dispersed using magnetic stirring followed by sonication with no additional chemical agents. The 0.2 wt% of NMs dosage resulted in compressive strength increase by 7 %, while the best result was obtained with use of 0.4 wt% MWCNTs, approx. 17 % improvement. A higher dosage resulted in a lower strength. On the other hand, X. Song et al. [96] achieved the highest increase in compressive strength of 3.5 %, when 0.25 wt% of MWCNT was applied. Even with the use of dispersant Polyvinyl Pyrrolidone (PVP).

It is important to note that improvement in mechanical properties and maximum performance of NMs can occur even with the application of very small amounts of NPs. In the study by Dalla et al. [97] nanoparticles were dispersed before mixing using ultrasonication aided by a polycarboxylate-based superplasticizer. The optimal amount of GN was observed, 1.0 wt% which resulted in an increase of mechanical strength by 26 %. Chen et al. [95] used a similar dispersing method on GN, also aided with polycarboxylate-based superplasticizer. With a lower dosage, 0.04 wt% reached a nearly similar increase in compressive strength, more than 28 % higher. When the concentration of GNs was subsequently increased, it was gradually reduced to 50 MPa when 1.0 wt% was applied.

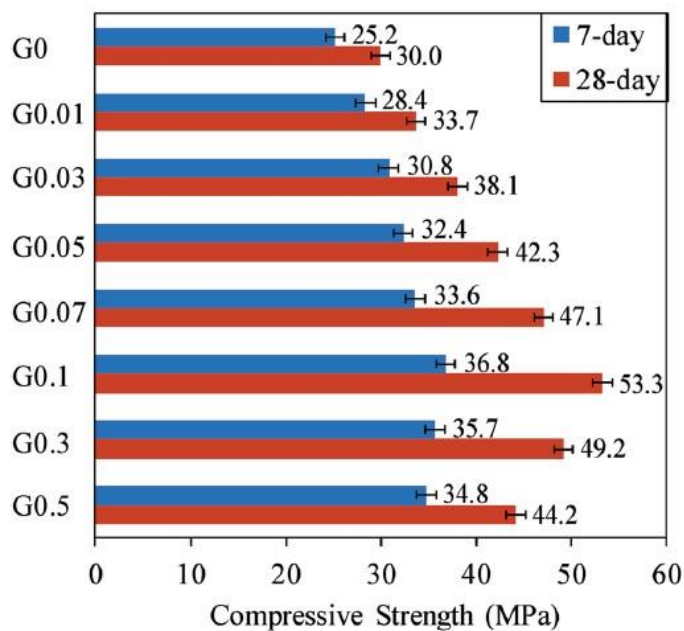


Figure 17: Variation of compressive strength of GO-cement mortar with different GO contents (0-0.5 %) [104].

A. Gholampour et al. [104] studied the influence of GO dosage on cement mortar. GO was sonicated in aqueous solution with a superplasticizer for 10 minutes, then mixed with the rest of the ingredients. Fig. 17 shows the increasing trend of mechanical strength with increasing concentration of GO. The optimal volume of applied GO was 0.1 wt%, which increased the compressive strength by more than 77 %. The application of GO exceeding 0.1 wt% led to a consequent decrease in strength.

Studies on the possible application of NMs are not only concerned with Portland cement-based composites. Several studies on improving lime and cement-lime mortars are listed in the Tab. 4.

Table 4: A selection of studies dealing with nano-modified lime-based mortars.

Ref.	Author & year	NMs	Studied volume	Mechanical strength improvement
[105]	L.-C. Pavlopoulou et al. (2023)	MWCNT	0.15 wt%	23 %
[106]	A.-E. Dimou et al. (2022)	MWCNT OSO ₃ H COOH	0.10 wt% 0.15 wt%	10.6 % 3.5 %
[107]	A.-E. Dimou et al. (2020)	MWCNT COOH rGO	0.15 wt% 0.15 wt%	2 % 20 %
[108]	G. H. Nalon et al. (2024)	CBN	3 - 9 wt%	No improvement in strength recorded.
[109]	P. Faria et al. (2017)	GO	0.05 – 1.0 wt%	12.5 % for 0.1 wt%

Lime cement mortar for MWCNTs-modified masonry restoration was studied by Pavlopoulou et al. [105]. An increase in mechanical resistance of 23 % was observed when 0.15 wt% of the nano-additive was used without stabilising agent.

A.-E. Dimou et al. [106] study the enhancement of lime-cement pastes with modified MWCNT, specifically containing carboxyl (COOH) and sulfonic (OSO₃H) groups. Despite the higher dose used in the case of carboxylated MWCNTs, this modification was ineffective, with only a 2 % increase in mechanical resistance. However, 0.1 wt% paste of sulfonated MWCNTs reached higher strength compared to the latter, by 10.6 % of the reference value. Another study by Dimou et al. [107] focused on natural hydraulic lime

pastes (NHL) with 0.15 wt% carboxylated MWCNTS and reduced GO (rGO). The modification with MWCNTs achieved roughly the same result as in the previously mentioned study, improvement only by 3 %. The second nanomodification with MgO obtained a significantly better result, i.e., a 20% increase in mechanical resistance. On the other hand, Faria et al. [107] applied nonmodified GO in NHL mortar with a 12.5 % increase in strength when 0.1 wt% of NP was applied.

3 Main Aims of Doctoral Thesis

Increasing demands on building materials require the use of alternative materials and the necessary improvement of existing ones. Improvements can be achieved by changing the material composition, such as adding nanomaterials as nano-additives to the composite material. The objectives of this dissertation thesis are as follows:

- a) Commercially available carbon-based nanomaterials analysis.
- b) Design, development, and optimisation of magnesia-based and lime-based composites with carbon-based graphene, nanotubes, and spheres.
- c) Microstructural analysis of prepared composites.
- d) Investigation of the basic chemical, physical, mechanical, and thermophysical properties of prepared composites.
- e) Cost effectivity of studied nano-enhancements.

The experimental results of this study are divided into two parts. The first part focusses on the effect of nano-additives on light-burnt magnesium oxide-based composite material using high purity MgO. The experimental measurement of this part was carried out in collaboration with colleagues from the Department of Inorganic Chemistry at the Faculty of Chemical Technology, UCT Prague.

The second part focusses on the design and evaluation of the optimal application technique and volume of nano-additives to improve the properties of commercial magnesium-based and lime-based mortars. Therefore, the aim of this part is to find an optimal technique to effectively disperse NMs in aqueous solution, regarding the technological process and additional dispersion-promoting chemical agents, if needed. Design the composition of mortars and evaluate performance and cost effectivity to determine the optimal combination of nano-additives for each composite material.

The obtained experimental data will be used for further development of nanoenhanced composite materials, especially lime-based mortars.

4 Experimental

This chapter is devoted to the description of the materials used in the preparation of lime and magnesium mortar samples, the design of individual composite mixtures, the procedure of sample preparation, and the description of the experimental methods chosen for the evaluation of the properties of the tested mixtures. Experimental test methodology is summarised in Annex A.

4.1 Used Materials

This section lists all of the materials used as raw materials for the composite mixtures, the modified nanomaterials (NMs), and the chemicals used to stabilise the nanomaterial dispersion that were used in the measurements described later in this study.

4.1.1 Binders

The chemical composition of the binders, determined by XRF analysis, as well as the loose bulk density, the specific density obtained by the helium pycnometer, and the specific surface measured with the Blaine air permeability apparatus, are listed in Tab.5.

Table 5: Chemical composition of the studied binders.

Substance	Mass %			
	CI 90-S	HL 5	MgO	MgO p.a.
CaO	95.32	57.46	5.23	0.09
MgO	1.23	1.48	80.52	93.19
SiO ₂	0.27	20.44	3.8	0.28
Fe ₂ O ₃	0.05	1.77	3.81	0.01
Al ₂ O ₃	3.06	11.63	6.02	6.23
SrO	0.04	0.04	0.39	0.08
SO ₃	-	1.44	0.22	-
MnO	-	0.33	-	-
Na ₂ O	-	2.39	-	-
K ₂ O	-	2.31	-	-
Σ	99.9	99.3	99.9	99.9
Loose bulk density (kg·m ⁻³)	446	787	840	447
Specific density (kg·m ⁻³)	2227	2624	3340	3459
Blaine specific surface (m ² ·kg ⁻¹)	1653	357	690	1663

The chemical composition of the binders, determined by XRF analysis, is listed in Tab. 5. In this dissertation, 4 types of binders were used. The first two binders belong to

the traditionally used lime-based mortar binders, namely lime hydrate CL 90-S (Čertovy schody s.r.o., Lhoist group, Czech Republic) and natural hydraulic lime HL 5 TrassitPlus (Baumit GmbH, Austria). The other two binders are based on light-burnt magnesium oxide as an alternative to ordinary used Portland Cement, because of its high strength and lower carbon emissions during production [110]. Specifically, these are commercially produced light-burnt MgO of 81% purity (Styromagnesit Steirische Magnesitindustrie Ltd., Oberdorf, Austria) and MgO p.a. with >98% purity. To form the magnesium mortar, both MgO powders had to be mixed with an aqueous solution of $\text{MgCl}_2 \cdot 6\text{H}_2\text{O}$ (Lach-Ner Ltd., Neratovice, Czech Republic).

The particle size distribution was measured by laser diffraction with an Analysette 22 Micro Tec instrument (FRITSCH GmbH Idar-Oberstein, Germany). The resulting distribution curves are shown in Fig. 18.

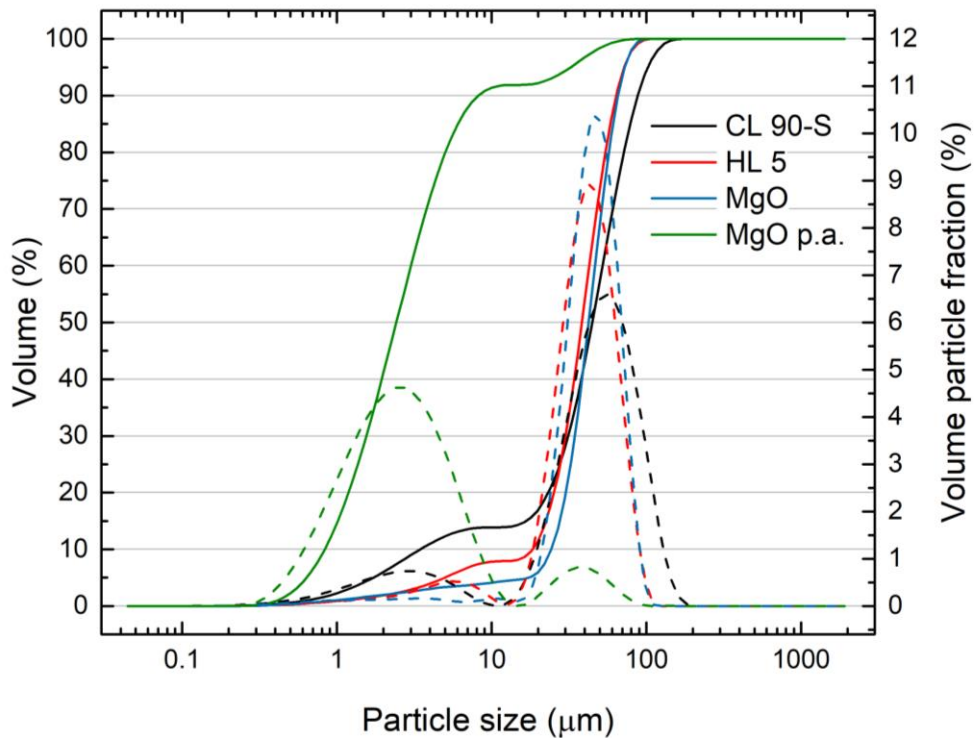


Figure 18: Particle size distribution measured by laser diffraction.

4.1.2 Aggregate

In the cases where composite materials in the form of mortars were studied, silica sand (Filtráční písky Ltd., Chlum u Doks, Czech Republic) with a total fraction of 0-2 mm composed of three fractions referred to as PG1 (0-0.5 mm), PG2 (0.5-1.0 mm) and PG3 (1.0-2.0 mm) mixed in a 1 : 1 : 1 ratio was used as aggregate. The loose bulk density of silica sand is $1670 \text{ kg}\cdot\text{m}^{-3}$. The particle size distribution of the sand measured by the sieving method according to the EN 1015-1 standard [111] is shown in Fig. 19.

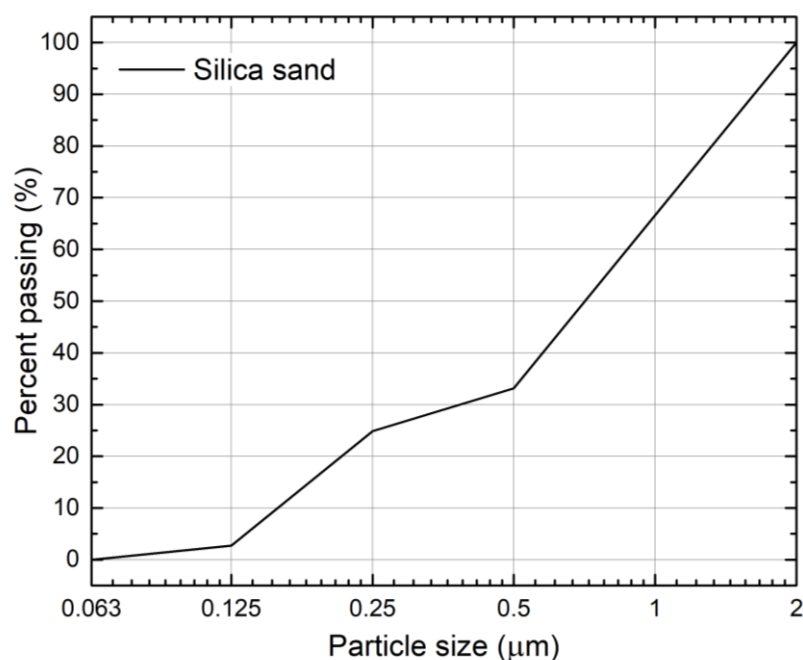


Figure 19: Particle size distribution of silica sand aggregate.

4.1.3 Carbon-based Nanomaterials

Three types of carbon-based nanomaterials (NMs) were investigated in this study, regarding their dimensionality: graphene, multiwalled carbon nanotubes, and carbon spheres. Among graphene NMs: Graphene nanoplatelets C-300 and C-750 (GN, Sigma Aldrich, St. Luis, USA) with a specific surface area of $300 \text{ m}^2\cdot\text{g}^{-1}$ and $750 \text{ m}^2\cdot\text{g}^{-1}$ respectively, were studied. In the case of surface functionalized graphene, industrial grade graphene oxide (ACS Material, LLC, Pasadena, US). The specifications and prices of used graphene NMs obtained from Sigma Aldrich [112] and ACS Material [113] product websites listed in Tab. 6.

Table 6: Specifications of studied graphene NMs [112, 113].

	GNs		GO
	C-300	C-750	
Purity (%)	>95	>95	-
Bulk density ($\text{g}\cdot\text{cm}^{-3}$)	0.2 – 0.4	0.2 – 0.4	0.5
Specific surface area ($\text{m}^2\cdot\text{g}^{-1}$)	300	750	-
Particle size (μm)	<2	<2	<177
Price (€ per gram)	0.84	0.84	7.08

The next type of NMs used are Industrial-grade Multi-walled Carbon Nanotubes TNIM8 prepared by SVD method and TNIMC8 functionalized with 0.51 wt% of carboxyl (-COOH) groups both supplied by TimesNano (Chengdu, China) prepared by SVD method. Specifications of MWCNTs obtained from TimesNano products website [114] are listed in the Tab. 7. The TEM image of the GNs and MWCNTs is shown in Fig. 20.

Table 7: Specifications of studied MWCNTs [114].

	TNIM8	TNIMC8
Functionalization	-	-COOH
Purity (%)	>95	>95
Specific surface area (m ² ·g ⁻¹)	>60	>60
Bulk density (g·cm ⁻³)	0.18	0.18
Outer diameter (nm)	30-80	30-80
Inner diameter(nm)	5-15	5-15
Length (μm)	<10	<10
Price (€ per gram)	0.09	0.14

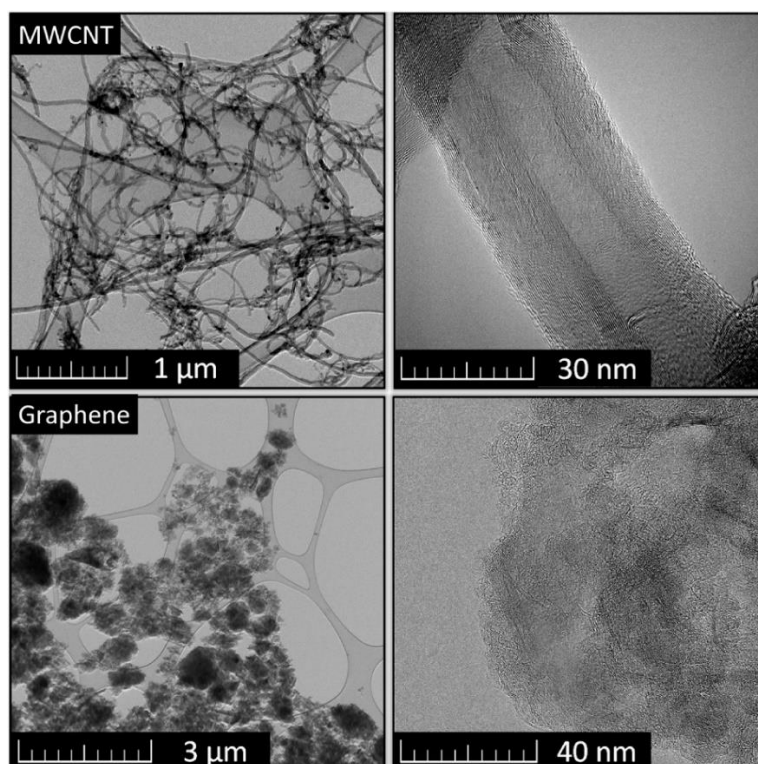


Figure 20. TEM micrograph of MWCNTs and GNs [115].

The last NM type was carbon spheres (CSs). This NM was obtained from the Institute of Plasma Physics of the CAS in Prague. It is a by-product of the gasification of polypropylene by using a microwave plasma torch to produce syngas. During production, the solid CSs were removed from the reactor, where they were subsequently captured and collected in a filter tank.

Characteristics of CSs, obtained by IPP CAS [116], are listed in the Tab. 8. In this case, CSs are a by-product or also a waste material and were supplied free of charge for research purposes. However, it is likely that this product could be for sale, especially if its effectivity as a nano-additive composite material is demonstrated. For this reason, for the purpose of this work, an indicative price was set at the same value as that of industrial grade MWCNTs.

Table 8: Specifications of studied CSs [116].

CS supplied by	
Institute of Plasma Physics of the CAS	
Specific surface area ($\text{g}\cdot\text{cm}^{-3}$)	60
Outer diameter (nm)	10 - 30
Price (€ per gram)	0.09 € per gram

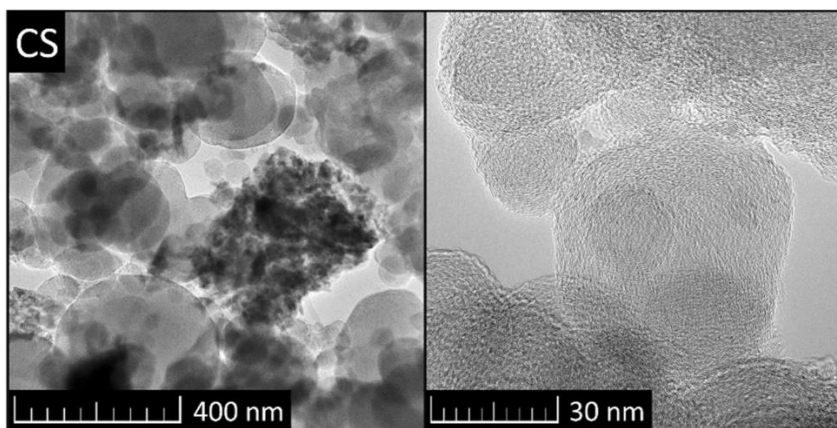


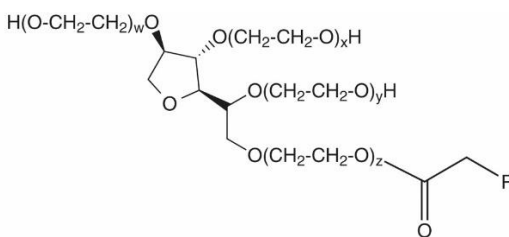
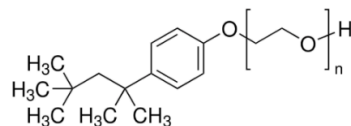
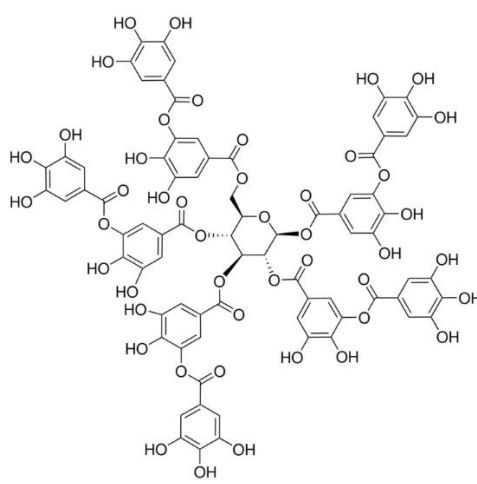
Figure 21: TEM micrograph of CSs [117].

4.1.4 Stabilising Chemical Agents

Although in the case of GNs, visible particle dispersion occurred only in water, in the case of MWCNTs and CSs, visible agglomeration occurred immediately after the ultrasonication stopped. Therefore, based on Chapter 2.3.2, the surface functionalisation of the surface of NMs was used to increase the level of dispersion and stability. Two commercially used non-ionic surfactants were selected for this purpose. The

specifications and prices of all the surfactants used are listed in Tab. 9. The surfactants were namely, Polysorbate 80 (commercial name, Tween® 80, Merck KGaA, Darmstadt, Germany) and octylphenol ethoxylate (commercial name, Triton® X100).

Table 9: Specification of used surfactants [118–123].

Polysorbate 80 (Tween® 80)	
Chemical formula	$C_{64}H_{124}O_{26}$
Price	0.12 € per gram
Chemical composition	
	
Triton® X 100	
Chemical formula	$C_{33}H_{60}O_{10}$
Price	0.03 € per gram
Chemical composition	
	
Tannic acid	
Chemical formula	$C_{76}H_{52}O_{46}$
Price	0.17 € per gram
Chemical composition	
	

The last substance used for NM functionalization was tannic acid (TA). TA is a polyphenolic compound found naturally in plants, fruits, or tree bark. As with previous surfactants, studies have shown that TA molecules can attach to the surface of NP, making them hydrophilic and aiding in NM dispersion [124, 125]. Triton® X100 and Tannic acid were supplied by Carl Roth GmbH, Karlsruhe, Germany.

4.1.5 Antifoamer

Defoamers, also termed foam inhibitors or antifoaming agents, are used to inhibit foam formation. They are divided into two types, fast and slow antifoams. Fast antifoams rupture the foam bubble film in the initial phase of its formation using a bridging-stretching mechanism (Fig. 22), thus completely removing the foam [126, 127].

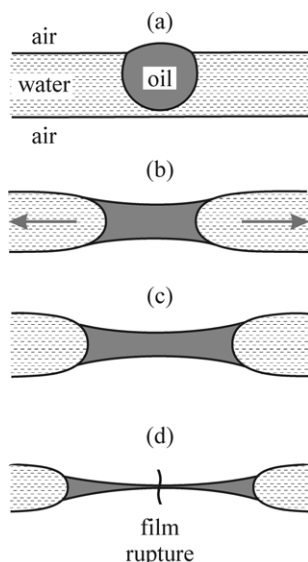


Figure 22: Schematic of the antifoams bridging-stretching mechanism [127].

Due to the high foaming properties of the chemicals used, it was necessary to combine the surfactant solution with an antifoamer or defoamer. Therefore, we used the active silicone polymer antifoamer, Antifoam A concentrate (Sigma-Aldrich, St. Luis, USA).

4.2 Sample Composition and Preparation Methods

In this part of the thesis there is a description of the design of the tested mixtures and the process of their preparation. Due to the composition of the designed mixtures, this section has been divided into two parts. In the first part, pastes and mortars based on magnesium oxychloride cement (MOC), also known as Sorel cement, made of light-burnt MgO chemical-grade are presented. The second part deals with mortars based on light-burnt MgO industrial-grade.

4.2.1 High-purity MOC

4.2.1.1 Influence of the Two-step Homogenization Technique

Other studies focused on the method of preparation of the MOC-based paste using the one-step and two-step homogenisation method, that is, the homogenisation of GN prior to the mixing procedure and the second homogenisation of the paste after the mixing procedure (as shown in Fig. 23) using the Ultra-Turrax T-18 high-shear mixer homogeniser for an additional 5 minutes at 10,000 rpm.

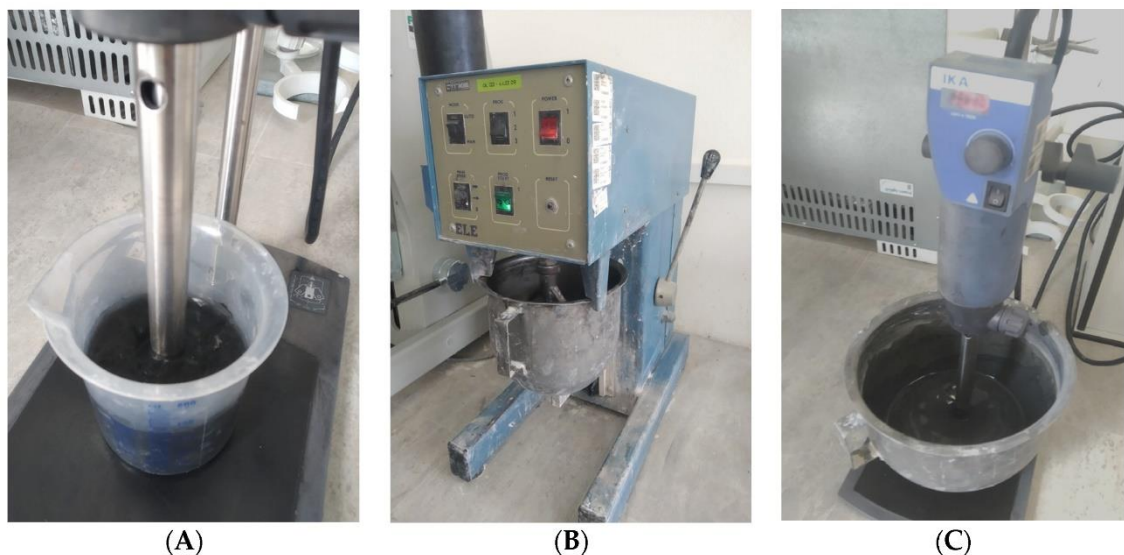


Figure 23: Preparation of composites: A) graphene dispersion in $MgCl_2$ solution; B) mixing of paste; C) second step of homogenization using Ultra-Turrax.

The study was published in the *Materials* 14(6), Article: “MOC Doped with Graphene Nanoplatelets: The Influence of the Mixture Preparation Technology on Its Properties” [128] published in 2021. The composition design was based on the design in a previous

study. The modification was made by adding GNs C-300 as 0.5 wt% of all dried components. The composition is listed in Tab. 10.

Table 10: Two-step homogenization - mixture composition (in kg·m⁻³).

Mixture	MgO	MgCl ₂ ·6H ₂ O	H ₂ O	C-300
MOC-REF	878.9	887.1	548.9	-
MOC-G	878.9	887.1	548.9	8.83
MOC-G-H	878.9	887.1	548.9	8.83

4.2.1.2 Influence of NM-Specific Surface Area

In the first part of the work, the effect of NMs on magnesium-based paste and mortar chemical batches was investigated. Various studies focused on the application methods and types of NM were published within the framework of research projects in collaboration with colleagues from UCT Prague. In all cases, the material was based on a mixture of MgO and MgCl₂ solution and prepared by a similar method.

The first study focused on the influence of the NMs specific surface area on the chemical, structural, and mechanical properties of the composites. The study was published in the *Journal of Building Engineering* 43 (2021). Article: “The influence of graphene specific surface on material properties of MOC-based composites for construction use” [129].

In addition to the control mixture, two types of GNs modifications were used. GNs C-300 (MOC-G300) and C-750 (MOC-G750) with specific surface area 300 m²·g⁻¹ and 750 m²·g⁻¹ respectively, were incorporated in MgO-based paste as 0.5 wt% of all dry components used. Detailed mixture composition is listed in Tab. 11.

Table 11: Specific surface area - mixture composition (in kg·m⁻³).

Mixture	MgO	MgCl ₂ ·6H ₂ O	H ₂ O	C-300	C-750
MOC-REF	878.9	887.1	548.9	-	-
MOC-G300	878.9	887.1	548.9	8.83	-
MOC-G750	878.9	887.1	548.9	-	8.83

4.2.1.3 Influence of Nanomaterial Dosage

The influence of NMs content was studied in the article: “Magnesium oxychloride-graphene composites: Towards high strength and water resistant materials for

construction industry”, published in *FlatChem* 29 (2021) [130]. In this study, the composition of MOC paste (Tab. 12) was calculated using stoichiometry with MgO addition, which did not react and served as filler. Plain paste (MOC-REF) was modified with GNs C-750 in 0.2 wt% (MOC-G0.2), 0.5 wt% (MOC-G0.5) and 1.0 wt% (MOC-G1.0) of paste weight.

Table 12: Nanomaterial dosage - mixture composition (in $\text{kg}\cdot\text{m}^{-3}$).

Mixture	MgO	MgCl ₂ ·6H ₂ O	H ₂ O	C-750
MOC-REF	809.95	583.76	362.11	-
MOC-G0.2	808.34	582.59	362.11	3.51
MOC-G0.5	806.00	580.83	360.20	8.78
MOC-G1.0	801.90	577.91	358.45	17.56

The samples MOC-REF, MOC-G0.2, MOC-G0.5 and MOC-G1.0 of MOC composites enhanced with GNs are shown in Fig. 24.

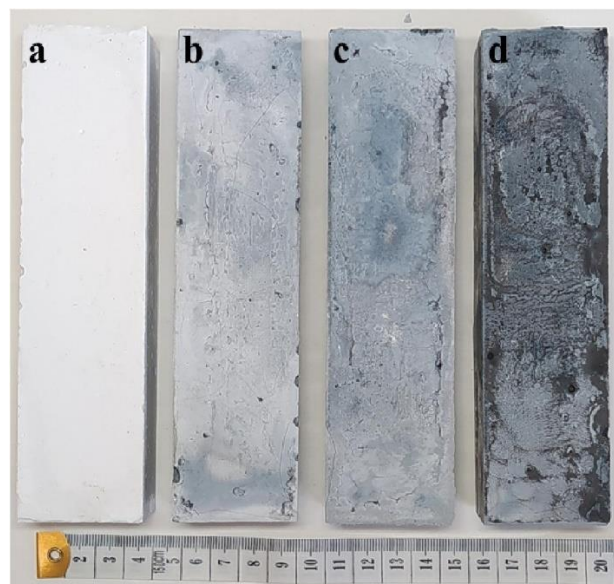


Figure 24: Photograph of the prepared prismatic specimens of a) MOC-REF; b) MOC-G0.2; c) MOCG0.5 and d) MOC-G1.0.

4.2.1.4 Combination of 1D and 2D Nano-additives

The modification of MOC using a combination of 1D and 2D NMs was studied in “Ultra-high strength multicomponent composites based on reactive magnesia: Tailoring of material properties by addition of 1D and 2D carbon nanoadditives” published in *Journal of Building Engineering* 50 (2022) [115]. The MOC paste was modified with GNs and MWCNTs, specifically C-750 and TINM8 without surface treatment. The dosage of

both NMs was 0.1 wt% and 0.2 wt% as shown in the composition of the mixture listed in Tab 13.

Table 13: Co-doped non-functionalized NMs - mixture composition (in $\text{kg}\cdot\text{m}^{-3}$).

Mixture	MgO	MgCl ₂ ·6H ₂ O	H ₂ O	C-750	TINM8
MOC-REF	810.0	583.8	362.0	-	-
MOC-G-MWCNT-0.1	808.3	582.6	361.2	1.8	1.8
MOC-G-MWCNT-0.2	806.7	581.4	360.5	3.5	3.5

The same approach was taken in the study “Co-Doped Magnesium Oxychloride Composites with Unique Flexural Strength for Construction Use” published in *Materials* 15(2) (2022) [131]. In this case, the same composition (Tab. 14) and application procedure was used, but with functionalized NMs. Specifically, GO and TNIMC8, both functionalized with carboxyl groups (-COOH).

Table 14: Co-doped functionalized NMs - mixture composition (in $\text{kg}\cdot\text{m}^{-3}$).

Mixture	MgO	MgCl ₂ ·6H ₂ O	H ₂ O	GO	TNIMC8
MOC-REF	810.0	583.8	362.0	-	-
MOC-GO-OMWCNT-0.1	808.3	582.6	361.2	1.8	1.8
MOC-GO-OMWCNT-0.2	806.7	581.4	360.5	3.5	3.5

4.2.1.5 Carbon Spheres Nano-additive

The last study focused on the characteristics of MOC composite mortar modified with carbon spheres (CSs), which are a byproduct of syngas production by gasification of polypropylene (PP) using a microwave plasma torch. In addition to investigating the effect of the CS dose on the material characteristics, the goal was to apply a higher amount of this carbon waste material. Therefore, the dosage was set at 0.5 wt%, 1.0 wt% and 3.0 wt% of MOC paste for mixtures labelled MOC-CS-0.5, MOC-CS-1.0 and MOC-CS-3.0, respectively. The photograph of CS powder and hardened specimens is shown in Fig. 25. The composition of the mixture is listed in Tab.15

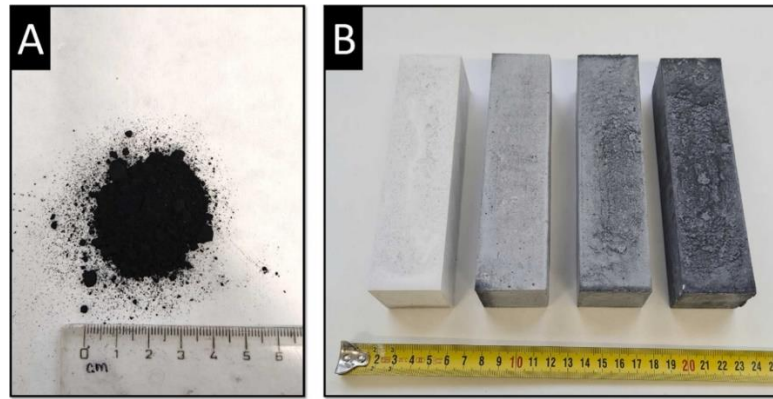


Figure 25: A) CSs powder; B) hardened prismatic samples of MOC mortars.

Table 15: Carbon spheres nano-additive - mixture composition (in $\text{kg}\cdot\text{m}^{-3}$).

Mixture	MgO	MgCl ₂ ·6H ₂ O	H ₂ O	Silica sand	CSs
MOC-REF	479.0	483.3	299.8	-	-
MOC-CS-0.5	479.0	483.3	299.8	1436.9	6.3
MOC-CS-1.0	479.0	483.3	299.8	1436.9	12.6
MOC-CS-3.0	479.0	483.3	299.8	1436.9	37.9

The results were presented in the article “Utilization of waste carbon spheres in magnesium oxychloride cement” published in *Case Studies in Construction Materials* 19 (2023) [117].

4.2.2 High-purity MOC – Sample Preparation

In all of the studies mentioned above, the same methodology of preparation was used. First, the magnesium oxychloride hexahydrate ($\text{MgCl}_2\cdot 6\text{H}_2\text{O}$) was mixed with tap water. The part of this batch was then used for NMs homogenization using high-shear homogenizer UltraTurrax T-18 (IKA -Werke GmbH & Co. KG, Staufen, Germany) at 11 000 rpm for 5 minutes. The suspension of NMs was then mixed with the rest of the MgCl_2 solution and MgO using a planetary type mixer (ELE International, UK) in low-speed regime (paddle 140 rpm, mixing head 62 rpm). In case of mortar, the aggregate was incorporated after 30 seconds. The total mixing time in the low speed regime was 1 minute followed by 0.5 minute in the high speed regime (paddle 285 rpm, mixing head 125 rpm). Then the mixing stopped, and the mixer head and sides of the mixing bowl were cleaned. After that, the mixing continued at a high-speed regime for another 3 minutes.

The prepared mixtures were casted into steel moulds with dimensions 40 mm x 40 mm x 160 mm and demoulded after 24 hours. The samples were stored under laboratory conditions ($T = 23 \pm 2$ °C and $RH = 50 \pm 5$ %) for 7, 14 or 28 days, respectively, depending on the study.

4.2.3 Standardized Mortars

In this part, MgO and lime binder-based mortars designed according to the EN 459-2 [132] modified with non-functionalised GNs, MWCNTs, and CSs were investigated. This section focusses on the conceptual design of the methods used and the mixture design for the most efficient application of NMs and the use of their extraordinary properties.

4.2.3.1 Conceptual Design of the NM Dispersion Technique

As already mentioned, the resulting performance of the composite material will be affected not only by properties of the used NMs but also by the level of distribution in the composite material, because of formation clusters and weak spots held by weak attractive van der Waals forces. For this reason, it is necessary to determine the most efficient method for preparing the applied NMs. As all materials are basically made up of binder, aggregate, and water, it was decided that nanomaterials would always be measured and applied in an aqueous suspension.

Based on the studies mentioned in Chapter 2.3, two methods of nanosuspension preparation were chosen, namely the ultrasonic and high-shear methods. For this test, a nanosuspension was created from individual nanomaterials and deionized water.

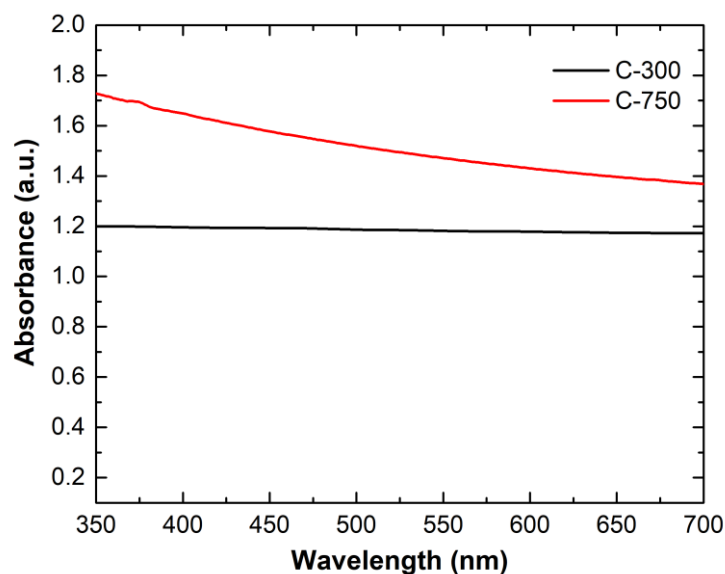


Figure 26: Absorbance spectra of GNs with different specific surface areas.

The concentration of nanosuspension was set at $0.1 \text{ g}\cdot\text{l}^{-1}$ due to the instrument limits. The level of nanosuspension dispersion was evaluated by visible light absorption measured using a UV/VIS instrument GENESYS 30 Visible Spectrophotometer (Thermo Fisher Scientific Inc., Massachusetts, USA). When NPs are dispersed in a liquid, the surface of these nanoparticles will absorb visible UV light passing through the liquid. As the level of dispersion of the nanomaterial in suspension increases, a higher absorbance at each wavelength will be measured. An example of this measurement is shown in Fig.26.

Two types of GN with a specific surface area of $300 \text{ m}^2\cdot\text{g}^{-1}$ (C-300) and $750 \text{ m}^2\cdot\text{g}^{-1}$ (C-750) were measured. In both cases, a nanosuspension was made from 150 ml of deionized water with a GN concentration of $0.1 \text{ g}\cdot\text{l}^{-1}$. This suspension was sonicated for 10 min. As can be seen from the results in Fig. 26. The GNs with higher specific surface area achieved higher absorbance at all wavelengths. The difference between unmodified and modified nanosuspensions with MWCNTs is shown in Fig.27.

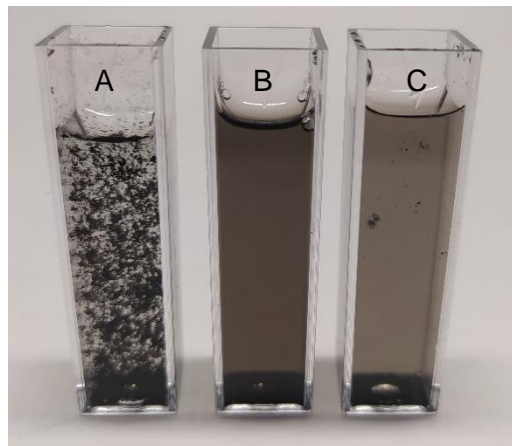


Figure 27: Agglomeration of suspension of A) non-modified and B, C) modified MWCNTs.

Unfortunately, as was investigated in study “*Influence of Different Surfactants on Hydrated Lime Pastes Modified with CNTs*” [133], which was presented in 2021 on INTERNATIONAL CONFERENCE OF NUMERICAL ANALYSIS AND APPLIED MATHEMATICS ICNAAM 2021, surfactants stabilized not only the nanoparticles but also the foam that was produced during mixing. In this study, a total of five mixtures of lime paste were studied. In addition to control lime paste and paste with MWCNTs, three mixtures modified with Tween[®] 80, Triton[®] X100, and the Dynamon SX superplasticizer were prepared.

Table 16: Characteristics of lime pastes with different surface modifications [133].

Composite mix	Spread on table (mm)	Total open porosity (%)	Compressive strength (MPa)
REF	193	53.6	0.78
CNT	178	53.4	0.82
CNT-TW (Tween®)	188	59.8	0.37
CNT-TR (Triton®)	183	71.7	0.20
CNT-D (Dynamon)	235	58.5	1.07

The results in Tab. 16 show that the use of both surfactants increased the porosity of the final composite, especially in the case of Triton® X100 (18,1% increase, absolute value). This resulted in a decrease in compressive strength. The use of a superplasticizer was preferable because the increase in porosity was small. However, it increased the flowability of the mixture, as determined by the flow table test. For this reason, it was necessary to limit the formation of foam.

Table 17: Foamability test results.

Surfactant/antifoamer ratio (wt%)	Volume of trapped air (ml)	
	Tween® 80	Triton® X100
0	55	265
5	25	60
10	15	35
15	10	25
20	7	20
25	3	15
30	0	10
35	-	5
40	-	0

For this purpose, an active silicone polymer antifoamer, Antifoam A concentrate (Sigma-Aldrich, St. Luis, USA) was used. The surfactant/antifoamer ratio required to reduce air bubbles was determined using a foamability test [134]. The foaming test is based on mixing the foam with a high-shear mixer and measuring the volume of produced and stabilised foam. A detailed description of this testing method is given in Section 4.3 Experimental tests.

The results of the foaming test are shown in Tab. 17. While Tween® 80 solution produced only 55 ml of foam, five times more foam was produced using Triton® X100. The maximum concentration of defoamer used to eliminate foam production also differed between both chemical agents.

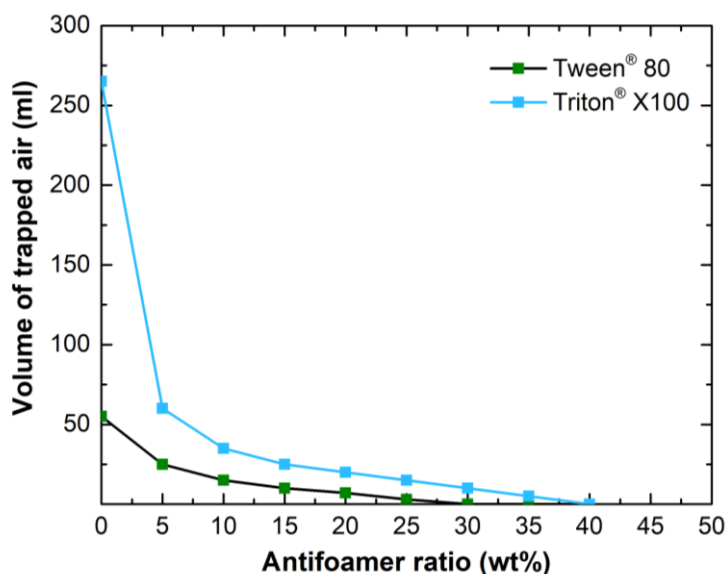


Figure 28: Results of the foamability test.

Although only 30 wt% was required for Tween® 80, in the case of Triton® X100, it was 40 wt% antifoamer. These concentrations were selected for further measurements. The dependence of the antifoamer concentration and the foam produced during mixing is shown in Fig. 28.

Based on these data, all three NMs, GNs C-750, MWCNTs TNIM8, and CSs were dispersed using an Elmasonic Easy 60 H (Elma Schmidbauer GmbH, Germany) and a mechanical high shear mixer UltraTurrax T-18 (IKA -Werke GmbH & Co. KG, Staufen, Germany), respectively. A detailed description of the preparation and measurement methods is given in Chapter 4.3. The Tab. 18 shows the content of the individual tested solutions.

Table 18: Solutions designed for NM dispersion (in g).

Solution	H ₂ O	NMs	Surfactant	Antifoam
H ₂ O only	150	0.015	-	-
Tween® 80	150	0.015	0.015	-
Triton® X100	150	0.015	0.015	-
Tween® 80+Antifoam	150	0.015	0.015	0.0045
Triton® X100+Antifoam	150	0.015	0.015	0.0060
Tannic acid	150	0.015	0.015	-

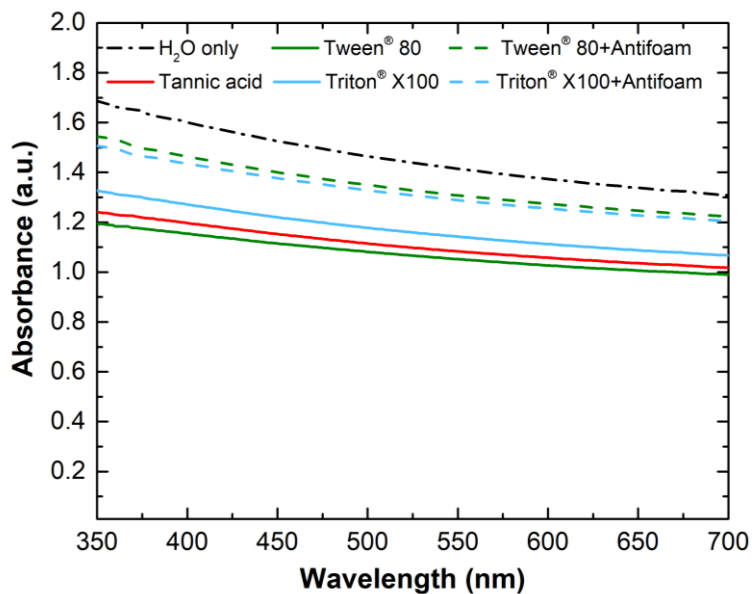


Figure 29: Absorbance spectra of GNs dispersed with an ultrasonic bath.

Figs. 29 and 30 show the resulting UV-visible absorption spectra of the tested GNs suspensions dispersed using an ultrasonic bath (A) and a high-shear mixer (B). It is clear from the results that the ultrasonic bath achieved greater dispersion, release of NMs, and greater exposure of the area of NMs that absorbed UV light for most solutions compared to high-shear homogenization. Using mechanical homogenisation, the solution with Triton® X100 achieved the best dispersion.

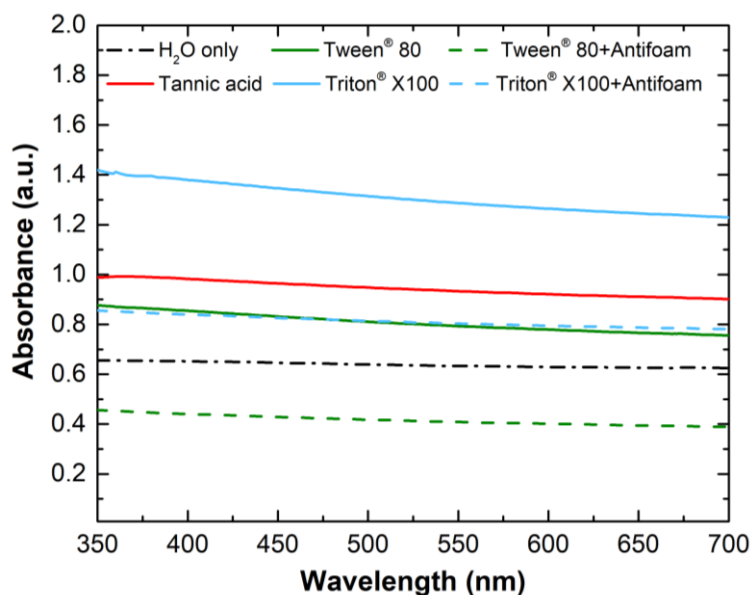


Figure 30: Absorbance spectra of GNs dispersed with a high-shear mixer.

Unfortunately, the same antifoam solution, which is necessary to reduce foamability, achieved a much lower absorbance. Surprisingly, the highest absorbance was achieved by the suspension dispersed by an ultrasound bath in H₂O only with an absorbance of 1.686 at 350 nm compared to the absorbance value of 1.419 of the high shear mixer.

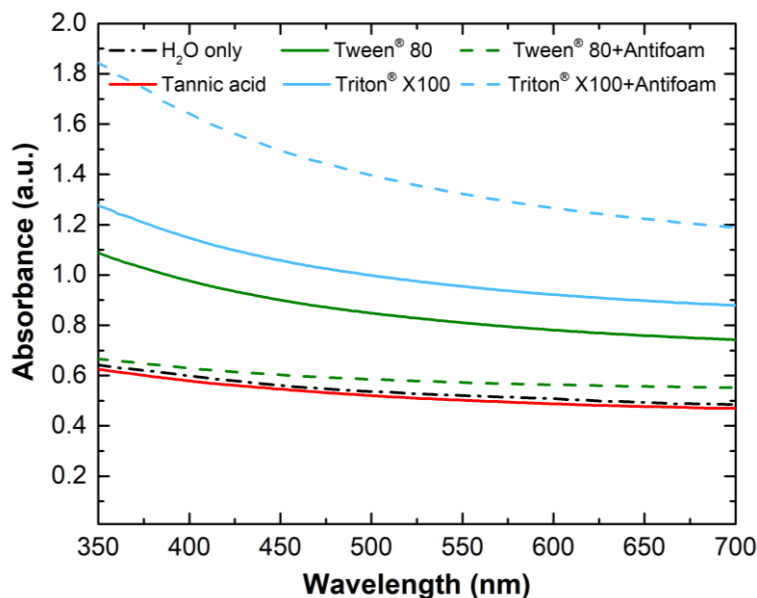


Figure 31: Absorbance spectra of MWCNTs dispersed with an ultrasonic bath.

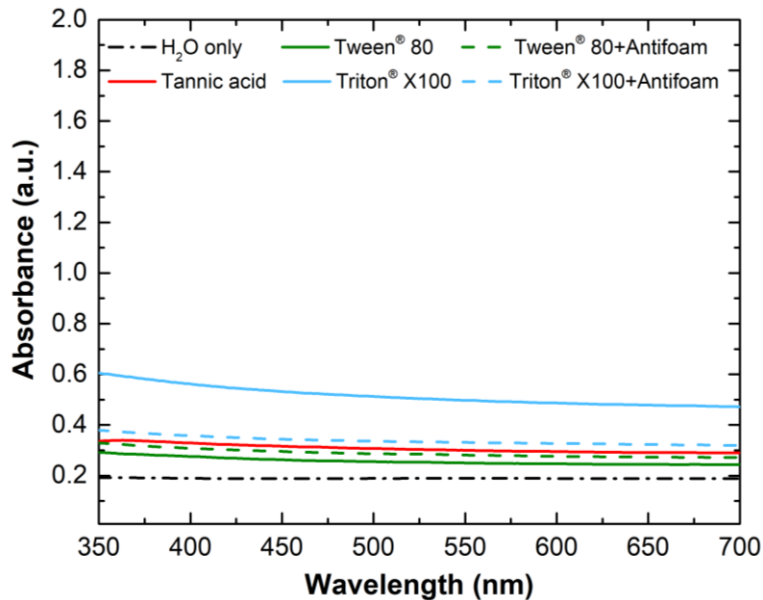


Figure 32: Absorbance spectra of MWCNTs dispersed with a high-shear mixer.

However, in the case of suspensions with MWCNTs, the use of chemical reagents was necessary. In all cases, as shown in Figs.31 and 32, there was an increase in absorbance and thus dilution of NMs compared to dispersion in H₂O. The best results were achieved by suspension of Triton® X100 and antifoamer solution dispersed using

an ultrasonic bath with an absorbance value of 1.841 at 350 nm wavelength. In comparison, this is 3 times higher than the value achieved by the best suspension that underwent high shear mixing (0.605 a.u.) at the same wavelength.

Similar results were also obtained for the measurement of suspensions with CSs (Figs. 33 and 34), where ultrasonic bathing supported by the Triton® X100, surfactant but without antifoamer, proved to be the most suitable dispersion method. The second most suitable option is the use of Tannic acid with an absorbance value of 1.201. This is still a better result compared to the best dispersion with high shear mixing (0.976) at a wavelength of 350 nm.

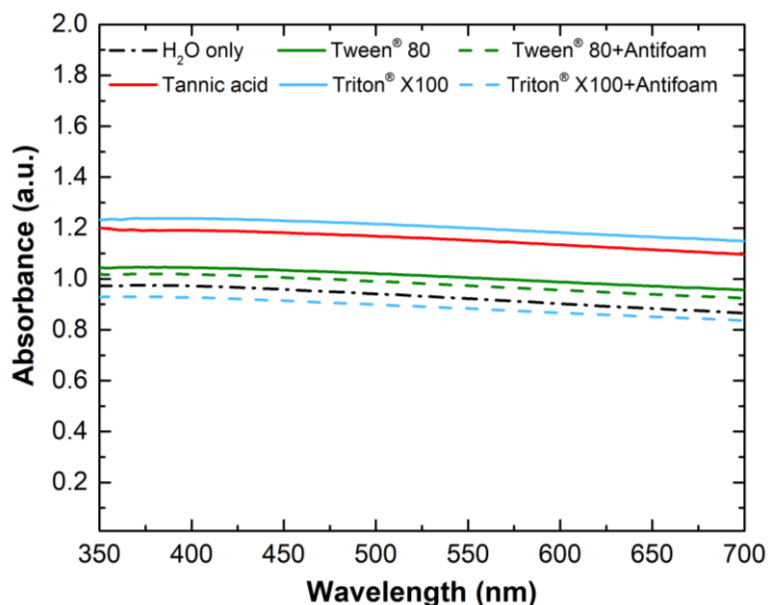


Figure 33: Absorbance spectra of CSs dispersed with an ultrasonic bath.

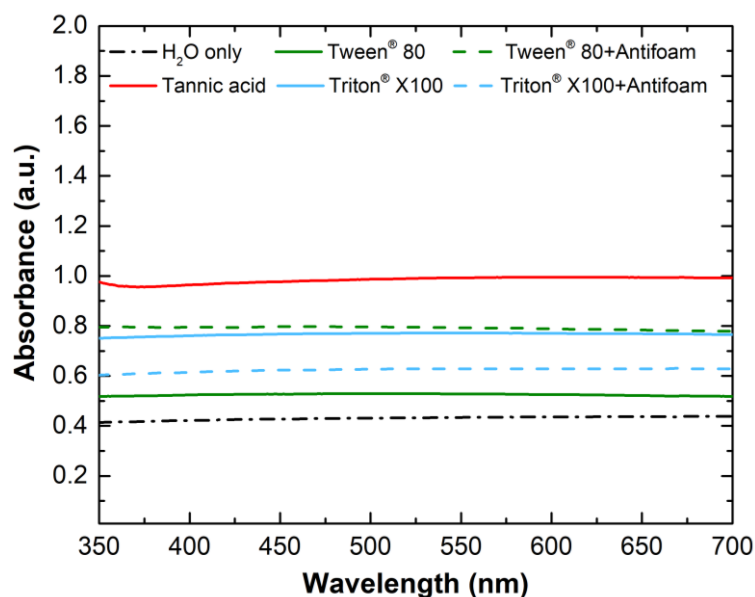


Figure 34: Absorbance spectra of CSs dispersed with a high-shear mixer.

Because no foam formation and stabilisation occur when Tannic acid is used, this combination, i.e., ultrasonication of CSs in Tannin solution, was chosen as the most optimal.

To produce the mixtures, all NMS were dispersed using an ultrasonic bath. Based on previous tests, GNs were ultrasonicated only in H₂O without additional chemical agents, which is beneficial to the final cost of the composite material produced. On the contrary, in the case of MWCNTs, an improvement in dispersion efficiency was achieved when using the Triton X100 solution in both cases. Even in combination with Antifomer, it achieved the best absorbance value among all measurements. Therefore, this combination was chosen for further measurements. In the case of CSs, the dispersion was made in a Tannic acid solution in the material design.

4.2.4 Standardized Mortars – Composite Design

The design of light-burnt MgO, lime hydrate, and hydraulic lime composite mixtures modified with carbon-based NMs was calculated based on EN 459-2 [132] and EN 196-1 [135] to determine the strength class of lime-based binders. The design of the mix is based on a 1: 3 ratio of binder to aggregate and a final fresh mixture spread evaluated using a flow table test of 165 ±3 mm. The spread diameter was achieved by varying the water to binder ratio of the individual mixtures.

These mixtures were further modified with individual NMs or with dispersion-enhancing chemical agents in a of 1: 1 ratio to NM weight and antifoamer according to previous measurements. Based on previous investigations where mechanical property improvement was achieved only up to 0.5% of the NMs dosage, the amount was set at 0.1, 0.3 and 0.5 wt% of the binder.

In the case of the MOC composites, changes were made in the standardised formulation of the mixtures. First, the amount of MgO was increased compared to that of the original formula as a result of its lower reactivity. Second, as a result of the high flow of the mixture, the amount of paste had to be reduced compared to the aggregate to maintain optimum workability. It is well known that MOC composite can contain a large volume of organic and inorganic fillers [136]. However, this change can have a negative effect on the characteristics of the composite, such as porosity or mechanical strength. For this reason, the effect of paste reduction was measured on the final properties of the mixtures. The workability of the final mixtures was optimised by varying the amount of MgCl₂ solution used.

The original design (according to standard) achieved a float-table test spread of 200 mm, more than the requirement. When the amount of MOC paste was reduced by 80%

and along with it the total paste, optimal workability was achieved (Tab. 19). Fortunately, this change does not have too much effect on the final properties of the mixtures. Even when the volume of paste was reduced to half that of the initial design, the material preserved its extraordinary properties only with reduction of workability. On the basis of these results, the composition of MOC composites is listed in the Tab. 20.

Table 19: Characteristics of composites with varying volumes of MOC paste volume.

Mixture	MOC paste volume (%)	Flow-table test spread (mm)	Bulk density ρ_b ($\text{kg}\cdot\text{m}^{-3}$)	Porosity Ψ (%)	Compressive strength f_c (MPa)
MOC-standard	100	200	2142	13.7	80.2
MOC-80%	80	165	2140	13.9	79.3
MOC-60%	60	125	2164	12.1	75.4
MOC-50%	75	100	2172	12.5	75.6

Table 20: Composition of magnesium oxychloride cement (MOC) mortars (in $\text{kg}\cdot\text{m}^{-3}$).

Mixture	MgO	MgCl ₂ ·6H ₂ O	H ₂ O	Silica sand	-	-	-
MOC-REF	503	223	185	1320	-	-	-
	MgO	MgCl ₂ ·6H ₂ O	H ₂ O	Silica sand	C-750	-	-
MOC -G0.1	450	209	173	1380	0.45	-	-
MOC -G0.3	450	209	173	1380	1.35	-	-
MOC -G0.5	450	209	173	1380	2.25	-	-
	MgO	MgCl ₂ ·6H ₂ O	H ₂ O	Silica sand	TNIM8	Triton [®] X100	Antifoam
MOC -CNT0.1	450	204.4	169	1380	0.45	0.45	0.21
MOC -CNT0.3	450	204.4	169	1380	1.35	1.35	0.62
MOC -CNT0.5	450	204.4	169	1380	2.25	2.25	1.03
	MgO	MgCl ₂ ·6H ₂ O	H ₂ O	Silica sand	CS	Tannic acid	-
MOC -S0.1	504	223.3	185	1302	0.50	0.50	-
MOC-S0.3	504	223.3	185	1302	1.51	1.51	-
MOC -S0.5	504	223.3	185	1302	2.52	2.52	-

The final composition of lime mortars is given in Tab.21 and Tab. 22, where hydrated lime is denoted CL, natural hydraulic lime is HL. Individual mixtures are further denoted according to the NMs dosage as G0.1, G0.3 and G0.5 for samples modified with GN, CNT0.1, CNT0.3, CNT0.5, respectively, when MWCNTs are used. The CSs modified mixtures were labelled S0.1, S0.3, and S0.5 for the individual batches used.

Table 21: Composition of hydrated lime (CL) mixtures (in kg·m⁻³).

Mixture	CL90S	H₂O	Silica sand	-	-	-
CL-REF	434	456	1302	-	-	-
	CL90S	H₂O	Silica sand	C-750	-	-
CL-G0.1	411	448	1233	0.41	-	-
CL-G0.3	411	442	1233	1.23	-	-
CL-G0.5	411	432	1233	2.06	-	-
	CL90S	H₂O	Silica sand	TNIM8	Triton[®] X100	Antifoam
CL-CNT0.1	411	442	1233	0.41	0.41	0.19
CL-CNT0.3	411	432	1233	1.23	1.23	0.56
CL-CNT0.5	411	422	1233	2.06	2.06	0.93
	CL90S	H₂O	Silica sand	CS	Tannic acid	-
CL-S0.1	434	1075	1302	0.43	0.43	-
CL-S0.3	434	1050	1302	1.30	1.30	-
CL-S0.5	434	1025	1302	2.17	2.17	-

Table 22: Composition of natural hydraulic lime (HL) mixtures (in $\text{kg}\cdot\text{m}^{-3}$).

Mixture	HL 5	H ₂ O	Silica sand	-	-	-
HL-REF	440	275	1320	-	-	-
	HL 5	H ₂ O	Silica sand	C-750	-	-
HL-G0.1	460	310	1380	0.41	-	-
HL-G0.3	460	310	1380	1.23	-	-
HL-G0.5	460	310	1380	2.06	-	-
	HL 5	H ₂ O	Silica sand	TNIM8	Triton® X100	Antifoam
HL-CNT0.1	460	299	1380	0.46	0.46	0.21
HL-CNT0.3	460	299	1380	1.38	1.38	0.62
HL-CNT0.5	460	299	1380	2.30	2.30	1.03
	HL 5	H ₂ O	Silica sand	CS	Tannic acid	-
HL-S0.1	434	282	1302	0.43	0.43	-
HL-S0.3	434	282	1302	1.30	1.30	-
HL-S0.5	434	282	1302	2.17	2.17	-

4.2.5 Standardized Mortars – Sample Preparation

All three types of mortars were produced using a similar preparation method. First, the chemical agents, if used, were mixed for one hour in part of batch water with a KS 4000 ic control incubator shaker (IKA-Werke GmbH & Co. KG, Staufen, Germany). For MOC mortars, batch water with already mixed MgCl_2 was used.

The NMs were then added to the solution and sonicated in an Elmasonic Easy 60 H ultrasonic bath for 10 minutes. When sonication stopped, the nano-suspension was mixed with the rest of the water, or MgCl_2 solution, and the binder by planetary-type mixer for 30 seconds in low-speed regime (paddle 140 rpm, mixing head 62 rpm). During another 30 seconds, the aggregate was added, followed by mixing in the high-speed regime (paddle 285 rpm, mixing head 125 rpm) for another 30 seconds. Then the mixing stopped, and the mixer head and sides of the mixing bowl were cleaned. After that, the mixing continued at high-speed regime for another 1.5 minutes.

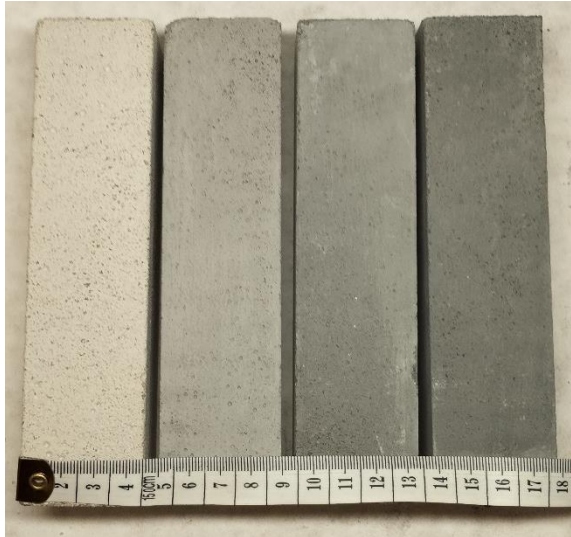


Figure 35: Photograph of HL-CNT samples.

The prepared mixtures were casted in plastic moulds with dimensions 40 mm x 40 mm x 160 mm in two layers, each compacted for 30 seconds with a high-frequency vibrating table. The moulds were then covered with PE foil. The CL and HL samples were removed after 48 hours and stored in the climate chamber at $T = 23 \pm 2$ °C and $RH = 60 \pm 5$ % for the CL samples. The HL samples were stored under the same temperature conditions with $RH = 90 \pm 5$ %. Both conditions are in accordance with EN 459-2 standard EN 459-2. The MOC mixtures have a fast-hardening time, so they could be demoulded after 24 hours, and then stored under laboratory conditions ($T = 23 \pm 2$ °C and $RH = 50 \pm 5$ %).

All samples were cured for a total of 28 days; then the samples were investigated in terms of basic structural characteristics, mechanical strength, and thermal properties.

4.3 Experimental Tests

This chapter describes all the measurement and computational methods used in this research. Experimental tests were carried out under laboratory conditions at a temperature of 22 ± 2 °C and a relative humidity of 40 ± 5 %, unless otherwise stated in the test description.

4.3.1 Raw Material Characteristics

Tab. 23 shows the methodology of the tests performed on raw bulk materials prior to the preparation of composite material specimens.

Table 23: Methodology of raw materials tests performed.

Analysis	Method	Apparatus
Granulometry	Laser Diffraction	Analysette 22 Micro tec plus, FRITSCH
	Blaine Air Permeability	Blaine apparatus UTCM-0280, UTEST
	Sieving test	Analytical sieve machine AS 200 Retsch + standardized sieve set
	Loose bulk density	Analytical balance OHAUS Discovery
Chemical composition	X-ray fluorescence	ARL™ QUANT'X EDXRF Spectrometer, Thermo Scientific™

4.3.1.1 Particle Size Distribution Analysis

For describing the binders used, their particle size distribution was experimentally determined using Analysette 22 Micro Tec plus (FRITSCH GmbH, Weimar, Germany), which allows the detection of particles in the range 0.08 - 2000 μm . The measuring unit contains a red and green laser source, with an output power of 7 mW and wavelengths of 532 nm and 940 nm. The ultrasonic bath, which is part of the dispersion unit, has a power of 50 Watts, which allows a vibration frequency of 40 Hz to be applied to the fluids in the reservoir, thus ensuring sufficient agitation of the agglomerates. The diffracted laser beam, which depends on size of each particle, strikes the sensor lens and the

intensity of diffracted light and the angle of incidence was recorded. Then, the Fraunhofer diffraction model is used to evaluate and calculate the diffraction patterns.

The results of the measurements provide distribution and frequency curves, which can be complemented by the volume fraction of particles at 10, 50 and 90% fraction, calculated with Thermo Fisher Scientific Inc. Milling and Sizing Software MaS Control 1.0.0.0. The particle size distributions of all the studied binders were measured in ethanol.



Figure 36: Analysette 22 Micro Tec plus particle size distribution analyser.

4.3.1.2 Blaine Air Permeability Test

The specific surface area (m^2/kg) of the investigated binders was determined using the Blaine's air permeability method, which is based on determining the air flow rate through the cement bed and comparing it with the flow rate through a bed of material of known specific surface area. Measurements were compared using an automated Blaine's UTCM-0280 apparatus (UTEST, Ankara, Turkey), according to EN 196-6 [135].

Before measurement, the sample was first ground in a friction pan to disperse the particle clumps. A sample of a specific mass, reflecting a suitable degree of porosity of the bed, comparable as much as possible to the reference material, was inserted into the cement bed of the flow chamber and compressed. The flow chamber was then placed in the measuring U-tube of the instrument filled with mineral oil. The top of the flow chamber was plugged with a rubber stopper and the oil level in the tube was raised approximately 3 cm from the bottom edge of the chamber by a vacuum pump. After the plug was removed, the oil level began to drop because of the balancing effect of the

hydrostatic pressure in the U-tube, with air flowing through the cement bed. The levelling rate was automatically measured between two parts of the tube 5 cm apart.



Figure 37: Automatic Blain's air permeability apparatus.

The measurement was repeated three times each time. The oil level drop rate was automatically measured between two fibre optic sensors in the tube 5 cm apart. The measurement was repeated three times for each material. The calculation of specific surface area S ($\text{m}^2 \cdot \text{kg}^{-1}$), based on the measured time of oil level drop and temperature, was calculated using the formula:

$$S = \frac{K}{\rho} \cdot \frac{\sqrt{e^3}}{(1 - e)} \cdot \frac{\sqrt{t}}{\sqrt{0.1 \cdot \eta}} \quad (1)$$

where K (-) is the apparatus constant, ρ ($\text{g} \cdot \text{cm}^{-3}$) is material density, e (-) is porosity of the bed, t (s) is the measured time and η (Pa·s) is air viscosity at the test temperature.

4.3.1.3 Grain Size Distribution

The grain size distribution (granulometry) of the aggregate used was determined using a standard sieve set and a RETSCH AS 200 Basic sieving machine (Retsch, GmbH, Haan, Germany) according to EN 1015-1 [111]. Standard sieves were used for sieving, according to EN 933-2 [137] have mesh sizes of 0.063, 0.125, 0.250, 0.500, 1.0 and 2.0 mm. The maximum aggregate size was 2 mm; therefore, the other sieves of this set, namely 4.0, 8.0, 16.0, 31.5 and 63 mm, were not used. The aggregate weight retained in each sieve was measured, and cumulative passes of the sieves (%) were calculated, from which the grain size line of the sample was plotted.

4.3.1.4 Loose Bulk Density

The loose bulk density ρ_s ($\text{kg}\cdot\text{m}^{-3}$) of the aggregate was determined by the gravimetric method. The volume of the measured amount of filler was determined with a graduated cylinder, and the weight of the fill was determined with an OHAUS Discovery balance with an accuracy of 0.01 g. Then it was calculated by the following equation:

$$\rho_s = \frac{m}{V} \quad (2)$$

where m (kg) is the aggregate mass and V (m^3) is the measured volume of aggregate.

4.3.1.5 X-Ray Fluorescence Analysis (XRF)

X-ray fluorescence analysis was performed on ground samples (Retsch MM 400 ball mill) and dried samples using an EDXRF spectrophotometer ARL Quant'X (Thermo Scientific™, Massachusetts, US). The instrument is equipped with a rhodium X-ray tube and a Si(Li) crystal detector. The acquired data are collected and evaluated by UniQuant software. The relative accuracy of the measurements varies between 0.5 and 5 %.



Figure 38: ARLTM QUANT'X EDXRF Spectrometer, Thermo Scientific.

4.3.2 Nanomaterial Suspension Characteristics

For the most effective application of NMs into the investigated mixtures, it was necessary to find the optimal procedure for the preparation of nano-dispersions with possible modification by surfactants. This chapter is focused on measuring of the characteristics of NM suspension. Methods to evaluate the dispersion efficiency are listed in the Tab. 24. In both tests performed, the suspension consisted of the NM under investigation mixed in distilled water or surfactant solution. Measurements were carried out under laboratory conditions at 22 ± 2 °C

Table 24: Methodology of performed NM suspension tests.

Analysis	Method	Apparatus
Level of dispersion	Ultraviolet-Visible Spectroscopy	GENESYS™ 30 Visible Spectrophotometer, Thermo Scientific™ Ultrasonic bath Elmasonic Easy 60 H, ELMA High-shear mixer UltraTurrax T-18, IKA
Foamability of suspension	Foam volume evaluation	High-shear mixer UltraTurrax T-18, IKA

4.3.2.1 Ultraviolet-visible Spectroscopy

Uv-Vis spectroscopy is based on absorption of light on ultraviolet visible range (180 – 780 nm). When NPs are dispersed in a liquid, the surface of these nanoparticles will absorb visible UV light passing through the liquid. As the level of dispersion of the nanomaterial in suspension increases, a higher absorbance at each wavelength will be measured.

Before measurement of UV-light absorbance, the suspension of NMs with and without chemical agents was subjected to homogenisation, specifically to sonication in an Elmasonic Easy 60 H ultrasonic bath (Elma Schmidbauer GmbH, Germany) for 10 minutes and high-shear mixing with the mechanical homogenizer UltraTurrax T-18 (IKA -Werke GmbH & Co. KG, Staufen, Germany) for 10 minutes at 9500 rpm, respectively. The nano-suspension was placed into the cuvette and measured immediately after the homogenization stops. Water/surfactant solution without nano-additives served as a blank solution for baseline measurement.

The level of nano-suspension dispersion was evaluated by this method using a UV/VIS instrument GENESYS 30 Visible Spectrophotometer (Thermo Fisher Scientific Inc., Massachusetts, USA).



Figure 39: UV-Vis spectrophotometer (A) and cuvettes (B).

4.3.2.2 Foamability of NM Dispersion

The surfactants stabilized not only the nanoparticles but also the foam that was produced during mixing. Therefore, the surfactant/antifoamer ratio required to reduce air bubbles was determined using a foamability test [121]. During this test, a 1 wt% solution of deionized water and surfactant was prepared and mixed in a high-shear mixer for 5 minutes at 9500 rpm. During the mixing process, the solution was aerated to form a stabilized foam. The volume of foam produced was decisive for selecting the best concentration of antifoamer so that no foam will be produced during mixing, as shown in Fig. 40.

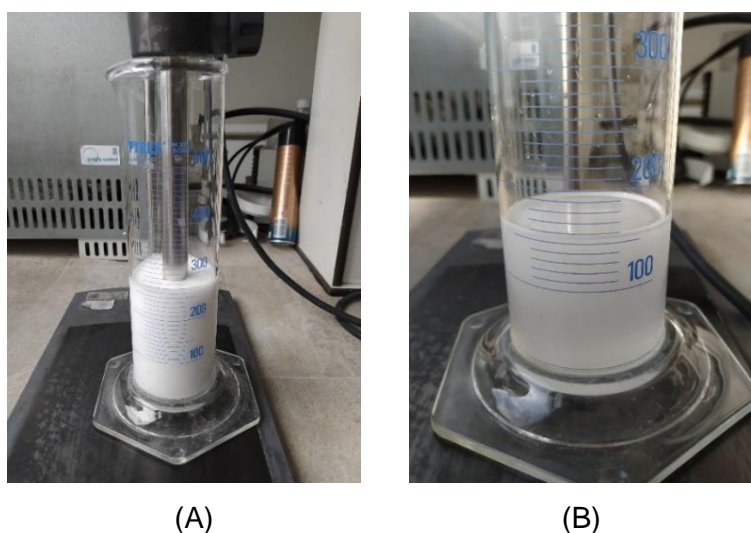


Figure 40: Foam formation during foamability test (A) and foam-free solution (B).

4.3.3 Characteristics of Fresh and Hardened Mortar and Pastes

Table 25: List of the experimental tests performed.

Analysis	Method	Apparatus
Chemical composition	XRD	D2 Phaser, Burger
	FTIR	Nicolet 6700, Thermo Scientific™
Morphology	SEM/EDS	Tescan Lyra 3, TESCAN Phenom™ XL G2, Thermo Scientific™
Material characteristics	Flow table test	Manual mortar flow-table
	Gravimetric	Analytical balance OHAUS Discovery
	Helium Pycnometry	Pycnomatic ATC, Thermo Scientific™
	Mercury intrusion	Mercury Intrusion Porosimeter Pascal 140+440, Thermo Scientific™
Mechanical strength	Three-point bending test	FP 100, Heckert
	Compressive strength test	FP 100 and ED 600, Heckert
	Ultrasonic pulse velocity	Vikasonic, Schleibinger
Thermophysical characteristics	Non-steady State	Hot-disk TPS1500, Hot Disk AB
Water absorption Characteristics	Capillary Water Absorption	Analytical balance OHAUS Discovery
Cost-effectivity	Calculation	-

4.3.3.1 X-Ray Powder Diffraction Analysis (XRD)

The samples were milled to a fine powder and dried to a constant weight, similar to the XRF method. Measurements were carried out using a Bruker D2 Phaser diffractometer (Bruker, Karlsruhe, Germany). The instrument parameters are as follows.

Bragg-Brentano geometry, CuK α source ($\lambda = 0.15418$ nm, U = 40 kV, I = 30 mA). The scanning step size was 0.019° (2 θ). Evaluation of the measured data was performed using High-Score Plus software.



Figure 41: X-Ray powder diffraction apparatus.

4.3.3.2 Fourier Transform Infrared Spectroscopy (FTIR)

Infrared spectrometry is an optical analytical technique used primarily for the identification and structural characterization of organic and inorganic substances. The technique is based on the interaction of infrared light in the wavenumber range 4000-400 cm⁻¹ with the sample.



Figure 42: FTIR spectrometer Nicolet 6700.

Samples of composite pastes and mortars were ground in a Retch MM 400 oscillating ball mill at a frequency of 30 Hz (1800 oscillations/min) and dried to a steady weight. The

samples were measured on a Nicolet 6700 spectrometer (Thermo Fisher Scientific Inc., Massachusetts, USA), which was equipped with reflectance attachment in the ATR sampling tool performance using diamond crystal. The equipment consists of a HeNe laser, an EverGlo™ high-intensity IR source, an interferometer with a KBr beam splitter, movable and static mirrors covered with gold foil, an HP DLaTGS pyroelectric detector, and a removable tray with the material under test. Spectra were collected after 32 scans at 4 cm^{-1} resolution in absorbance mode. The spectral regions were normalized to enable comparison of individual samples and peak deconvolution using Gaussian peak fitting was performed, in order to evidence the stretching mode contribution of the different functional groups. Deconvolution of bands, fitting with Gaussian function, in the IR spectra was done using Thermo Fisher Scientific Inc. software OMNIC 8.3.103, 1992-2011.

4.3.3.3 Morphology of Hardened Samples

In the presented study, two types of scanning electron microscope (SEM) were used to determine the surface morphology equipped with an energy-dispersive X-ray spectroscopy (EDS) detector to identify the chemical composition of measured materials.

The first was Tescan Lyra 3 (TESCAN GmbH, Dortmund, Germany) with a dual beam system with an FEG electron source and an EDS analyser with a silicon drift detector (SDD) detector. The second apparatus was Phenom™ XL G2 (Thermo Fisher Scientific Inc., Massachusetts, USA) with a CeB_6 electron source, also equipped with an SDD detector.

4.3.4 Material Characteristics Analysis

4.3.4.1 Flow Table Test

The workability and consistency of the fresh mortar were specified using the flow table test according to EN 1015-3 [138]. During this test, the mortar was placed in a cone-shaped mould on a flow table. The cone was half-filled with the mixture and compacted 10 times with a tamping rod. The mould was then filled and compacted again. The mould was then removed, and the table was raised by 12.5 mm and dropped 15 times in 15 seconds. The diameter of the spread of the mixture was measured in two perpendicular directions using a tape measure.



Figure 43: Flow table test.

4.3.4.2 Bulk Density

Among basic structural properties, the bulk density ρ_v ($\text{kg}\cdot\text{m}^{-3}$) and the specific density ρ_{mat} ($\text{kg}\cdot\text{m}^{-3}$) were evaluated. Bulk density measurement was based on the gravimetric method in accordance with standard EN 1015-10 [139]. At least five hardened specimens in prismatic shape (40 mm x 40 mm x 160 mm) were dried in a vacuum chamber at 60 ± 5 °C until a steady-state mass was reached. The mass of the samples was measured using an analytical scale with an accuracy of ± 0.01 g. The volume of the samples was measured with a digital calliper with a precision of ± 0.01 mm. The expanded combined uncertainty of this test was 1.4 %.

$$\rho_v = \frac{m}{V} \quad (3)$$

where m (kg) is the dried mass and V (m^3) is the volume measured of the specimen.

4.3.4.1 Specific Density

The specific density was evaluated with the pycnometry method using the Pycnomatic Helium Pycnometer ATC, Thermo Scientific™. The samples were similar to those of the previous measurement and dried in a vacuum chamber to steady-state mass. The volume of material matrix was evaluated as a comparison of the measurement chamber volume with the porous specimen and the reference chamber, the known helium pressure in each chamber, and the known atmospheric pressure. The final density was measured by equation 2 similarly to the bulk density. The expanded combined uncertainty of this test was 1.2 %.



Figure 44: Helium pycnometer Pycnomatic ATC.

4.3.4.2 Total Open Porosity

The total open porosity ψ (%) was calculated from the known bulk density and the specific density using the equation:

$$\psi = \left(1 - \frac{\rho_v}{\rho_{mat}}\right) \cdot 100 \quad (4)$$

where ρ_v ($\text{kg}\cdot\text{m}^{-3}$) is the bulk density and ρ_{mat} ($\text{kg}\cdot\text{m}^{-3}$) is the specific density measured. The expanded combined uncertainty of this test was 2.0 %.

4.3.4.3 Mercury Intrusion Porosimetry (MIP)

Mercury intrusion porosimetry (MIP) was used in some cases to measure the pore size distribution of samples dried to a steady mass. The analysis consisted of two measurement modules. The first, Pascal 140, performs low-pressure porosimetry from vacuum to 400 kPa, measuring large pores (pore size 116 - 3.8 μm). It is coupled to a second high-pressure module, Pascal 440, which reaches 400 MPa and allows the measurement of very small pores (pore size 15 - 0.0036 μm). Prior to the test, the samples were dried to a constant weight. The measurement was based on mercury intrusion into small fragment of material. The volume of mercury intruded into material pores and the pressure was recorded and pore size d_p (m) calculated by the Washburn equation:

$$f_f = \frac{3 \cdot F \cdot l}{2 \cdot b \cdot h^2} \quad (5)$$

where p (Pa) is the measuring pressure, γ (N/m) surface tension of mercury and θ ($^\circ$) is the contact angle.

The measurements resulted in distribution and cumulative pore size curves calculated and evaluated with Thermo Fisher Scientific Inc. software SOLID EVO Solver of Intrusion Data 1.4.0.



Figure 45: MIP apparatus Pascal 140 and 440.

4.3.5 Mechanical Strength Analysis

4.3.5.1 Flexural and Compressive Strength Test

Mechanical strength was analysed on six 28-day cured prismatic samples (40 mm \times 40 mm \times 160 mm) according to the EN 1015-11 standard [140] with expanded combined uncertainty 1.4 % for both tests. The flexural strength f_f (MPa) was measured in a three-point bending set-up with a mechanical press FP 100 (Heckert, Germany) with load capacity 100 kN. The specimen was placed in a holder with two supports 100mm apart and a middle loading pin. The maximum force at the specimen break and its dimensions were used for f_f calculation by equation:

$$f_f = \frac{3 \cdot F \cdot l}{2 \cdot b \cdot h^2} \quad (6)$$

where F (N) is the maximum force at the specimen breakage, l (mm) is the span of supports in the three-point bending setup, b (mm) and h (mm) are the dimensions of the cross section of the sample.



(A)



(B)

Figure 46: Flexural strength A) and compressive strength B) testing setup.

The compressive strength test f_c (MPa) was performed on fractions of prismatic samples from the flexural strength test. Due to the different strength characteristics of lime-based and lightly burnt magnesite materials, two presses were used to measure the maximum failure force of the specimen. A mechanical press FP 100 (Heckert, Germany) with a maximum loading force of 100 kN for lime-based plasters and a hydraulic press ED 600 (Heckert, Germany) with a maximum force of 600 kN for MgO-based mortar. In both cases, the maximum force applied to a loading area 40 mm x 40 mm at a loading rate of 500 N/s. The compressive strength was calculated as follows:

$$f_c = \frac{F}{b \cdot h} \quad (7)$$

where F (N) is the maximum force at the specimen breakage, b (mm) and h (mm) are the dimensions of the loading area (maximum 40 mm x 40 mm).

4.3.5.2 Modulus of Elasticity

Three air-dried prismatic samples (40 mm x 40 mm x 160 mm) were used for the measurement of the dynamic modulus of elasticity E (GPa) using ultrasound testing

apparatus Vikasonic (Schleibinger Geräte GmbH, Buchbach, Germany). This is a non-destructive test based on the detection of the speed of ultrasonic wave velocity. The measured sample was sandwiched between two circular probes, an ultrasonic wave transmitter and a receiver. The contact between the sample surface and the probe was ensured by a sonogel.



Figure 47: Ultrasonic data logger – Vikasonic.

The instrument recorded the time of passage of the ultrasonic waves at frequency 54 kHz through the sample from the transmitter to the receiver. The velocity of the ultrasonic wave and subsequently the dynamic modulus of elasticity were calculated from the wave time according to EN 12504-4 [141] with the expanded combined uncertainty of this test being 2.3 % by the equation:

$$E = \rho_v \cdot v^2 \quad (8)$$

where ρ_v ($\text{kg}\cdot\text{m}^{-3}$) is the bulk density and v ($\text{m}\cdot\text{s}^{-1}$) is the transit time of the ultrasonic wave, calculated by:

$$v = \frac{a}{t} \quad (9)$$

where a (m) is the length of the sample between both probes and t (s) is the measured ultrasonic wave transit time.

4.3.6 Thermophysical Properties

The thermal properties of the investigated materials were measured using the non-stationary, transient plane source method (transient plane source method-TPS). With the Hot-Disk apparatus TPS 1500 (HotDisk AB, Göteborg, Sweden). The TPS method is capable for determining the thermal conductivity in the range of 0.005 to 1800 $\text{W}\cdot\text{m}^{-1}\cdot\text{K}^{-1}$, diffusivity, and specific heat capacity. These parameters can be measured at room temperature and elevated temperatures.



Figure 48: Hot-Disk apparatus setup.

The measuring setup consists of a measuring probe, a hot-disk instrument, a sample holder, and a computer containing the control and calculation programme. Six prismatic specimens (40 mm x 40 mm x 160 mm), two for each measurement were measured. The probe, which serves as both a heat source and a temperature sensor, is placed between two pieces of the sample to be measured or one piece of the sample and the thermal insulation. An electrical current sufficient to heat the probe (200 mW for MgO-based mortars and 100 mW for lime-based mortars) is sent to the probe while its temperature and the response of the entire system being measured. The recorded temperatures (200 points) were plotted as the function of the time of measurement (40 seconds). Thermal characteristics were then calculated from this plot using Hot Disk AB software Thermal Constant Analyser 7.5.15.

4.3.7 Water Absorption Characteristics

The water absorption coefficient A_w ($\text{kg}\cdot\text{m}^{-2}\cdot\text{s}^{-1/2}$) and the 24-hour water absorption W_a ($\text{kg}\cdot\text{m}^{-2}$) were measured as part of the capillary water absorption characteristics

according to the EN 1015-18 standard [142]. Three cube-shaped specimens (40 mm side) for all tested materials were dried to a constant weight before measurement. The measurements are based on the principle of 1D capillary absorption; for this reason, the samples were insulated around the outer perimeter with epoxy resin. The sample was attached to a hanger and immersed in water to a depth of 1-2 mm from its bottom edge. The increase in the weight of the sample was recorded as a function of time.



Figure 49: Water absorption measurement.

The absorption coefficient for water was determined from the trend of the cumulative water absorption function I ($\text{kg}\cdot\text{m}^2$) function related to the absorption area according to the formula:

$$I = A_w \cdot t^{1/2} \quad (10)$$

where A_w ($\text{kg}\cdot\text{m}^{-2}\cdot\text{s}^{-1/2}$) is the water absorption coefficient, t (s) is the time of water absorption. The expanded combined uncertainty of this test was 2.3 %.

24-hour water absorption W_a ($\text{kg}\cdot\text{m}^{-2}$) was calculated by:

$$W_A = \frac{m_{24h} - m_{dry}}{a \cdot b} \quad (11)$$

where m_{24h} (kg) is the weight of the sample after 24-hour water absorption, m_{dry} (kg) is the weight of the sample in the dry state, a (mm) and b (mm) are the dimensions of the absorption area. The expanded combined uncertainty of this test was 2.3 %.

4.3.8 Cost-Effectivity of Nano-Additive

The cost-effectivity evaluation was based on concrete cost-benefit analysis in studies by J. Pan et al. and H. Mahzuz et al. [143, 144]. In our case, the calculation considering only the cost of the nano-additive and any chemicals used versus the improvement in compressive strength and flexural strength. The unit cost of additive per 1 m³ of material was evaluated and the ratio between the enhancement cost and the strength improvement was evaluated by the enhancement of the strength per the cost of material modification (kPa·€⁻¹) by equation:

$$\text{strength enhancement / modification cost} = \frac{f_{enhanced} - f_{control}}{CPU} \quad (12)$$

where CPU is cost per unit (€), in this case 1 m³ and $f_{control}$ (kPa) and $f_{enhanced}$ (kPa) are measured mechanical strength values of control mixture and enhanced mixture, respectively.

5 Results and Discussion

5.1 High purity MOC

This chapter discusses the results of the characteristics of the measured 28-days cured hardened composites based on MgO with high purity.

5.1.1 Influence of the Two-step Homogenisation Technique

The following section focusses on the resulting MOC properties of the composite modified with GNs. Specifically, a two-step homogenisation method was used in which the composite paste was additionally homogenised using a high-shear mixer.

Fig. 50 shows diffraction patterns of 14-day old mixtures obtained with XRD analysis. As a result of their very low content, GNs were not visible in the diffraction patterns. The results are similar between each mixture, show only the presence of the crystalline phase $\text{Mg}_3(\text{OH})_5\text{Cl} \cdot 4\text{H}_2\text{O}$ (ICDD 04-014-8836), corresponding to the stoichiometry of the crystalline phase MOC Phase 5.

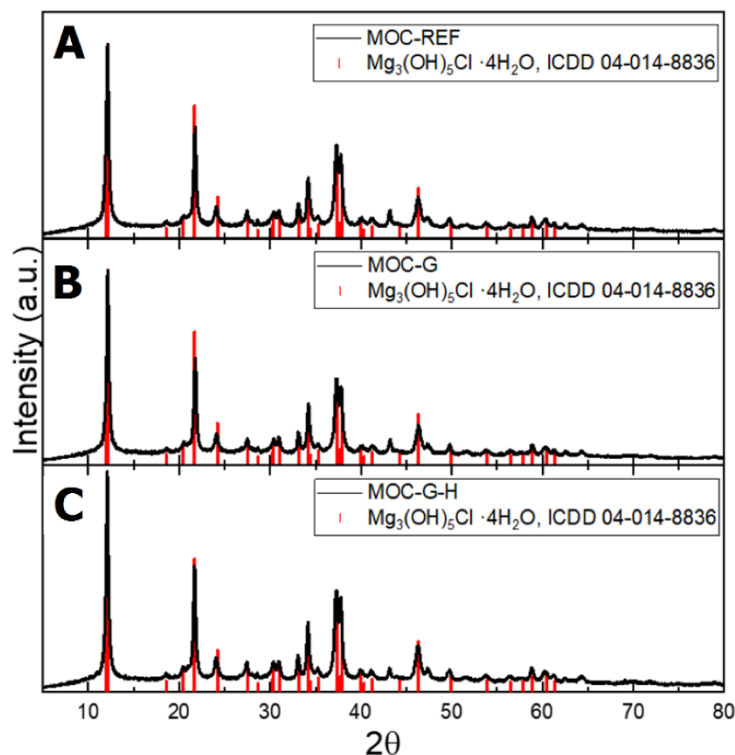


Figure 50: XRD analysis: A) MOC-REF, B) MOC-G, and C) MOC-G-H.

The microstructure of 14-day-cured hardened mixtures characterised by SEM micrographs are shown in Fig. 51. Even in this analysis, the GNs were not visible. Taking into account the significant effect of the improvement of the material strength, the analysis occurred in the fractured area of the sample, that is, in the area with lower

concentrations of GN. The images show the presence of the crystalline phase MOC Phase 5, typical needle-shaped crystals with 1-6 μm in length and thickness approx. 0.5 μm .

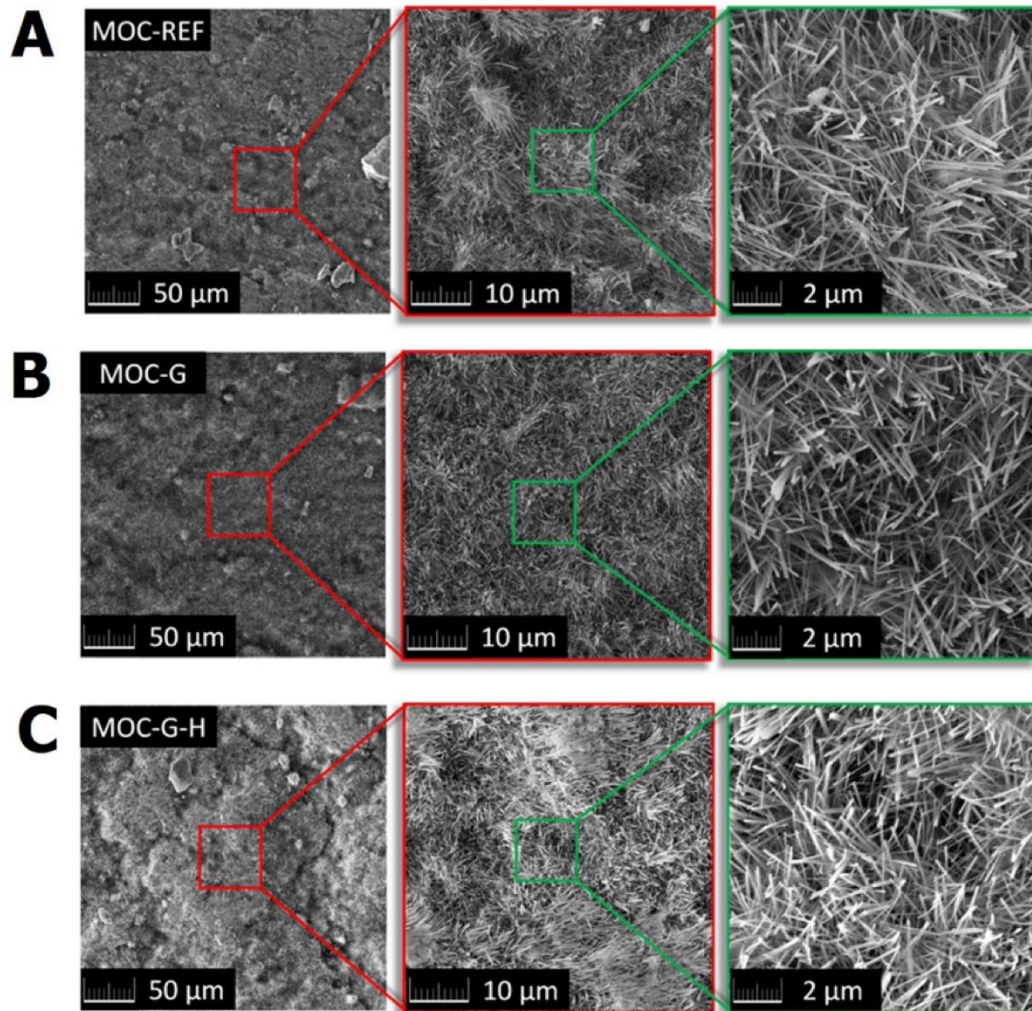


Figure 51: Micrographs of samples: A) MOC-REF, B) MOC-G, and C) MOC-G-H.

In the case of the EDS elemental maps to obtain the chemical composition, Fig. 52, the presence of Mg, O, Cl, and C was detected. The compositions obtained were similar for all samples and corresponded to the stoichiometry of phase 5 of the high-purity MOC composite. A relatively higher carbon content was found, probably due to the surface reaction with carbon dioxide to form chlorartinite [145]. Clusters of carbon were also noted in the images, marking areas of inhomogeneity in the mixture.

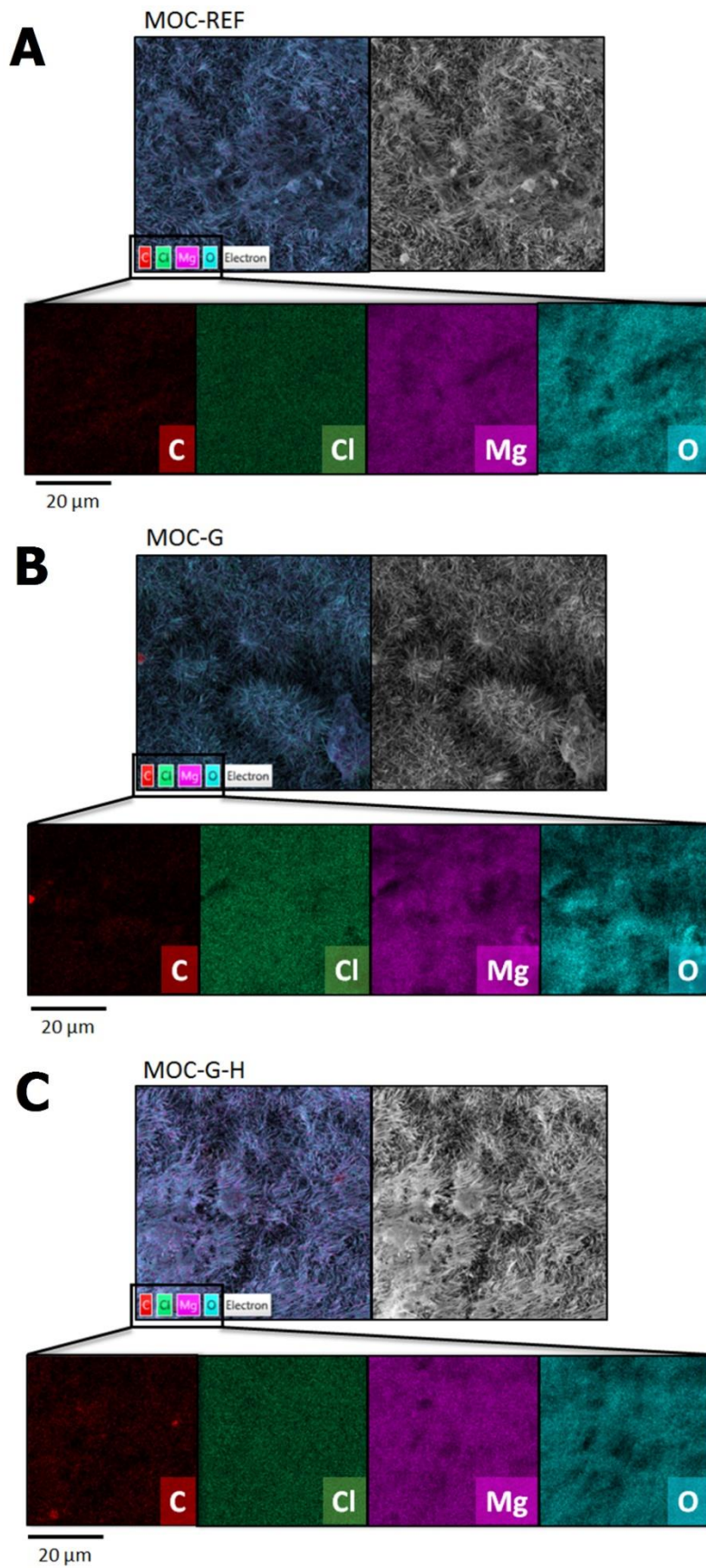


Figure 52: EDS elemental maps of the samples: A) MOC-REF, B) MOC-G, and C) MOC-G-H.

The obtained FT-IR spectral lines are presented in Fig. 53. All samples analysed contained the O-H, Mg-Cl and Mg-O bands that come from the fundamental vibrations of the structural H_2O , MgCl_2 , $\text{Mg}(\text{OH})_2$ and $\text{MgCl}_2 \cdot 8\text{H}_2\text{O}$ molecules. Although the absorption bands between 3700 and 3600 cm^{-1} can be attributed to the OH bonds in the hydroxyl group in $\text{Mg}(\text{OH})_2$, the broad absorption band with a maximum at $3375\text{-}3346 \text{ cm}^{-1}$ is due to the vibration of the OH bonds in the hydroxyl group in water. In the cases of the band intensities at 1646 , 1608 and 1157 cm^{-1} , these are bending vibrations of the O-H bonds in the hydroxyl group in $\text{Mg}(\text{OH})_2$. At 1622 and 1429 cm^{-1} stretching vibrations of Mg-O in $\text{MgCl}_2 \cdot 8\text{H}_2\text{O}$ can be observed. Several modes in the wavelength range $1000\text{-}400 \text{ cm}^{-1}$ come from the lattice translational vibration of Mg-OH and vibrational vibrations of the Mg-O/ Mg^{2+} , O/O-Mg-O/O- Mg^{2+} -O bonds. The modes of lattice vibration of the Mg-O/Mg-Cl bonds around a wavelength of 500 cm^{-1} can be caused by the vibration of both the Mg-Cl and Mg-O bonds. The analysed spectrum of graphene reveals only one weak line, which appears at 1586 cm^{-1} and can be assigned to the stretching of the C=C bond. In the case of the MOC composites, this line shifts to higher wavenumbers, specifically to 1611 cm^{-1} . This line also partially overlaps with the intense Mg-O band stretching line in $\text{MgCl}_2 \cdot 8\text{H}_2\text{O}$. Based on this phenomenon, it was observed that the optimum resolution is 1611 cm^{-1} for the MOC-G and MOC-G-H samples.

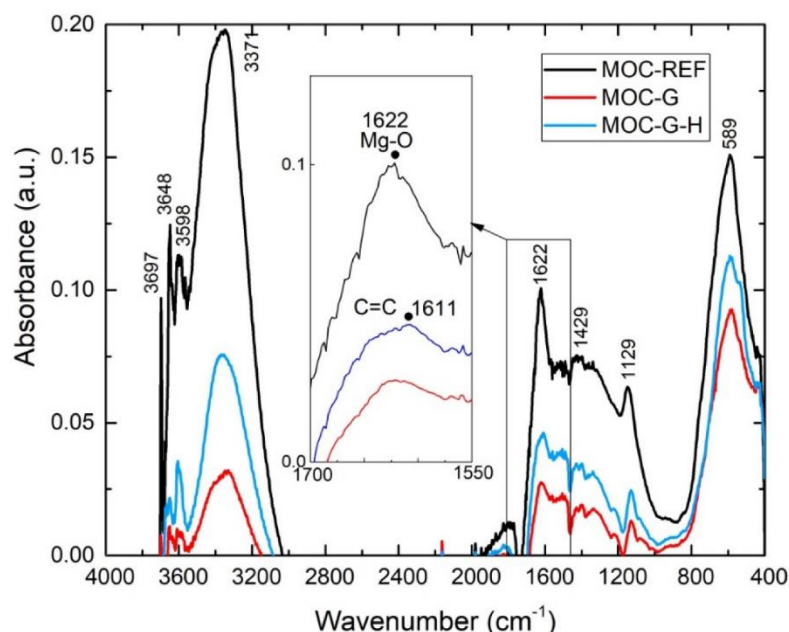


Figure 53: The MIR (Mid-infrared) spectra of MOC-REF, MOC-G3 and MOC-G-H.

A summary of the assignment of the main absorption bands is provided in Tab. 26.

Table 26: Assignments of the major absorption bands of MOC composites.

Wavenumber (cm ⁻¹)	Assignment
3697, 3648, 3598	stretching (ν) vibration of O-H in Mg(OH) ₂
3375-3346	stretching (ν) vibration of H-O-H in H ₂ O
1646, 1608, 1157	bending (δ) vibration of H-O-H in MgCl ₂ ·8H ₂ O
1622, 1429	stretching (ν) vibration of Mg-O in MgCl ₂ ·8H ₂ O
1611	stretching (ν) vibration of C=C
844	stretching (ν) vibration of the Mg-O cubic structure
668, 634	stretching (ν) vibrations of Mg-O
589	deformation (δ) and stretching (ν) lattice vibrations of Mg-Cl/Mg-O
535	translation vibrations of Mg/Mg-O, Mg-OH
440	vibrational modes of the lattice showing the Mg-O/Mg ²⁺ , O/O-Mg-O/O-Mg ²⁺ -O bonds

The basic structural parameters of the cured compounds are shown in Tab. 27 and 28. At both curing times, the effect of graphene additive on composite porosity was evident. Furthermore, the two-step mixing method allowed a further reduction of the porosity. The reduction in porosity measured for 14-day-old samples was 21% for MOC-G and 33% for MOC-G-H (relative value), which clearly describing the effectivity of the designed homogenisation procedure. The results of the 14-day mixtures were complemented by porosity measurements using mercury intrusive porosimetry. The differences in bulk density and specific density were small, but compared to the reference material, the bulk density was typically higher for graphene-enriched composites; in contrast, specific gravity was reduced by incorporating nano-additives into the composite mixture.

Table 27: Two-step homogenization: Basic structural parameters of 7-days cured pastes.

Mixture	Bulk density ρ_b (kg·m ⁻³)	Specific density ρ_s (kg·m ⁻³)	Porosity ψ (%)
MOC-REF	1603 ± 23	1867 ± 23	14.2 ± 0.3
MOC-G300	1680 ± 22	1854 ± 22	11.2 ± 0.2
MOC-G750	1654 ± 22	1848 ± 22	10.5 ± 0.2

Table 28: Two-step homogenization: Basic structural parameters of 14-days cured pastes.

Mixture	Bulk density ρ_b ($\text{kg}\cdot\text{m}^{-3}$)	Specific density ρ_s ($\text{kg}\cdot\text{m}^{-3}$)	Porosity ψ (%)
MOC-REF	1633 \pm 22	1887 \pm 23	13.5 \pm 0.3
MOC-G300	1658 \pm 23	1857 \pm 22	10.7 \pm 0.2
MOC-G750	1652 \pm 23	1818 \pm 22	9.1 \pm 0.1

The pore size distribution curves obtained by mercury intrusion porosimetry of 14-day-old samples are shown in Figs. 54 and 55. Microstructural data seem to agree with the total porosity data given in Tab. 28. The differences between the total porosity data obtained by the MIP technique and those calculated from the bulk and specific density values are small, especially considering the sample size and the principles of the applied techniques.

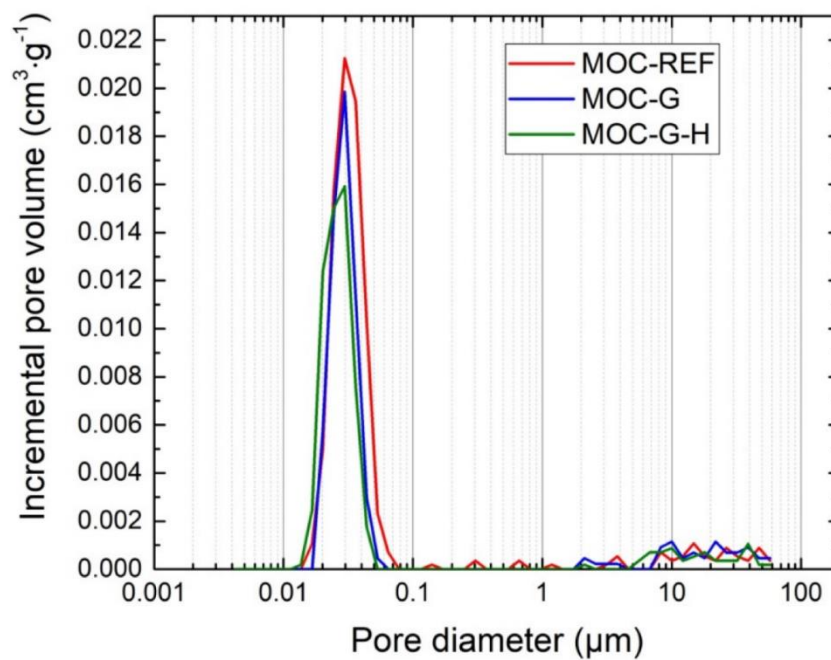


Figure 54: Two-step homogenization: Incremental pore volume distribution for 14-day composites.

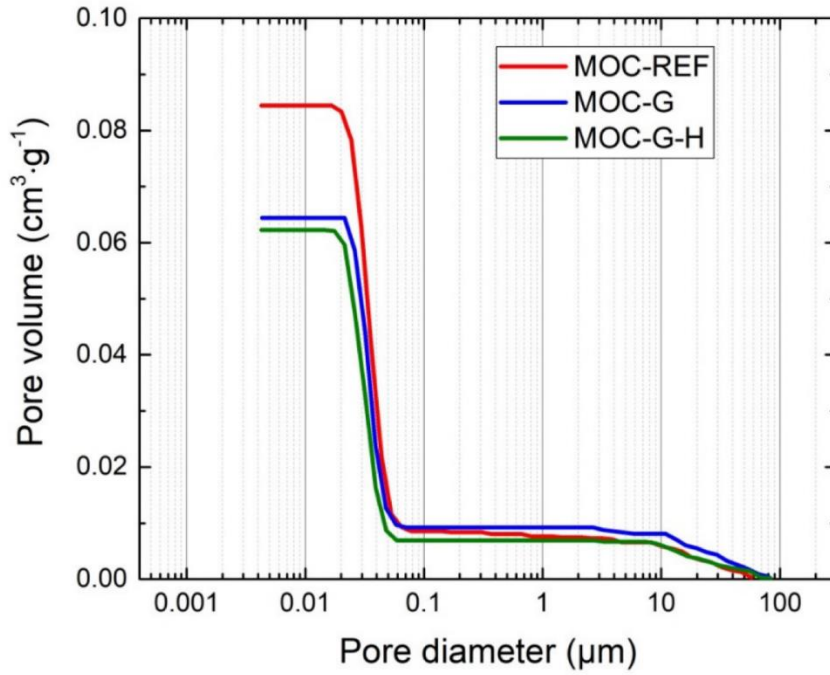


Figure 55: Two-step homogenization: Cumulative distribution of the pore volume for 14-day composites.

The microstructural parameters of the 14-day cured samples are listed in Tab. 29. The pore volume decreased visibly with the application of graphene, but the average pore size increased slightly for materials containing GNs compared to the control mixture. This was caused by an increase in the volume of the pores in the diameter range of 100-10 µm and a decrease in the volume of the nanosized pores (5-35 nm).

Table 29: Two-step homogenization: Microstructural parameters of the 14-day composites.

Parameter	MOC-REF	MOC-G	MOC-G-H
Hg porosity (%)	13.4	10.4	9.8
Total pore volume (cm ³ ·g ⁻¹)	0.0844	0.0644	0.0622
Average pore diameter (µm)	0.0295	0.0317	0.0320

The investigated mechanical strength parameters, presented in Fig. 11, the addition of GNs had a noticeable effect on the mechanical resistance of the hardened composites, in addition to the already general high compressive strength and flexural strength, exhibited by the control MOC mixture, similarly to other studies focused on this type of material [146, 147].

The use of nano-additives in the form of GNs significantly improved both compressive and flexural strength, which corresponded well with the measured total porosity and pore size distribution data. When comparing the mechanical properties with the control mixture, a remarkable increase in compressive strength is observed, already remarkable

at 7 days. For these samples, the increase in compressive strength was 34.6% and 53.6% for MOC-G and MOC-G-H, respectively. Similarly, for the 7-day specimens, the increase in flexural strength was 57.1% and 65.9% for the MOC-G and MOC-G-H composites, respectively. For the 14-day old specimens, the increase in compressive strength values was 28.6% for the MOC-G composites and 36.6% for the MOC-G-H composites. The results of the flexural strength showed an increase in flexural strength of 57.4% for the MOC-G composite and 61.4% for the MOC-G-H composite.

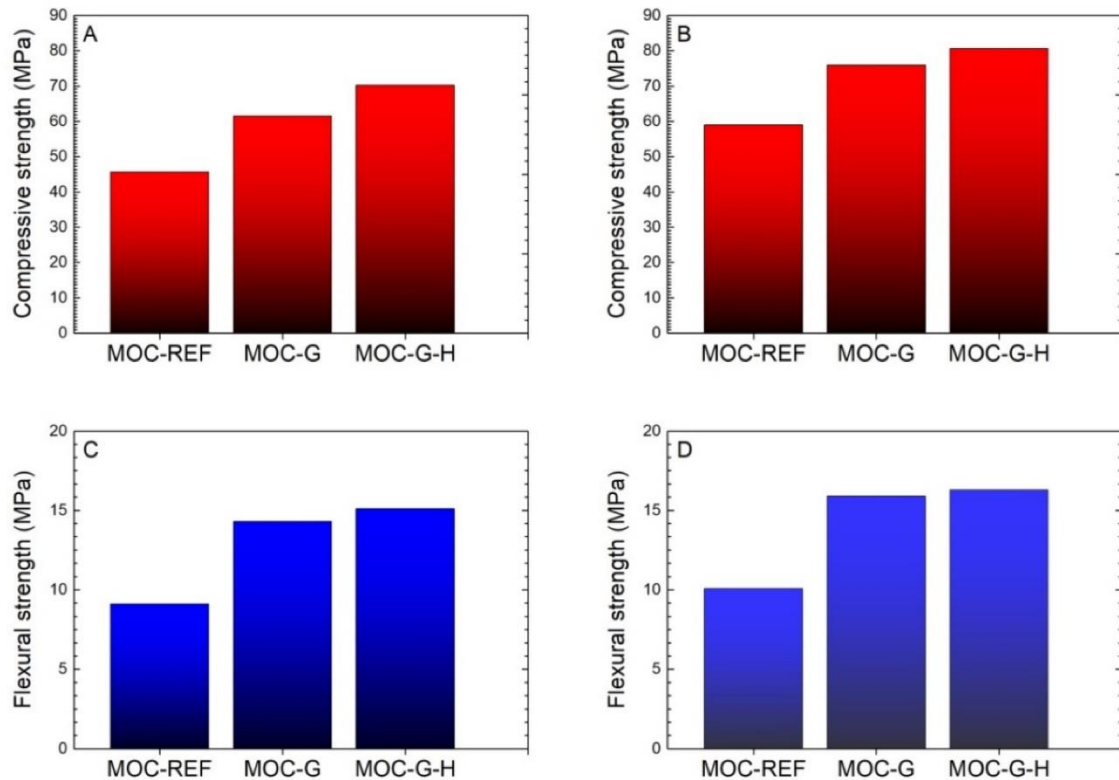


Figure 56: Mechanical strength: A) compressive strength of 7-day samples; B) compressive strength of 28-day samples; C) flexural strength of 7-day samples; D) flexural strength of 28-day samples.

From the results, it was observed that the two-step homogenization technique led to an increase in compressive strength. However, the improvement in flexural strength due to the homogenisation procedure was not large. It is evident that the two-step homogenisation procedure improved the distribution of graphene particles in the fresh MOC mixture, which in turn led to an improvement in the parameters of the reinforced composites. For all the composites investigated, the extended curing time significantly increased both mechanical parameters studied. The results were in agreement with the findings of other authors who reported the evolution of the strength of MOC mixtures with curing age [148]. This was due to the solidification of the precipitated MOC phases, that

is, the free growth of the crystalline phases and the thickening of the composite microstructure [149]. However, then the mass transport in the studied materials and their durability are estimated, it is necessary to consider the fact that porosity significantly affects mechanical strength, while transport processes depend on the structure and distribution of pore sizes.

Table 30: Two-step homogenization: Cost-effectivity of additive.

Mixture	Additional cost per m ³ (€)	Flexural strength f_f (MPa)	Compressive strength f_c (MPa)	Cost-effectivity in comparison of:	
				f_f	f_c
				(kPa·€ ⁻¹)	(kPa·€ ⁻¹)
MOC-REF	-	8.2	59.9	-	-
MOC-G	7453	12.9	77.0	0.63	2.30
MOC-G-H	7453	13.2	81.8	0.67	2.94

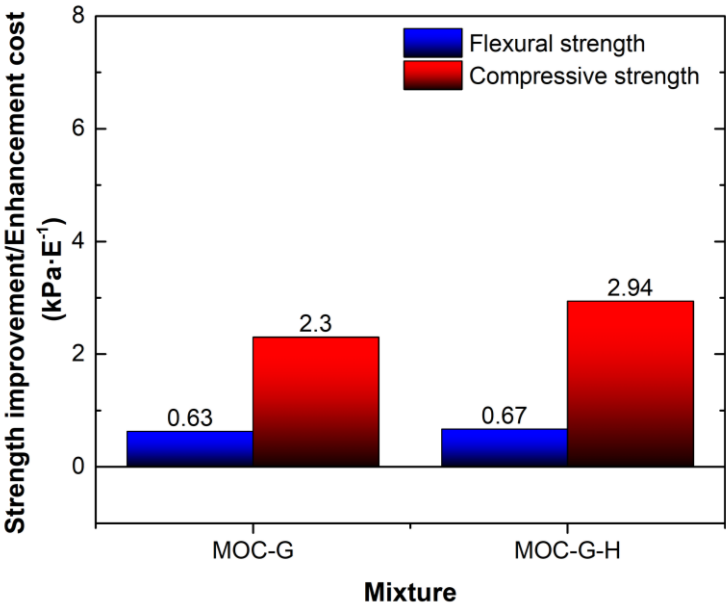


Figure 57: Two-step homogenization: Cost-effectivity ratio.

The cost effectivity of the nano-additive as a ratio of the improvement in mechanical resistance and the price of the NM used is presented in Tab.30 and Fig. 57. The resulting values basically indicate what improvement in kPa strength can be obtained for the price of 1 €. The detailed calculation of cost-effectivity is listed in Annex B.

Since the only variables were the preparation methods of the mixtures, the total price of the enhancement was the same for both admixtures. The results were only affected by the advantageous properties of the mixtures, namely the improvement in strength. With respect to flexural strength, the resulting cost-effectivity is practically the same. In

the case of compressive strength, higher strengths were achieved at the same cost; thus, the two-step homogenisation preparation method appears to be the most effective.

5.1.2 Influence of NM's Specific Surface Area

In this part, the results of MOC composites with nano-additives with varying specific surface area were presented. These were two types of GNs with a specific surface area of $300 \text{ m}^2\text{g}^{-1}$ and $750 \text{ m}^2\text{g}^{-1}$, prepared with the two-step homogenisation method studied in the previous chapter. The results of the XRD analysis are shown in Fig. 58.

As in the previous chapter, only one crystalline phase was observed, the MOC phase $5 \text{ Mg(OH)}_2\cdot\text{MgCl}_2\cdot 8\text{H}_2\text{O}$ (ICDD 04-014-8836) were was observed in all three measured mixtures. Because of the low volume of applied GNs, it was not visible in the diffraction pattern. Therefore, no differences are observed between the different mixtures.

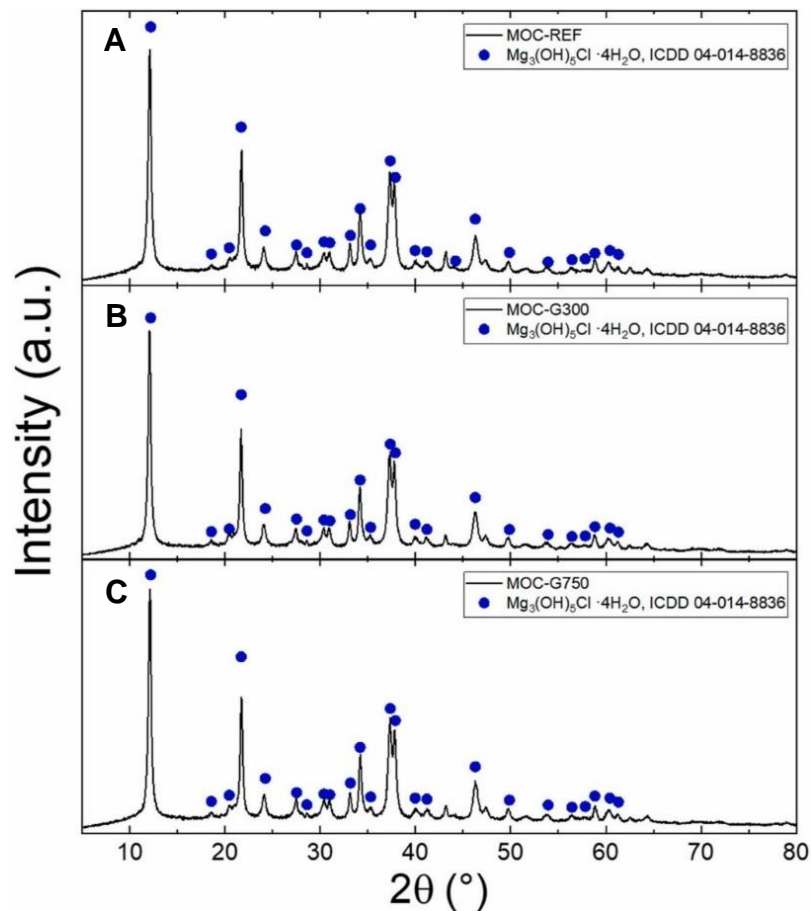


Figure 58: XRD analysis: A) MOC-REF; B) MOC-G300 and C) MOC-G750

The SEM analysis of the sample microstructure is shown in Fig.59. Again, images revealed typical needle-shaped crystals of MOC composite with $\sim 1\text{--}5\ \mu\text{m}$ length and $50\text{--}150\ \text{nm}$ width. Unfortunately, no signs of GNs were visible in these images.

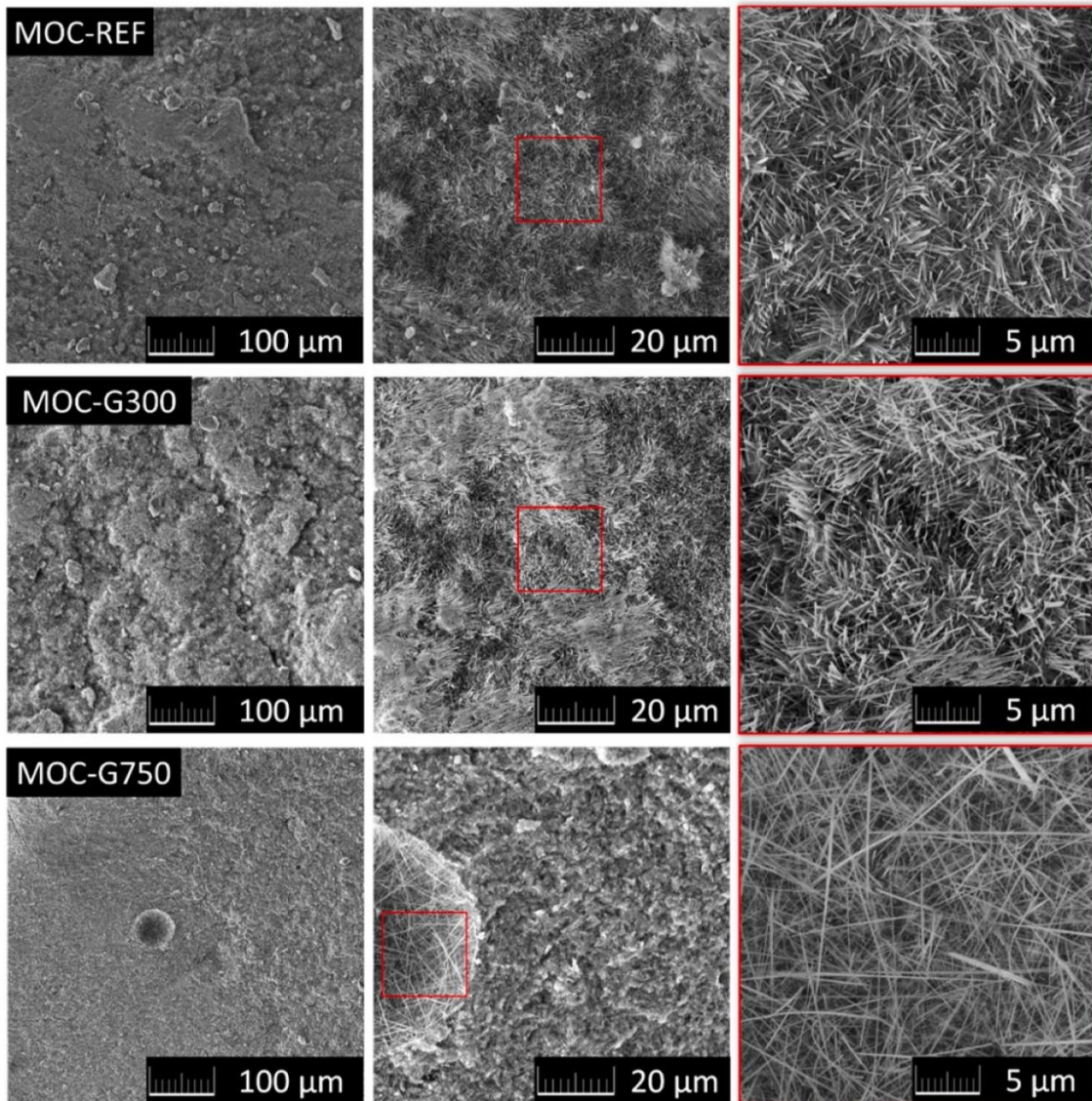


Figure 59: Micrographs of samples: MOC-REF, MOC-G300, and MOC-G750.

The chemical composition of the prepared samples in the form of elemental maps, studied using EDS, is shown in Fig. 60. This analysis has shown the presence of magnesium, chlorine, and oxygen and carbon. In the case of carbon, the maps show an even distribution of it, probably because of surface reaction with carbon dioxide in addition to the GNs distribution. Furthermore, the MOC-G300 and MOC-G750 maps reveal signs of NM clusters in the morphology of the material.

A relatively higher carbon content was found, probably due to the surface reaction with carbon dioxide to form chlorartinite. Clusters of carbon were also observed in the images, marking areas of inhomogeneity in the mixture.

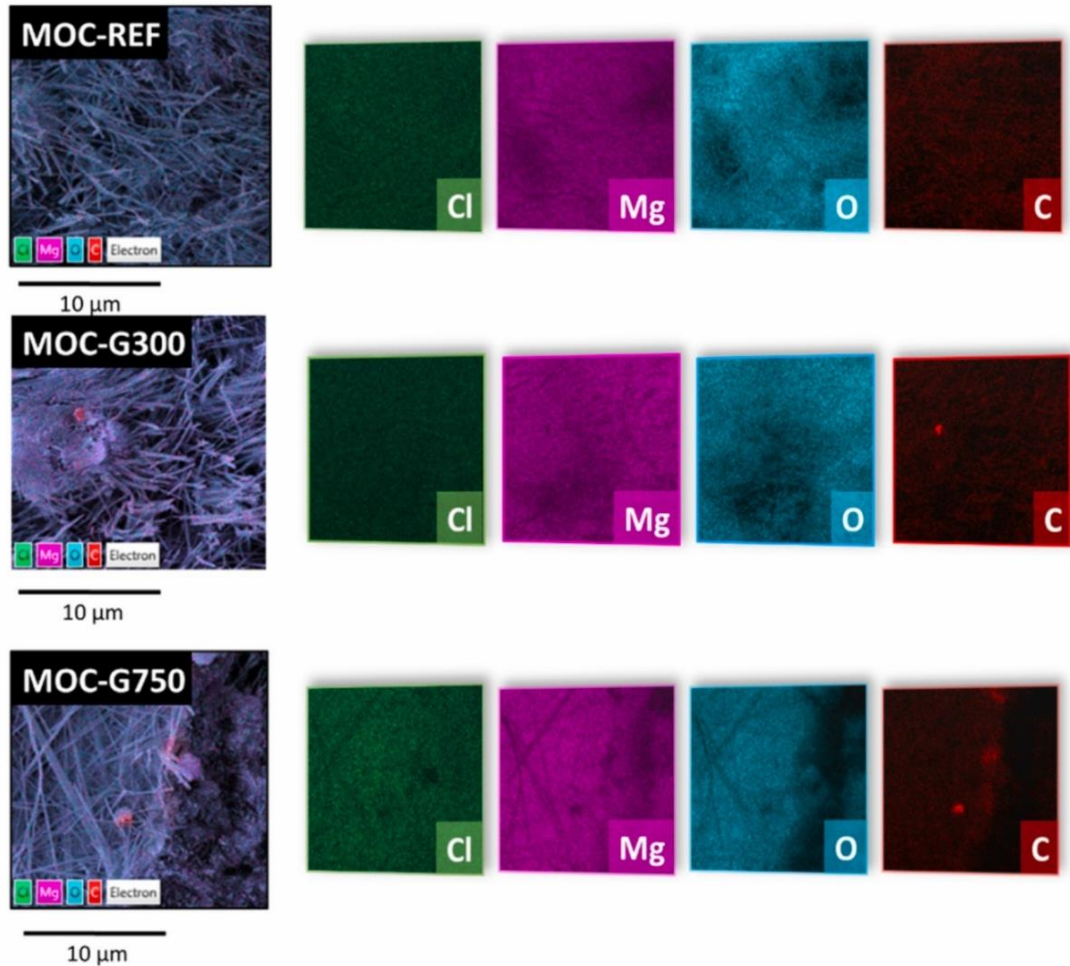


Figure 60: EDS elemental maps of the samples: MOC-REF, MOC-G300 and MOC-G750.

In the case of both 7-day and 14-day hardened samples, the porosity drops with the addition of GNs. Furthermore, the application of C-750 GN resulted in a high decrease in porosity compared to the control mixture. For 7 days old samples, the reduction in total open porosity was by 2.1 % and 3.6 % (absolute value) for MOC-G300 and MOC-G750, respectively. As the samples cured for another 7 days for total 14 days of curing, porosity drops by 3.4 % and 5.0 % (absolute value) for MOC-G300 and MOC-G750 compared to the control mixture. The deviations of the bulk density and the specific density between the mixtures were marginal. The porosity measured by mercury intrusion porosimetry was almost like the total open porosity values calculated from both bulk and specific densities, given the differences in the size of the measured samples and the technique.

The basic structural parameters of composites in both curing ages are listed in Tab.31 and 32.

Table 31: NM's specific surface area: Basic structural parameters of 7-days cured pastes.

Mixture	Bulk density	Specific density	Porosity
	ρ_b (kg·m ⁻³)	ρ_s (kg·m ⁻³)	ψ (%)
MOC-REF	1603 ± 22	1867 ± 22	14.2 ± 0.3
MOC-G300	1630 ± 23	1854 ± 22	12.1 ± 0.2
MOC-G750	1662 ± 23	1864 ± 22	10.6 ± 0.2

Table 32: NM's specific surface area: Basic structural parameters of 14-days cured pastes.

Mixture	Bulk density	Specific density	Porosity
	ρ_b (kg·m ⁻³)	ρ_s (kg·m ⁻³)	ψ (%)
MOC-REF	1633 ± 23	1887 ± 23	13.5 ± 0.3
MOC-G300	1652 ± 22	1836 ± 22	10.1 ± 0.2
MOC-G750	1684 ± 22	1847 ± 22	8.8 ± 0.2

The pore size distribution is shown in Figs. 61 and 62. Both graphs correspond to the total porosity presented in Tab.33. The specific results of the pore size and volume are shown in Tab.33. It is obvious that the application of both GNs resulted in a great reduction in the specific volume of the pores throughout the diameter range (100–0.001 μm) with a decrease in the grater when C-750 was applied compared to the GNs C-300. Compared to the control sample, the total pore volume was reduced by 26.3 % and 37.7 % for MOC-G300 and MOC-G750, respectively.

Table 33: NM's specific surface area: Microstructural parameters of the 14-day composites.

Parameter	MOC-REF	MOC-G300	MOC-G750
Hg porosity (%)	13.4	9.8	8.4
Total pore volume (cm ³ ·g ⁻¹)	0.0844	0.0623	0.0529
Average pore diameter (μm)	0.0295	0.0291	0.0314

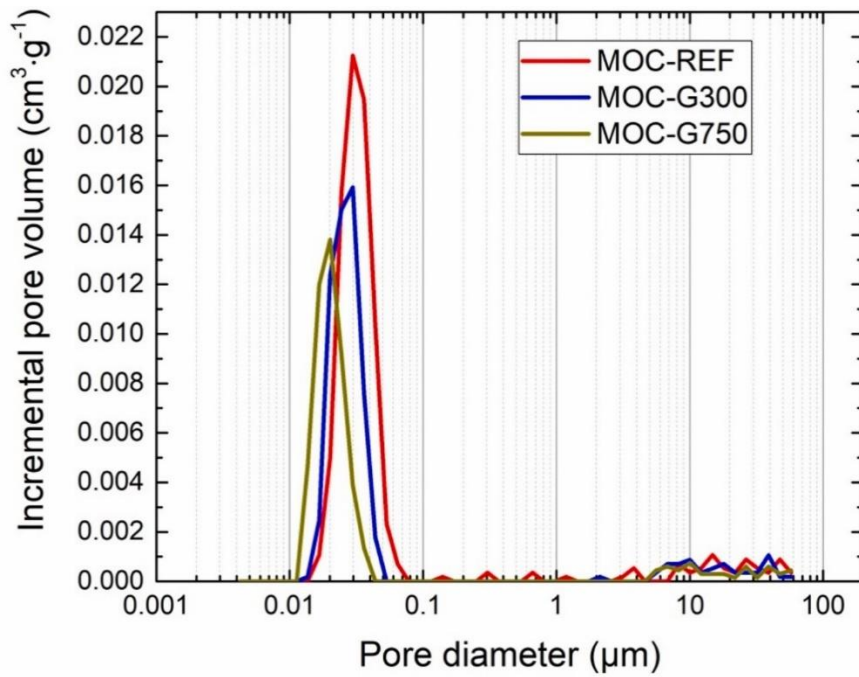


Figure 61: NM's specific surface area: Incremental pore volume distribution for 14-day composites.

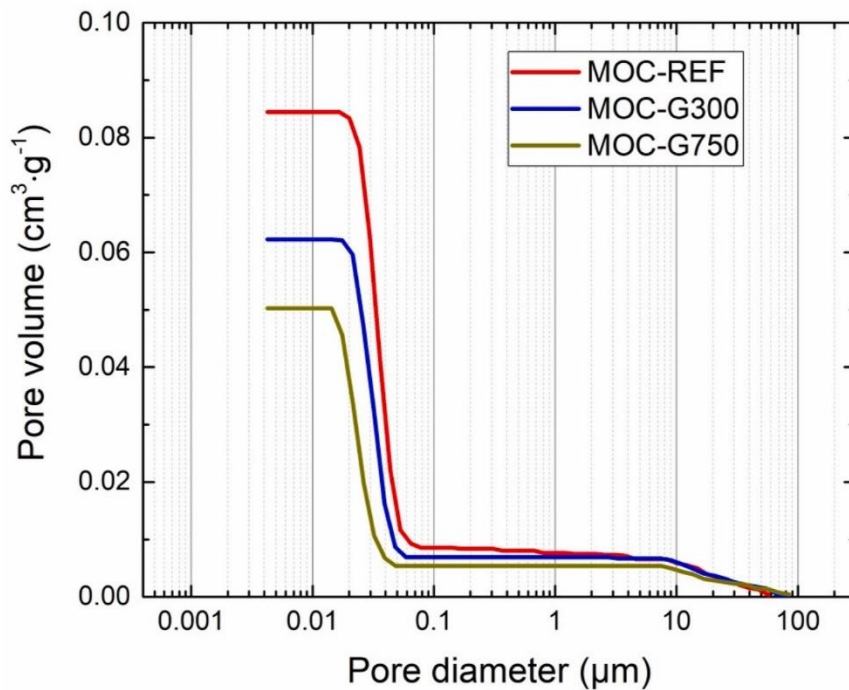


Figure 62: NM's specific surface area: Cumulative distribution of the pore volume for 14-day composites.

The resulting mechanical strength of enhanced composites improved greatly with the nano-additive GNs, which, due to their uniform distribution in the matrix, reinforce the interlocked MOC crystalline phases.

The mechanical strength parameters of the investigated mixtures are shown in Fig. 63. The 7-day samples of the GN-doped composites achieved an increased compressive strength of 31.2% and 42.7% for MOC-G300 and MOC-G750, respectively, in reference to the control mixture. Similarly, the flexural strength of the GN doped composites increased by 24.6% for MOC-G300 and 45.9% for MOC-G750. For samples cured for 14 days, the flexural strengths were 23.5% (MOC-G300) and 39.5% (MOC-G750) higher compared to the reference composite. The same was true for compressive strength. GN enhancement increased strength by 14.3% for MOC-G300 and 26.5% for MOC-G750.

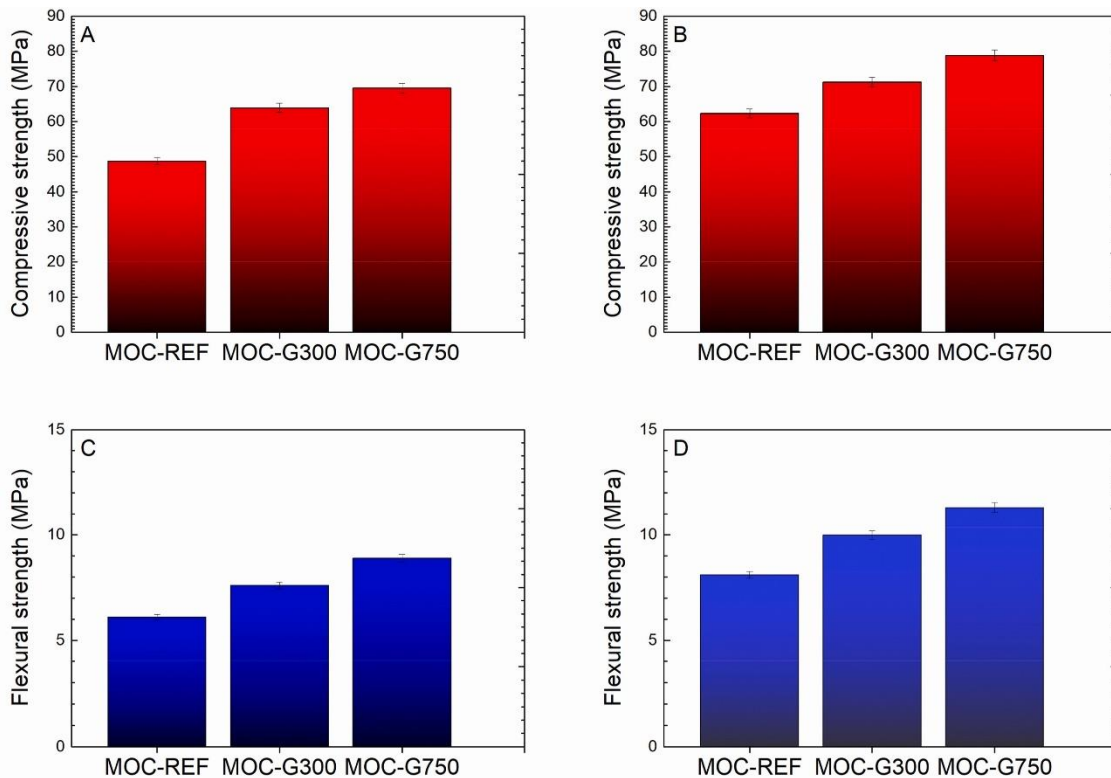


Figure 63: Mechanical strength: A) compressive strength of 7-day samples; B) compressive strength of 28-day samples; C) flexural strength of 7-day samples; D) flexural strength of 28-day samples.

With the curing time, the reinforcing effect of the GNs decreased slightly but still achieved a high efficiency in improving the mechanical behaviour of the investigated composites. The mechanical properties turned out as expected, in accordance with the basic structural and microstructural parameters reported above. Even the decrease in overall porosity contributed to the increase in flexural and compressive strength, with a reduction in the volume of capillary pores (0.01-10 μm in diameter), which are responsible for mechanical strength and one of the causes of improvement in mechanical resistance. However, the results of the observed mechanical resistance were the result

of two combined factors induced by the application of GNs: i) reduction of the pore size and volume, and ii) incorporation of graphene with excellent mechanical properties [150].

Strength characteristics varied significantly with time, consistent with the results of a previously reported study [151]. In this case, the pure MOC phases typically reached their maximum values as early as 10 days of maturation, with no other significant changes over time. On account of this fact, it was possible to measure the properties of the material when it reached 14 days of maturation and consider the parameters obtained as definitive.

Table 34: NM's specific surface area: Cost-effectivity of additive.

Mixture	Additional cost per m ³ (€)	Flexural strength f_r (MPa)	Compressive strength f_c (MPa)	Cost-effectivity in comparison of:	
				f_r (kPa·€ ⁻¹)	f_c (kPa·€ ⁻¹)
MOC-REF	-	8.2	62.6	-	-
MOC-G300	5863	10.1	71.6	0.32	1.54
MOC-G750	7453	11.4	79.2	0.43	2.23

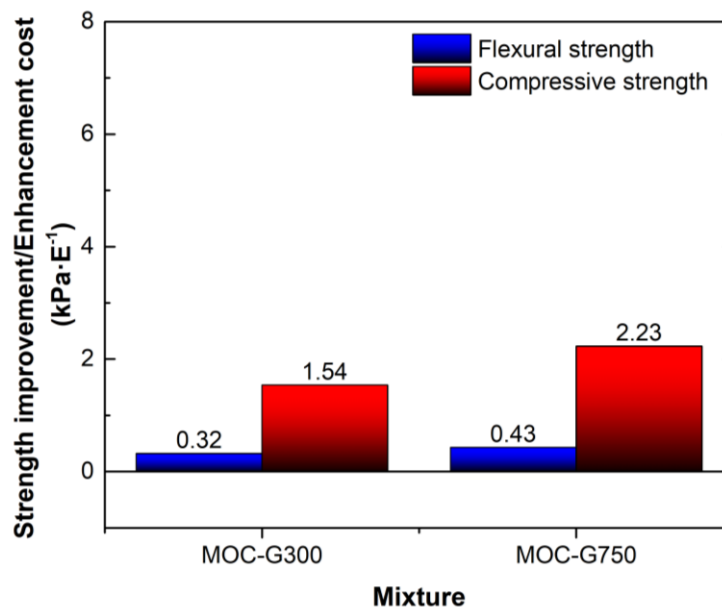


Figure 64: NM's specific surface area: Cost-effectivity ratio.

The cost effectivity of the nano-additive as a ratio of the improvement in mechanical resistance and the price of the NM used is presented in Tab. 34 and Fig. 64. Despite the lower price of the applied GNs C-300 and the total cost per m³, the most cost-effective method is the use of the more expensive C-750 due to the higher performance to improve

both the flexural and compressive strength parameters that affected the final results. The detailed calculation of cost-effectivity is listed in Annex B.

5.1.3 Influence of NM's Volume

This chapter deals with the optimisation of the GN content in MOC-based pastes to achieve the best mechanical, chemical, and physical properties of the formed composite materials.

The phase composition of the prepared hardened mixtures analysed with XRD shows the presence of two phases: unreacted MgO (ICDD 04–003-7162), used as filler, and crystalline Phase 5 (ICDD 00–007-0420), the main product of MOC hardening. However, in the diffractograms, even GNs at 1% dose were not visible., shown in Fig. 65.

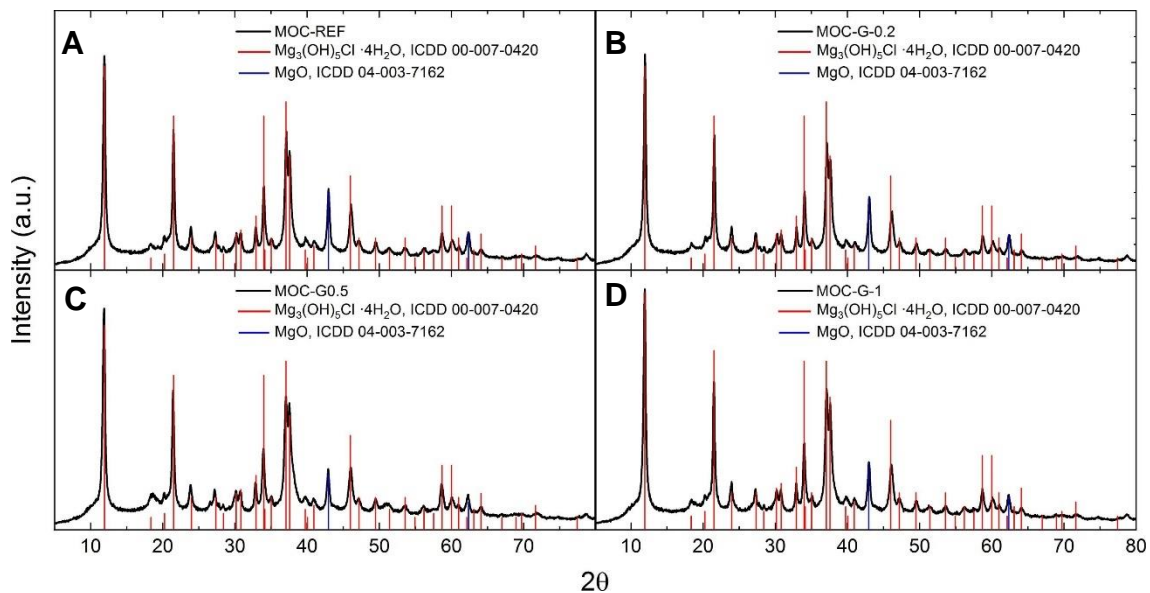


Figure 65: XRD analysis: A) MOC-REF, B) MOC-G0.2, and C) MOC-G0.5 and D) MOC-G1.0.

The micrographs obtained of the composite microstructure, obtained with SEM, are shown in Fig. 66. The GNs were not visible in all enhanced samples. Even when the 1.0 wt% dose of GNs was applied, individual NPs were not visible because of the size and low volume. The only distinguishable were phase 5 needle-like MOC paste crystals.

The EDS elemental maps (Fig. 67) show the presence of Mg, O, and Cl of the MOC paste. The C content is also visible on the elemental map of each mixture, even in MOC-REF- This was caused by reaction with atmospheric carbon dioxide. In the case of enhanced composites, there were signs of carbon clusters due to agglomeration of GNs,

which may affect the final material characteristics. The larger clusters were recorded with a higher dose of NMs.

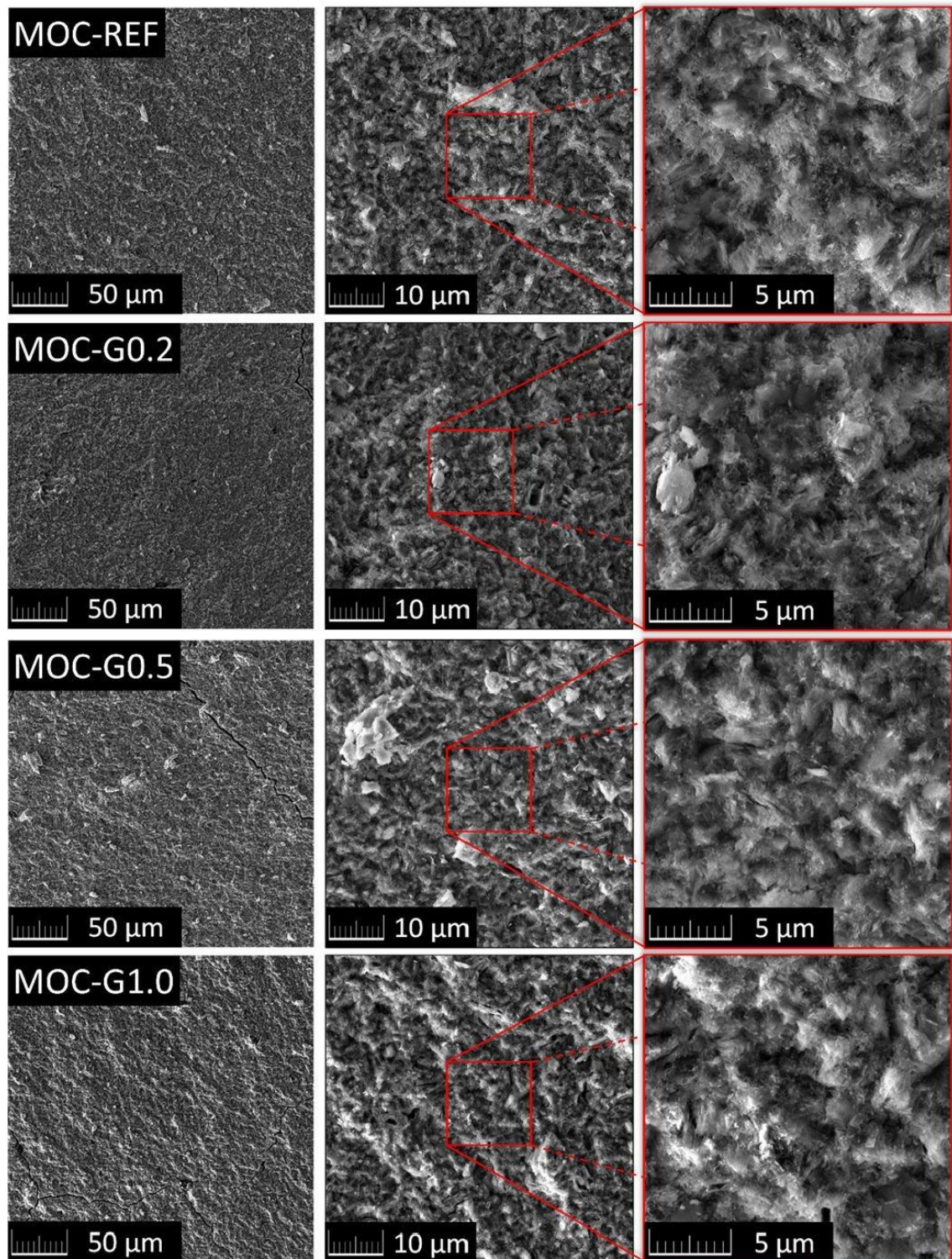


Figure 66: Micrographs of samples: MOC-REF, MOC-G0.2; MOC-G0.5 and MOC-G1.0.

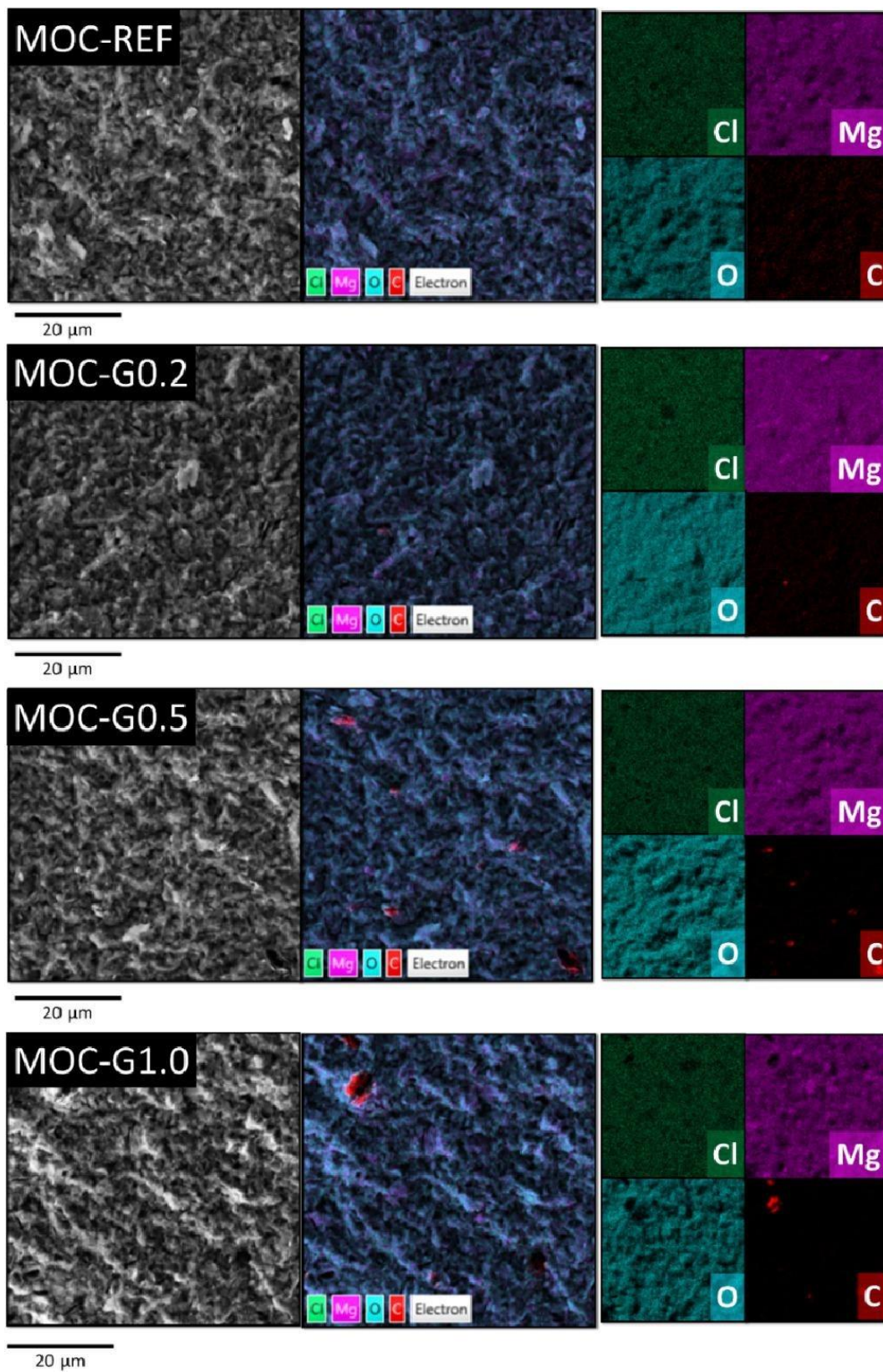


Figure 67: EDS elemental maps of the samples: MOC-REF, MOC-G0.2; MOC-G0.5 and MOC-G1.0.

The MIR spectral lines of the MOC compounds are shown in Fig. 68. There were records of the characteristic fundamental and lattice vibrations of the bonds in $\text{MgCl}_2 \cdot 6\text{H}_2\text{O}$ (O–H, Mg–Cl, and Mg–OH). The vibration bands between wavelengths 3700 and 3300 cm^{-1} were caused by O–H bonds in $\text{Mg}(\text{OH})_2$, H_2O , $\text{MgCl}_2 \cdot 6\text{H}_2\text{O}$. Between the wavelengths of 1647 and 1150 cm^{-1} , the bending and tensile vibrations of the O–H bonds in the hydroxyl group in MOC and the Mg–O bonds in $\text{MgCl}_2 \cdot 8\text{H}_2\text{O}$ were recorded. The presence of GNs was identified by a weak band at 1614 cm^{-1} , which can be attributed to the stretching vibration of the C = C bond.

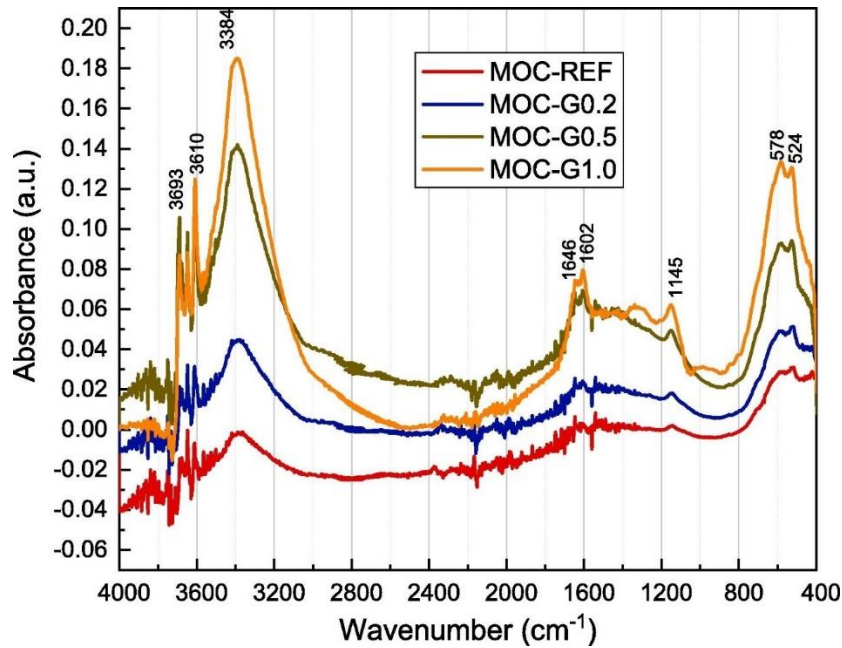


Figure 68: The MIR (Mid-infrared) spectra of MOC-REF, MOC-G0.2; MOC-G0.5 and MOC-G1.0.

The basic structural properties of hardened samples at 28 days, in Tab. 35., shows the relatively low porosity of the control MOC mixture, which decreased further with increasing GNs content. The total open porosity of the composites was reduced by 1.7 %, 2.5 %, and 1.1 % for MOC-G0.2, MOC-G0.5, MOC-G1.0, respectively. This was due to the increase in bulk density, affected by the dose of GNs.

Table 35: NM's volume: Basic structural parameters of pastes.

Mixture	Bulk density	Specific density	Porosity
	ρ_b ($\text{kg} \cdot \text{m}^{-3}$)	ρ_s ($\text{kg} \cdot \text{m}^{-3}$)	ψ (%)
MOC-REF	1772 ± 25	1931 ± 23	8.2 ± 0.2
MOC-G0.2	1784 ± 25	1907 ± 23	6.5 ± 0.1
MOC-G0.5	1787 ± 25	1896 ± 23	5.7 ± 0.1
MOC-G1.0	1806 ± 25	1899 ± 23	4.9 ± 0.1

The results of the MIP analysis are shown in Fig. 69. and Tab. 36. The decrease in porosity and the porosity obtained measured with MIP were consistent with the total open porosity calculated from the bulk and matrix densities. It is apparent that the nano-additive GN significantly reduced the pore volume of capillary pores, as well as micropores with diameter range 3 nm - 7 μm , according to the pore size classification defined by Mindess et al. [152]. Furthermore, with the application of increasing doses of GNs in the composites, there was a significant refinement of the porous structure in terms of lower average pore diameters. Furthermore, the drop in volume of both capillary pores and micropores led to a reduction in the sorption, diffusion, and transport of water vapour. Compared to MOC-REF.

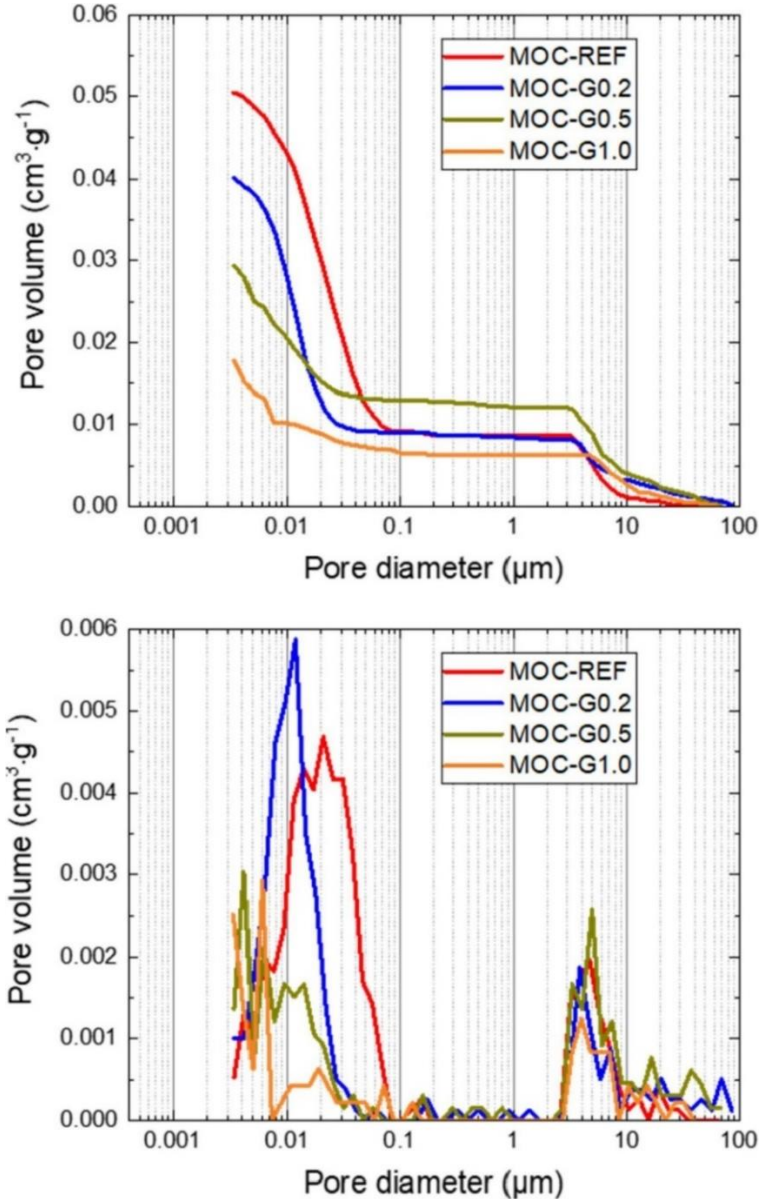


Figure 69: NM's volume: Cumulative (top) and incremental (bottom) pore size distribution curves.

Table 36: NM's volume: Microstructural parameters of hardened composites.

Parameter	MOC-REF	MOC-G0.2	MOC-G0.5	MOC-G1.0
Hg porosity (%)	8.8	7.1	5.5	4.3
Total pore volume (cm ³ ·g ⁻¹)	0.0506	0.0401	0.0296	0.0178
Average pore diameter (μm)	0.0208	0.0118	0.0060	0.0042

The mechanical strength parameters of the hardened composites for 28 days are listed in the Tab. 37. In this case, the increasing dosage of GNs resulted in an increase in both flexural and compressive strength with maximum values obtained, when 1.0 wt% of graphene was applied, which proved the use effectivity of GNs as nano-additive for strengthening the MOC composite paste. In case of flexural strength (Fig. 70), the recorded increase was 44.2 %, 61.5 % and 73.1 % for MOC with 0.2 wt%, 0.5 wt%, and 1.0 wt% dosage. The compressive strength (Fig. 71) increased by 7.6 %, 12.5 % and 26.8 % for MOC-G0.2, MOC-G0.5 and MOC-G1.0, respectively, compared to the control mixture. In addition, the dynamic modulus of elasticity improved by 6.3 %, 10.4 %, and 14.9 %.

Table 37: NM's volume: Mechanical strength of hardened composites.

Mixture	Flexural strength f_f (MPa)	Compressive strength f_c (MPa)	Dynamic modulus of elasticity E (GPa)
MOC-REF	5.2 ± 0.07	78.6 ± 1.1	26.9 ± 0.6
MOC-G0.2	7.5 ± 0.10	84.6 ± 1.2	28.5 ± 0.7
MOC-G0.5	8.4 ± 0.12	88.4 ± 1.2	29.7 ± 0.7
MOC-G1.0	9.0 ± 0.13	99.7 ± 1.4	30.9 ± 0.7

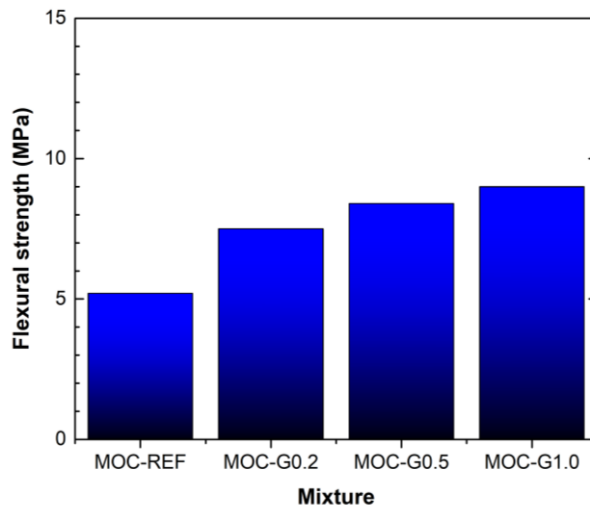


Figure 70: NM's volume: Flexural strength of hardened composites.

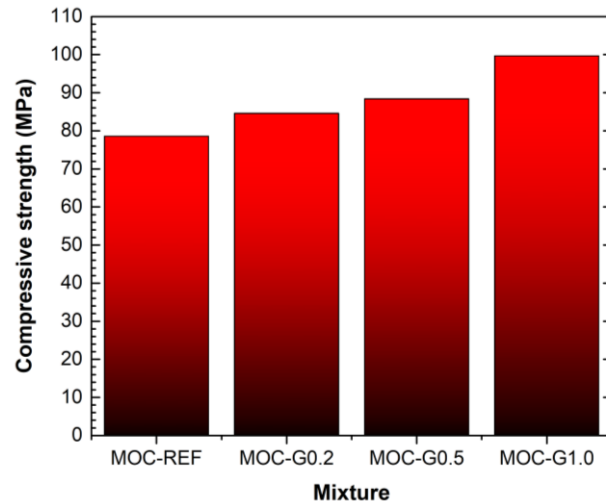


Figure 71: NM's volume: Compressive strength of hardened composites.

The water absorption and thermal properties are listed in the Tab. 38. Hygric performance was affected by the reduction in total porosity of the material due to the addition of GNs, which inhibits the ability to transport moisture.

in addition to the already low absorption of MOC-REF. For comparison with commonly used materials, the water absorption coefficient of ceramic bricks is in a range of 0.1-0.55 $\text{kg}\cdot\text{m}^{-2}\cdot\text{s}^{-1/2}$ [153]. Thus, the graphene-enhanced MOC can be considered to be non-capillary active composites.

Table 38: NM's volume: Hygric and thermal properties of hardened composites.

Mixture	Water absorption coefficient A_w ($\text{kg}\cdot\text{m}^{-2}\cdot\text{s}^{-1/2}$)	24-hour water absorption W_a ($\text{kg}\cdot\text{m}^{-2}$)	Thermal conductivity λ ($\text{W}\cdot\text{m}^{-1}\cdot\text{K}^{-1}$)	Volumetric heat capacity $C_v \times 10^6$ ($\text{J}\cdot\text{m}^{-3}\cdot\text{K}^{-1}$)
MOC-REF	0.039	4.092 ± 0.09	1.040 ± 0.023	2.221 ± 0.058
MOC-G0.2	0.017	3.643 ± 0.08	1.055 ± 0.023	2.335 ± 0.061
MOC-G0.5	0.016	2.661 ± 0.06	1.115 ± 0.025	2.486 ± 0.065
MOC-G1.0	0.008	2.375 ± 0.05	1.180 ± 0.026	2.562 ± 0.067

In case of thermal properties characterised with thermal conductivity and volumetric heat capacity parameters, both increased greatly with the addition of high conductive graphene ($3000\text{-}6500 \text{ W}\cdot\text{m}^{-1}\cdot\text{K}^{-1}$) [154] with the highest specific heat capacity among nanoparticles ($643\text{-}2100 \text{ J}\cdot\text{kg}^{-1}\cdot\text{K}^{-1}$) [155]. Both parameters are affected not only by volume of nano-additive, but also by level of NM dispersion and connection of individual particles.

The cost effectivity of the nano-additive as a ratio of the improvement in mechanical resistance and the price of the NM used is presented in Tab. 39.

The dose of 1% GNs was the highest in terms of additional costs, which was 5 times higher. This resulted in the lowest cost-effectivity compared to the flexural strength and the second highest compared to the compressive strength. However, the composite reached the compressive strength of nearly 100 MPa, which was the highest among the measured mixtures.

Table 39: NM's volume: Cost-effectivity of additive.

Mixture	Additional cost per m ³ (€)	Flexural strength f_f (MPa)	Compressive strength f_c (MPa)	Cost-effectivity in comparison of:	
				f_f (kPa·€ ⁻¹)	f_c (kPa·€ ⁻¹)
MOC-REF	-	5.20	78.60	-	-
MOC-G0.2	2962	7.50	84.60	0.78	2.03
MOC-G0.5	7410	8.40	88.40	0.43	1.32
MOC-G1.0	14821	9.00	99.70	0.26	1.42

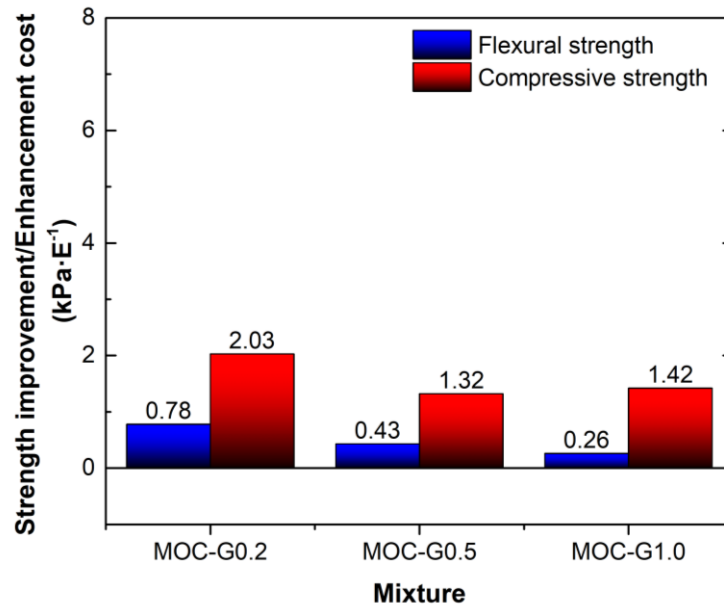


Figure 72: NM's volume: Cost-effectivity ratio.

The best strength enhancement to the additional cost ratio, in terms of both flexural and compressive strength, reached MOC-G0.2 with only 0.2 by weight of NMs and the lowest nano-additive cost. The trend of cost-effectivity ratio is shown in Fig. 72. The detailed calculation of cost-effectivity is listed in Annex B.

5.1.4 Combination of 1D and 2D Nano-additives

In this part, the material characteristics of MOC were obtained with a combination of 1D and 2D NMs, specifically GNs and MWCNTs in both a non-functionalised and a functionalised form.

The chemical composition of composites with non-functionalised and functionalised NMs measured by SEM/EDS is shown in Figs. 73 and 74. The elemental composition shows the presence of Mg, Cl, and O corresponding to the composition of MOC phase 5 crystals and residual MgO which served as filler. The C content is observed again in all mixtures, even the control mixture, as a result of carbonation products on the surface of the samples. The elemental maps of MOC-GO-OMWCNT-0.1 and MOC-GO-OMWCNT-0.2, presented in Fig. 75, show the formation of carbon agglomerates.

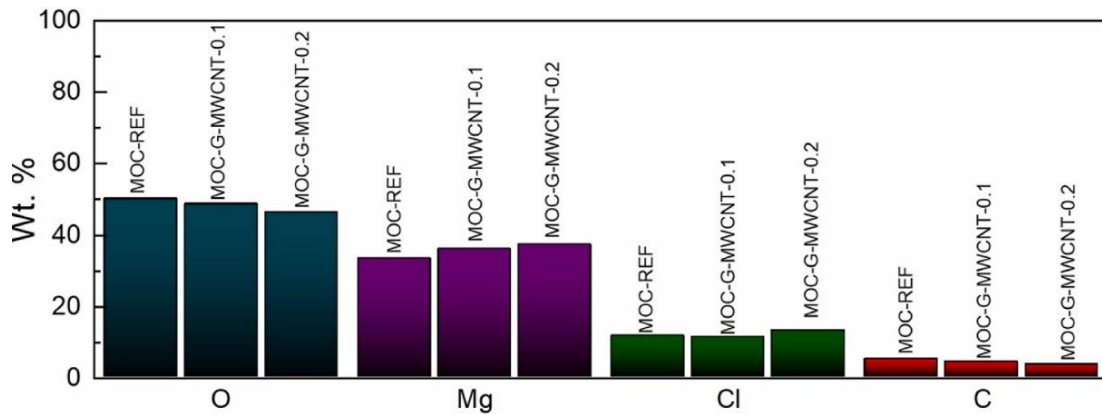


Figure 73: The elemental composition: MOC co-doped with non-functionalized NMs:

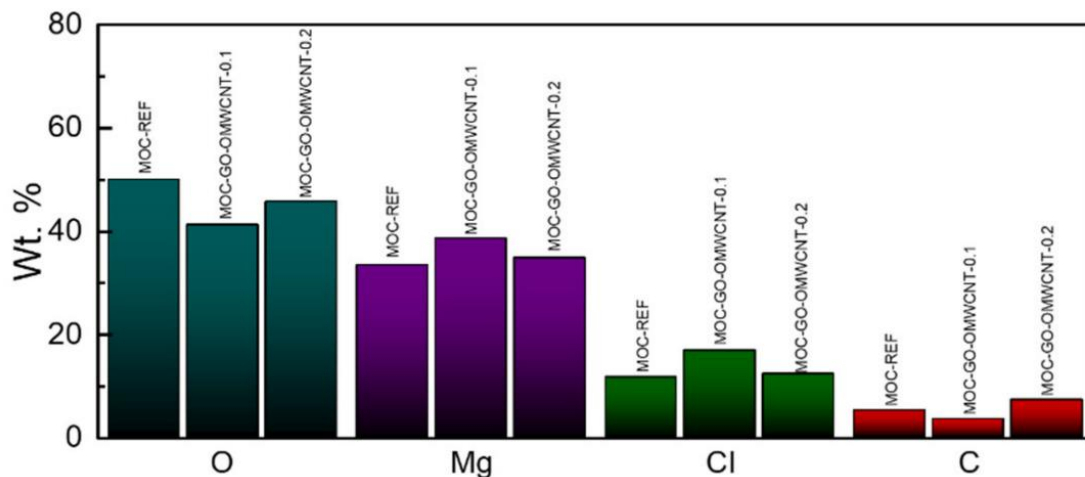


Figure 74: The elemental composition: MOC co-doped with functionalized NMs:

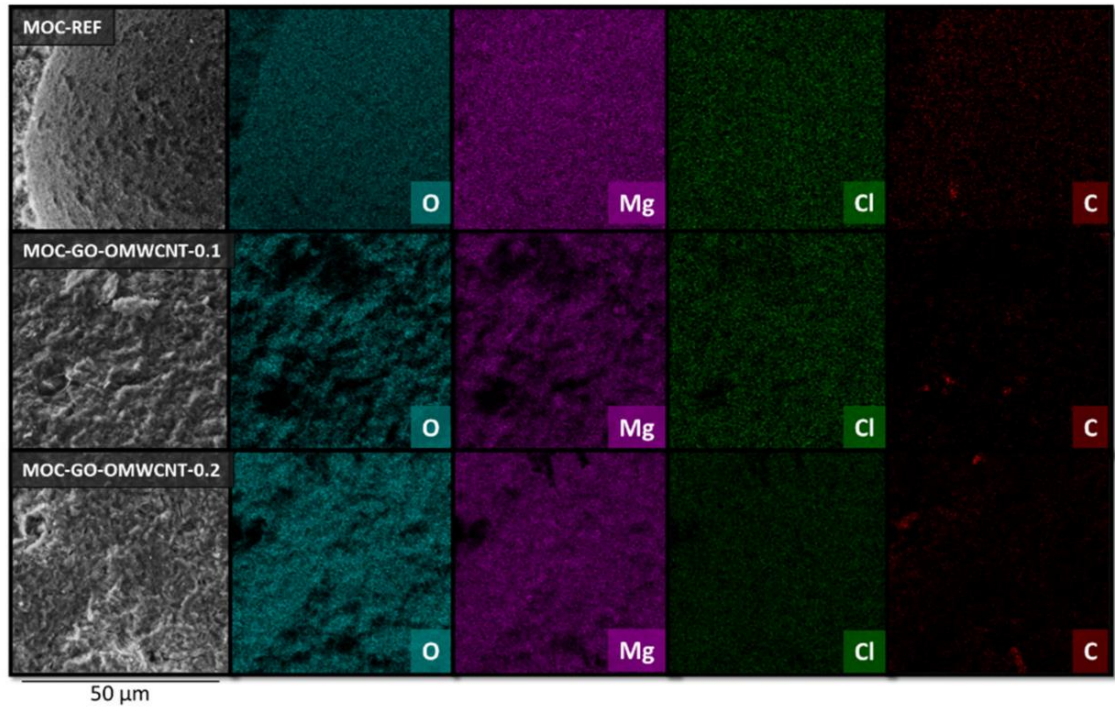


Figure 75: The elemental maps of MOC surface modified with functionalized NMs.

The results of XRD analysis and SEM micrographs are not presented in this part of the thesis. The resulting diffraction patterns were similar for all mixtures, with both normal and oxidised NMs, and were consistent with previous studies, with no traces of carbon-based NMs due to their very low content.

The results of the macrostructural characteristics of the composites are shown in Tab. 40. In this instance, the control MOC obtained very low open porosity, which was further decreased with nano-additive dosage by 1.1 % (absolute value), when 0.2 wt% of co-doped NMs were applied. Quantitatively, the resulting porosity values were low; therefore, their high mechanical strength performance can be assumed.

Table 40: Co-doped MOC: Basic structural properties of pastes.

Mixture	Bulk density	Specific density	Porosity
	ρ_b ($\text{kg}\cdot\text{m}^{-3}$)	ρ_s ($\text{kg}\cdot\text{m}^{-3}$)	ψ (%)
MOC-REF	1768 ± 25	1838 ± 22	3.8 ± 0.1
MOC-G-MWCNT-0.1	1786 ± 25	1841 ± 22	3.0 ± 0.1
MOC-G-MWCNT-0.2	1807 ± 25	1858 ± 22	2.7 ± 0.1
MOC-GO-OMWCNT-0.1	1801 ± 25	1861 ± 22	3.2 ± 0.1
MOC-GO-OMWCNT-0.2	1812 ± 25	1862 ± 23	2.7 ± 0.1

Mechanical strength and stiffness characteristics are listed in the Tab. 41. Co-doping of MOC with 1D and 2D NMs had a positive effect in all cases, especially when non-functionalized NMs were applied. The flexural strength increased by 34.2 % and 42.1 % for MOC-G-MWCNT0.1 and MOC-G-MWCNT-0.2, respectively. In the case of compressive strength, the increase was 17.4 % and 24.2 % for these mixtures.

Table 41: Co-doped MOC: Mechanical strength parameters.

Mixture	Flexural strength f_f (MPa)	Compressive strength f_c (MPa)	Dynamic modulus of elasticity E (GPa)
MOC-REF	3.8 ± 0.05	59.1 ± 0.9	24.3 ± 0.6
MOC-G-MWCNT-0.1	5.1 ± 0.07	69.4 ± 1.0	25.1 ± 0.6
MOC-G-MWCNT-0.2	5.4 ± 0.07	74.6 ± 1.1	25.4 ± 0.6
MOC-GO-OMWCNT-0.1	5.9 ± 0.08	60.1 ± 0.8	25.4 ± 0.6
MOC-GO-OMWCNT-0.2	7.3 ± 0.10	63.2 ± 0.9	25.9 ± 0.6

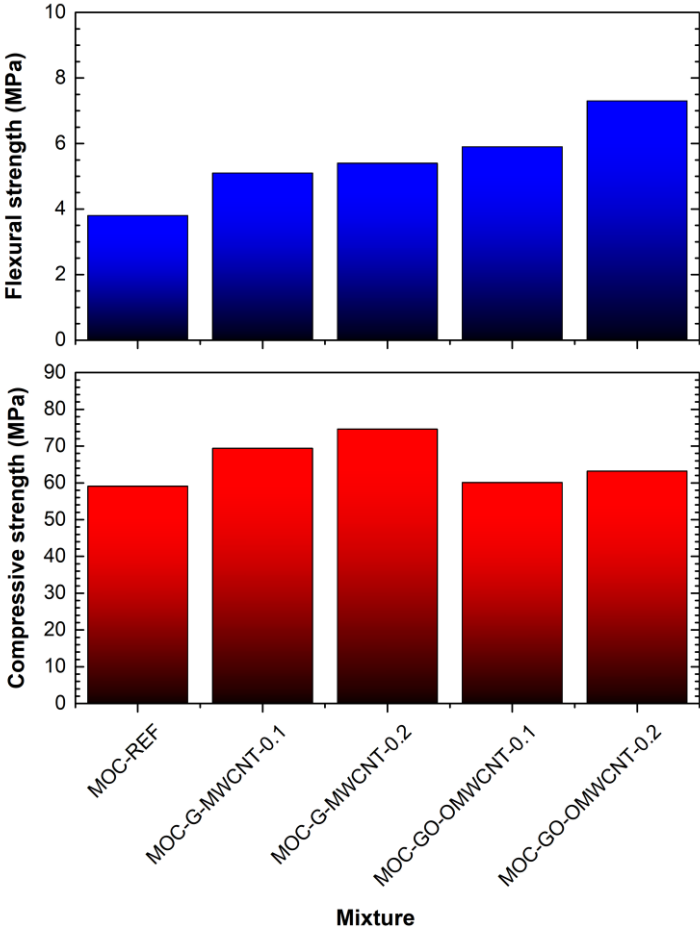


Figure 76: Co-doped MOC: Mechanical strength of hardened composites.

Compressive strength of MOC-G-MWCNT-0.2 among the measured mixtures. On the other hand, MOC co-doped with functionalised NMs had a more positive effect on flexural strength. The application of 0.2 wt% of NMs resulted in almost double the flexural strength compared to the MOC-REF. However, while the compressive strength also increased, the gain was not as high as for nonfunctionalised NMs. The rate of increase of individual strength parameters is shown in Fig. 76.

The water transport parameters are listed in Tab.42. The addition of NMs reduced porosity, followed by a decrease in capillary absorption of enhanced mixtures. The decrease is greater when functionalised NMs are applied in comparison to those that are not functionalised. It should be noted that the absorption properties of the original unimproved material are low compared to other commonly used building materials.

Table 42: Co-doped MOC: Hygric properties of hardened composites.

Mixture	Water absorption coefficient A_w ($\text{kg}\cdot\text{m}^{-2}\cdot\text{s}^{-1/2}$)	24-hour water absorption W_a ($\text{kg}\cdot\text{m}^{-2}$)
MOC-REF	$0.0029 \pm 7 \times 10^{-5}$	1.07 ± 0.01
MOC-G-MWCNT-0.1	$0.0022 \pm 5 \times 10^{-5}$	0.93 ± 0.01
MOC-G-MWCNT-0,2	$0.0014 \pm 5 \times 10^{-5}$	0.51 ± 0.01
MOC-GO-OMWCNT-0.1	$0.0019 \pm 4 \times 10^{-5}$	0.80 ± 0.01
MOC-GO-OMWCNT-0.2	$0.0018 \pm 4 \times 10^{-5}$	0.65 ± 0.01

Similarly, as in previous chapters, the mixtures follow the trend of increased thermal conductivity and heat capacity, with the higher the volume of applied NMs due to the drop of porosity and high conductivity and heat storage properties of all NMs. However, it is impossible to distinguish which effect was the dominant in improving the thermal parameters analysed. The resulting heat transport characteristics are listed in Tab. 43.

Table 43: Co-doped MOC: Thermal properties of hardened composites.

Mixture	Thermal conductivity λ ($\text{W}\cdot\text{m}^{-1}\cdot\text{K}^{-1}$)	Volumetric heat capacity $C_v \times 10^6$ ($\text{J}\cdot\text{m}^{-3}\cdot\text{K}^{-1}$)
MOC-REF	1.276 ± 0.029	2.588 ± 0.067
MOC-G-MWCNT-0.1	1.331 ± 0.306	2.752 ± 0.072
MOC-G-MWCNT-0,2	1.347 ± 0.031	2.767 ± 0.072
MOC-GO-OMWCNT-0.1	1.322 ± 0.030	2.675 ± 0.070
MOC-GO-OMWCNT-0.2	1.334 ± 0.031	2.815 ± 0.073

Table 44: Co-doped MOC: Cost-effectivity of additive.

Mixture	Additional cost per m ³ (€)	Flexural strength <i>f_f</i> (MPa)	Compressive strength <i>f_c</i> (MPa)	Cost-effectivity in comparison of:	
				<i>f_f</i>	<i>f_c</i>
				(kPa·€ ⁻¹)	(kPa·€ ⁻¹)
MOC-REF	-	3.80	59.10	-	-
MOC-G-MWCNT-0.1	1684	5.10	69.40	0.77	6.12
MOC-G-MWCNT-0.2	3274	5.40	74.60	0.49	4.73
MOC-G-MWCNT-0.1	12991	5.90	60.10	0.16	0.08
MOC-G-MWCNT-0.2	25259	7.30	63.20	0.14	0.16

As we can see from the results of the cost-effectivity ratio in Tab. 44 and Fig. 77, the MOC with both volumes of functionalized NMs reached a very low value due to the several times higher cost of the used graphene and MWCNTs compared to the non-functionalized ones. In case of normal NMs, the cost-effectivity of flexural strength was similar to the previous sections. On the other hand, the cost-effectivity with regard to compressive strength came out to be high. The most efficient batch of particle size appears to be 0.1 wt%, which achieved a strength of less than 70 MPa. The detailed calculation of cost-effectivity is listed in Annex B.

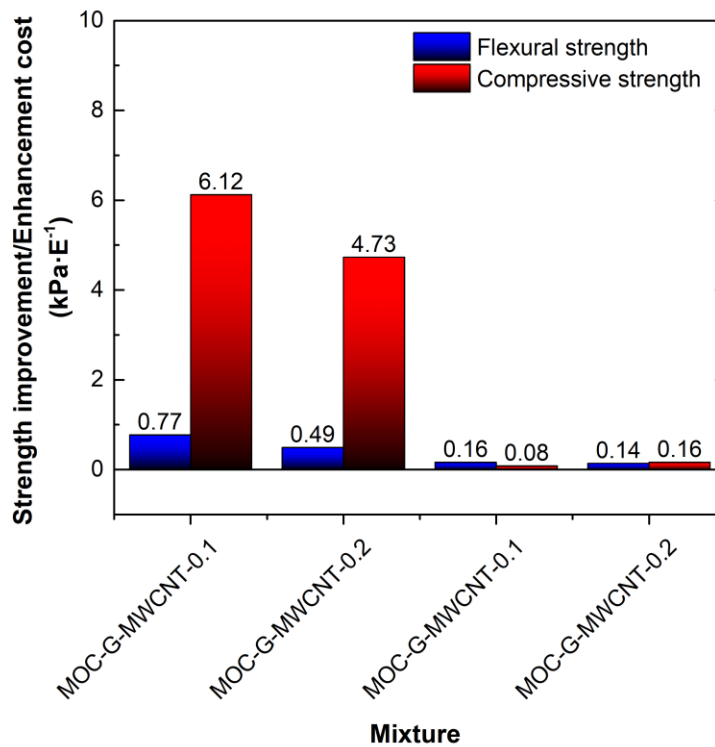


Figure 77: Co-doped MOC: Cost-effectivity ratio.

5.1.5 Carbon Spheres Nano-additive

This part is focused on nano-enhancement of MOC composite, in this instance in form of mortars with silica sand aggregate with size up to 2 mm and waste carbon spheres (CSs) as nano-additive.

The CSs used were examined using SEM/EDS analysis (Fig. 78). The observed particles were spherical or quasi-spherical in shape and up to approximately 0.4 μm in diameter. Elemental map analysis showed that the sample particles contain 92.5 wt% carbon, 3.2 wt% oxygen, 3.6 wt% iron, and 0.6 wt% silicon.

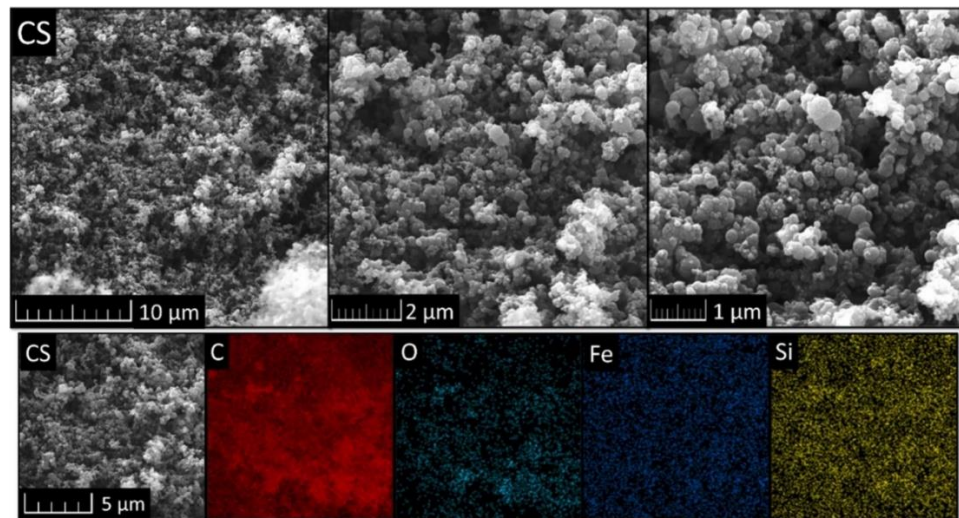


Figure 78: SEM/EDS analysis of Carbon Spheres (CSs).

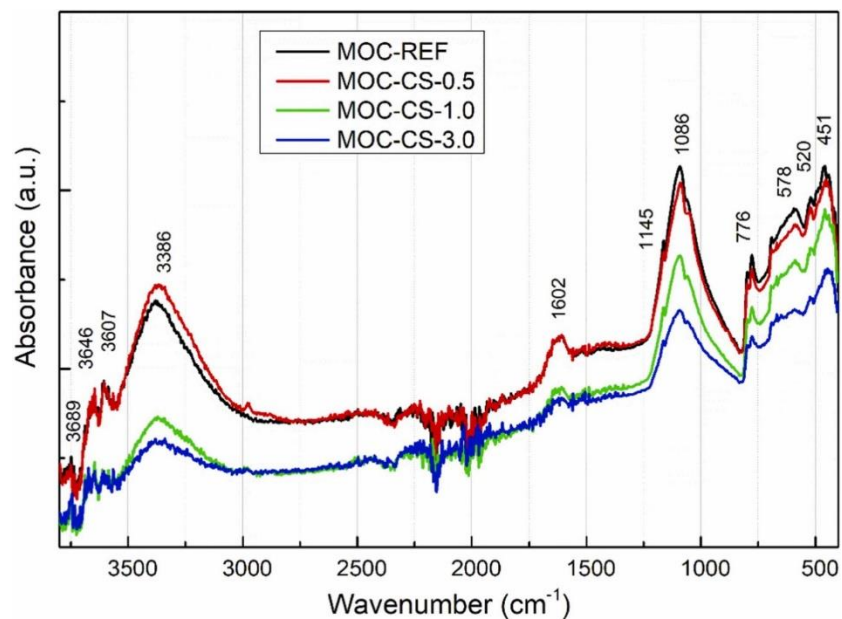


Figure 79: The MIR (Mid-infrared) spectra of MOC-CS pastes.

Fig. 79 presents IR spectral lines of MOC mortar. The bands of Mg-O, Mg-Cl, and O-H are clearly visible in the spectra. The development of MOC hydration was carried out by monitoring the amount of magnesium hydroxide investigated. The most typical absorption band of magnesium hydroxide occurs at 3689 cm^{-1} ; therefore, a peak resolution and semiquantitative analysis was used to compare the $\text{Mg}(\text{OH})_2$ content in the MOC sample composites tested. As can be seen, the more CS was applied, the less $\text{Mg}(\text{OH})_2$ formed during hydration. In the case of the composite mixture with 3.0 by weight CS, no $\text{Mg}(\text{OH})_2$ content was found, which had a positive effect on the mechanical strength and overall durability of the cured composite.

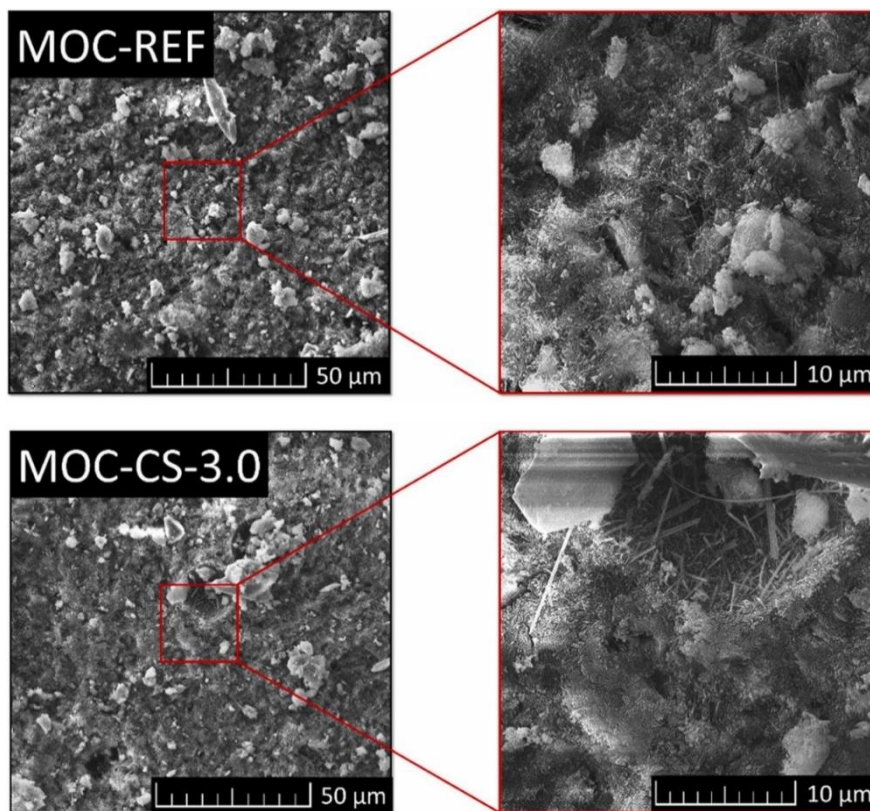


Figure 80: SEM micrograph of MOC-REF and MOC-CS-3.0

The fracture surface morphology of the hardened samples was analysed using SEM (Fig. 80) showing no visible cracks or defects and a typical crystalline phase of the MOC. Even in this case, the carbon nanomaterials were not visible on the surface, even at a dose as high as 3.0 by weight.

In previous chapters, the addition of carbon-based NMs had no apparent effect on the crystalline phase of MOC. However, based on the obtained FT-IR data, the presence of CS in the composites affected the $\text{Mg}(\text{OH})_2$ content. This leads to the hypothesis that the applied CSs reacts with $\text{Mg}(\text{OH})_2$ to form an amorphous Mg-C-H-like substance.

There is an expectation that there is chemisorption of dissolved Mg ions on the active surface of the CS.

The results of basic structural properties are listed in the Tab. 45. The addition of CSs had only a small effect on both the bulk and specific densities. However, the differences are in the range of expanded combined uncertainties. Additionally, the porosity changes were minimal compared to the control mortar and consistent with the observed values of the total pore volume and the average pore size obtained by MIP analysis and listed in the tab. 46.

Table 45: Carbon spheres additive: Basic structural properties of composites.

Mixture	Bulk density	Specific density	Porosity
	ρ_b ($\text{kg}\cdot\text{m}^{-3}$)	ρ_s ($\text{kg}\cdot\text{m}^{-3}$)	ψ (%)
MOC-REF	2052 \pm 29	2270 \pm 27	9.6 \pm 0.2
MOC-CS-0.5	2054 \pm 29	2263 \pm 27	9.2 \pm 0.2
MOC-CS-1.0	2053 \pm 29	2270 \pm 27	9.6 \pm 0.2
MOC-CS-3.0	2051 \pm 29	2280 \pm 27	10.0 \pm 0.2

Table 46: Carbon spheres additive: Microstructural parameters of hardened composites.

Parameter	MOC-REF	MOC-CS-0.5	MOC-CS-1.0	MOC-CS-3.0
Total pore volume ($\text{cm}^3\cdot\text{g}^{-1}$)	0.0582	0.0565	0.0551	0.0574
Average pore diameter (μm)	0.0445	0.0455	0.0470	0.0474

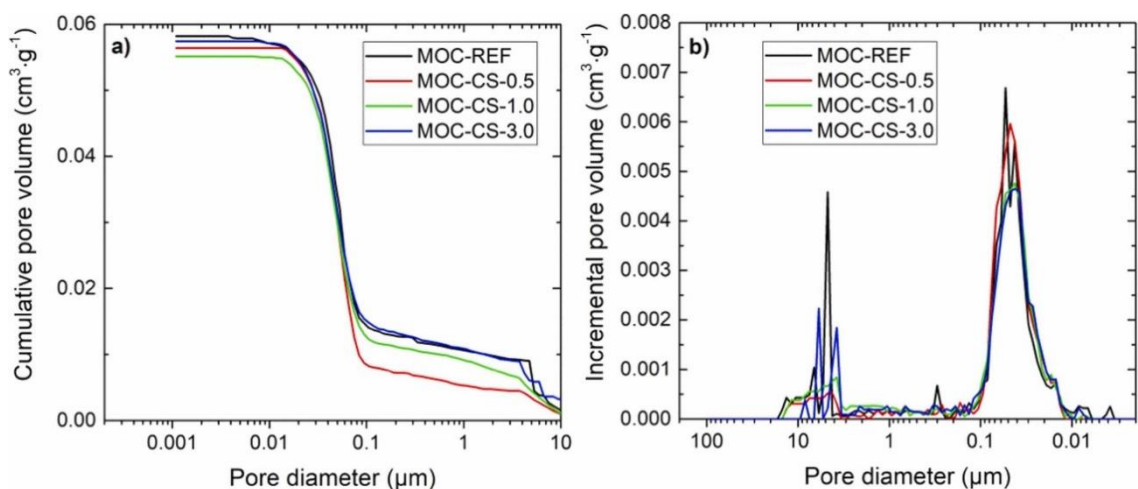


Figure 81: Carbon spheres additive: a) Cumulative and b) incremental pore size distribution curves.

A more detailed description of the pore structure of the investigated materials is shown in Fig. 81. In all cases, the maximum pore volume was observed in the range 0.01 μm to 0.1 μm . This pore size corresponds to large and medium capillary pores, which affect the mechanical strength and permeability of mortars. Larger voids, recorded in Fig. 81b, were observed mainly in composites with higher CSs content and are caused by CSs agglomeration, i.e. insufficient homogenisation of applied NMs.

The measured flexural strength, compressive strength, and dynamic modulus of elasticity values are shown in Tab.47. There is almost no change in all parameters when 0.5 wt% of CSs was applied. It has been demonstrated that such a low dose of CSs in combination with mechanical homogenisation is not sufficient to improve overall mechanical properties. However, in the case of MOC-CS-1.0 and MOC-CS-3.0, increase in both flexural and compressive strength was observed compared to MOC-REF (Fig. 82). Quantitatively, MOC-CS3.0 had the highest mechanical strength, but only approximately 4.3 % for the flexural strength and 5.5 % for the compressive strength. However, MOC- CS-1.0 shows slightly lower performance at a dose three times lower.

Table 47: Carbon spheres additive: Mechanical strength characteristics.

Mixture	Flexural strength f_r (MPa)	Compressive strength f_c (MPa)	Dynamic modulus of elasticity E (GPa)
MOC-REF	16.7 \pm 0.23	76.2 \pm 1.06	36.0 \pm 0.8
MOC-CS-0.5	16.6 \pm 0.23	76.5 \pm 1.06	36.1 \pm 0.8
MOC-CS-1.0	17.5 \pm 0.25	79.8 \pm 1.12	36.3 \pm 0.8
MOC-CS-3.0	17.7 \pm 0.25	80.5 \pm 1.12	36.1 \pm 0.8

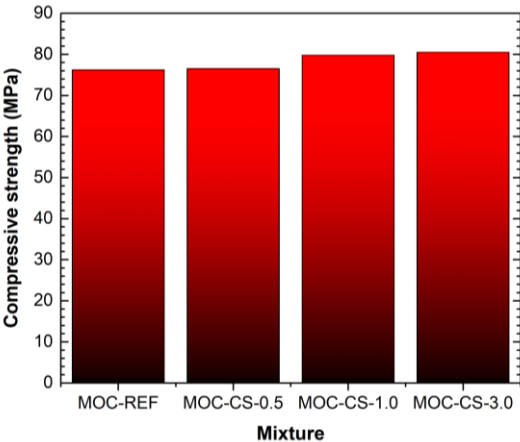


Figure 82: Carbon spheres additive: Compressive strength of hardened mortars.

The hygric properties, described by the water absorption coefficient and the 24-hour water absorption, are shown in the Tab. 48. The results show a decrease in water transport with the application of CSs. This was mainly caused by the decrease in porosity, which is in accordance with the observed porosity despite the higher volume of CSs.

Table 48: Carbon spheres additive: Hygric properties of hardened composites.

Mixture	Water absorption coefficient A_w ($\text{kg}\cdot\text{m}^{-2}\cdot\text{s}^{-1/2}$)	24-hour water absorption W_a ($\text{kg}\cdot\text{m}^{-2}$)
MOC-REF	$0.0042 \pm 5 \times 10^{-5}$	2.51 ± 0.01
MOC-CS-0.5	$0.0026 \pm 3 \times 10^{-5}$	2.37 ± 0.01
MOC-CS-1.0	$0.0030 \pm 4 \times 10^{-5}$	2.46 ± 0.01
MOC-CS-3.0	$0.0031 \pm 4 \times 10^{-5}$	2.40 ± 0.01

The cost-effectivity results are shown in the Tab. 49. And Fig. 83. indicate 0.5 wt% of CSs as the most inappropriate dosage volume. The negative flexural strength ratio is caused by its lower value compared to the control mixture. As the best volume in terms of cost of NM and material enhancement was the use of 1.0 wt% of CSs, compared to the MOC-CS-3.0. This was due to the higher additional cost for the latter. Furthermore, MOC-CS-1.0 reached nearly identical flexural and compressive strength. Thus, this is the most effective CSs volume.

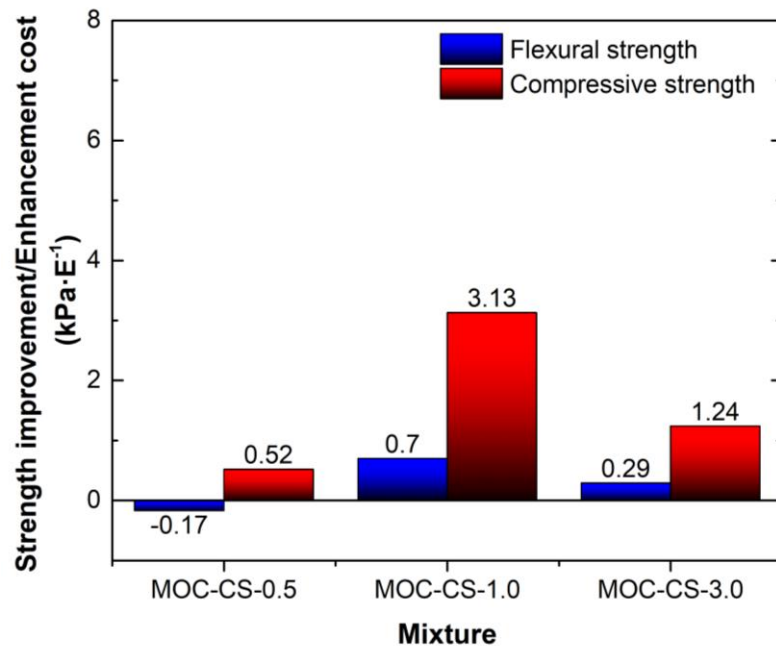


Figure 83: Carbon spheres additive: Cost-effectivity ratio.

It must be noted that the calculations and cost values were based on the assumption that the material was sold at the same price as industrial grade MWCNTs. The actual cost value of this type of NM has not been determined because it was obtained as waste material from the production of syngas. The detailed calculation of cost-effectivity is listed in Annex B.

Table 49: Carbon spheres additive: Cost-effectivity of the additive.

Mixture	Additional cost per m³ (€)	Flexural strength <i>f_f</i> (MPa)	Compressive strength <i>f_c</i> (MPa)	Cost-effectivity in comparison of:	
				<i>f_f</i> (kPa·€⁻¹)	<i>f_c</i> (kPa·€⁻¹)
MOC-REF	-	16.70	76.20	-	-
MOC-CS-0.5	575	16.60	76.50	-0.17	0.52
MOC-CS-1.0	1150	17.50	79.80	0.70	3.13
MOC-CS-3.0	3460	17.70	80.50	0.29	1.24

5.2 Standardized Mortars

The following section deals with the characterization of 28-days cured mortars based on magnesium oxychloride cement (MOC), lime hydrate (CL) and natural hydraulic lime (HL) modified with GNs, MWCNTs and CSs at 0.1 wt%, 0.3 wt% and 0.5 wt%. The results are focused on the basic properties, mechanical strength, heat transfer properties, and cost-effectivity of the mixtures. All measured characteristics and detailed calculations are listed in Annex C, D and E for MOC, CL and HL composites, respectively.

5.2.1 Magnesium Oxychloride Cement Mortars (MOC)

The elemental composition shows the presence of Mg, Cl, and O corresponding to the phase composition of the MOC phase crystals, as shown in MOC-REF in Fig. 84. Because the MOC mortar is composed of industrial light-burnt MgO, the mortar contains traces of Fe and Al, but the concentration is very low and the instrument did not detect these elements. The C content is again observed in all enhanced mixtures across the entire cross-section because of material carbonation and NM modification.

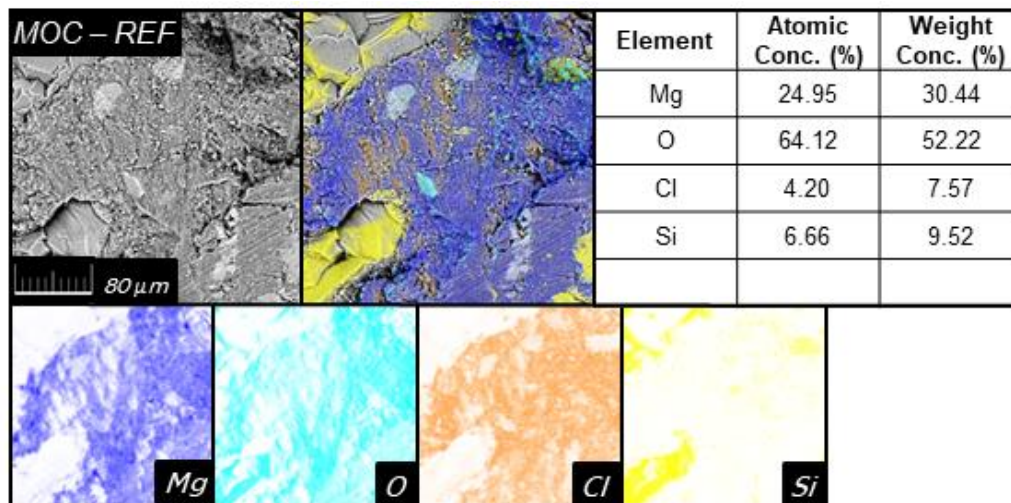


Figure 84: Elemental maps of the MOC-REF mixture.

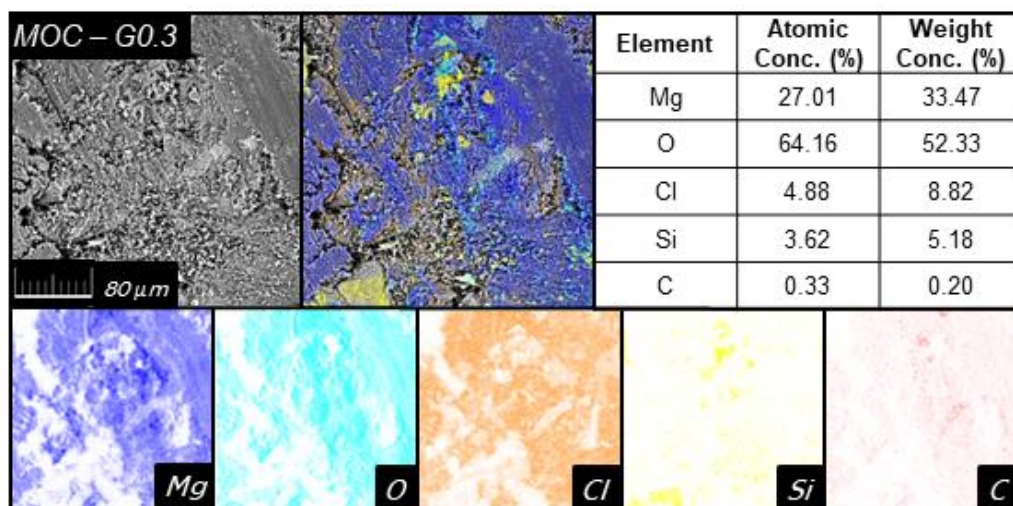


Figure 85: Elemental maps of the MOC-G0.3 mixture.

The instances are shown in Fig. 85 and Fig. 86 for MOC-G0.3 and MOC-S0.3, respectively. While the MOC-G0.3 sample shows carbonaceous clusters, MOC-S0.3 has visibly fewer clusters, confirming the effectivity of the dispersion technique using the ultrasonic bath and tannic acid additive.

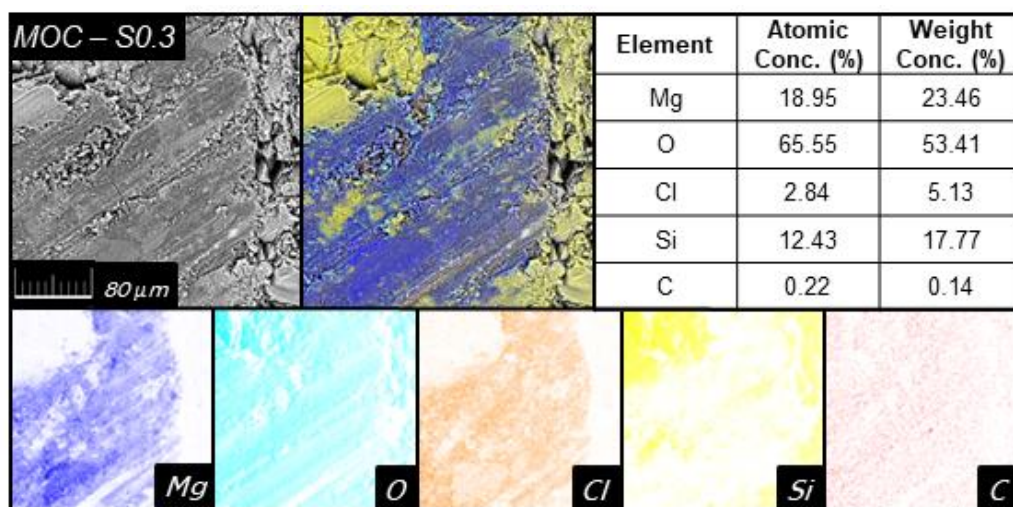


Figure 86: Elemental maps of the MOC-S0.3 mixture.

The basic properties of the MOC composites can be seen in the Tab. 50. While the specific density was in all cases nearly similar to the density of the control sample, the changes occurred in cases of bulk density and porosity. The application of GNs increases the porosity by around 1 % (absolute value) for MOC-G0.1 and MOC-G0.3.

The MOC-G0.5 obtained nearly identical porosity as MOC-REF. In case of MWCNT-enhanced mixtures, surfactant and antifoamer, the porosity increased by more than 4 % (absolute value) when a dose of 0.1% and 0.3% dosage was used. 0.5% dosage increases porosity by 1.8 %. The influence of CSs dispersed in tannic acid was less

effective than that obtained from the aforementioned enhancements. The highest increase in porosity was in the case of MOC-S0.3 (by 1.3% higher).

Table 50: MOC mixtures: Basic structural properties.

Mixture	Bulk density	Specific density	Porosity
	ρ_b ($\text{kg}\cdot\text{m}^{-3}$)	ρ_s ($\text{kg}\cdot\text{m}^{-3}$)	ψ (%)
MOC-REF	2206 ± 31	2352 ± 28	6.2 ± 0.1
MOC-G0.1	2179 ± 31	2342 ± 28	7.0 ± 0.1
MOC-G0.3	2191 ± 31	2372 ± 28	7.6 ± 0.2
MOC-G0.5	2201 ± 31	2344 ± 28	6.1 ± 0.1
MOC-CNT0.1	2116 ± 30	2356 ± 28	10.2 ± 0.2
MOC-CNT0.3	2123 ± 30	2377 ± 29	10.7 ± 0.2
MOC-CNT0.5	2131 ± 30	2315 ± 28	8.0 ± 0.2
MOC-S0.1	2205 ± 31	2365 ± 28	6.8 ± 0.1
MOC-S0.3	2186 ± 31	2362 ± 28	7.5 ± 0.1
MOC-S0.5	2207 ± 31	2349 ± 28	6.1 ± 0.1

The mechanical strength characteristics of MOC mortars are presented in Tab.51. In terms of mechanical strength and stiffness, MOC mortar prepared from industrial lightly fired MgO was highly effective, similar to its high purity MgO alternative described in previous chapters.

Table 51: MOC mixtures: Mechanical strength characteristics.

Mixture	Flexural strength	Compressive strength	Dynamic modulus of elasticity
	f_f (MPa)	f_c (MPa)	E (GPa)
MOC-REF	22.32 ± 0.31	68.20 ± 0.10	48.53 ± 1.12
MOC-G0.1	24.93 ± 0.35	73.86 ± 1.03	49.33 ± 0.69
MOC-G0.3	26.24 ± 0.37	75.24 ± 1.05	48.22 ± 0.68
MOC-G0.5	25.15 ± 0.36	65.10 ± 0.91	49.03 ± 0.69
MOC-CNT0.1	24.31 ± 0.34	71.78 ± 1.00	44.50 ± 0.62
MOC-CNT0.3	23.12 ± 0.32	72.73 ± 1.03	44.20 ± 0.62
MOC-CNT0.5	21.36 ± 0.30	69.41 ± 0.97	44.99 ± 0.63
MOC-S0.1	31.20 ± 0.43	81.29 ± 1.14	48.54 ± 1.12
MOC-S0.3	33.23 ± 0.47	82.95 ± 1.16	48.09 ± 1.11
MOC-S0.5	33.25 ± 0.47	69.85 ± 0.98	48.99 ± 1.13

The dynamic modulus of elasticity of modified mixtures resulted in the same with the exception of MOC-CNT mixtures with higher porosity, which reached lower modulus of elasticity values by approx. 9 %.

In terms of flexural strength (Fig. 87), MWCNTs enhancement was least effective. The highest increase was obtained when 0.1% dosage was applied (9% increase). A further increase of the applied NM volume decreases the strength. In case of GNs enhanced mortar, the best result reached MOC-G0.3. A similar trend can be observed for the compressive strength (Fig. 88) of these samples. The best result among MOC-G and MOC-CNT achieves MOC-G0.3 with 10.3 increase to more than 75 MPa.

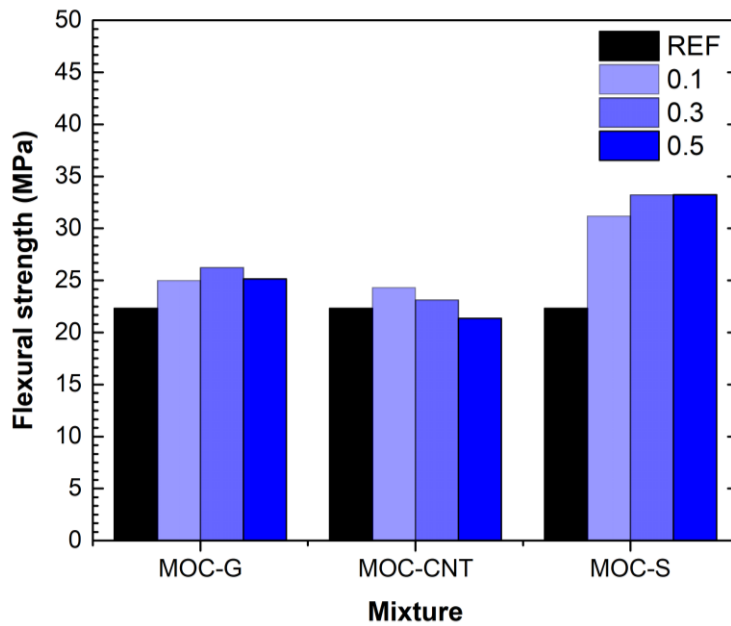


Figure 87: MOC mixtures: Flexural strength parameters.

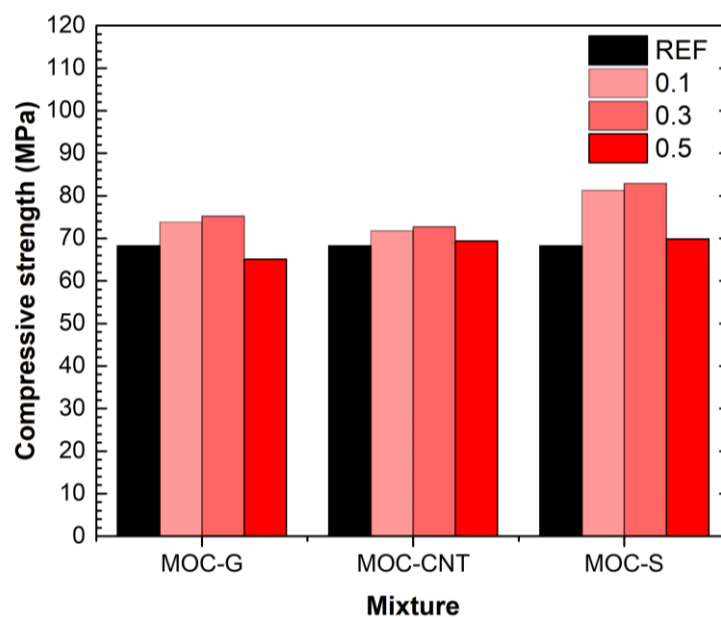


Figure 88: MOC mixtures: Compressive strength parameters.

However, the CSs enhancement greatly improved the extraordinary properties of the MOC composite. The increase in flexural strength was 39.7 % for MOC-S0.1. Both the MOC-S0.3 and MOC-S0.5 strengths increased further by 48.9 % for each mixture. In case of compressive strength, the results present the highest mechanical strength among studied mortars, 81.29 MPa and 82.95 MPa. It was 19.2% and 21.6% increases of MOC-S0.1 and MOC-S0.3.

The heat transfer properties, shown in Tab. 52, were consistent with the results of the total porosity of the MOC mortars. MOC mortar obtained high conductive properties even without any modification. The addition of NMs again increased both the thermal conductivity and the heat capacity. The highest thermal conductivity and heat capacity was obtained by HL-S0.5. The increase was only 3.5 % and 5. % in thermal conductivity and heat capacity, respectively.

Table 52: MOC mixtures: Heat transfer characteristics.

Mixture	Thermal conductivity λ ($\text{W}\cdot\text{m}^{-1}\cdot\text{K}^{-1}$)	Volumetric heat capacity $C_v \times 10^6$ ($\text{J}\cdot\text{m}^{-3}\cdot\text{K}^{-1}$)
MOC-REF	3.262 ± 0.072	2.153 ± 0.056
MOC-G0.1	3.245 ± 0.071	2.090 ± 0.054
MOC-G0.3	3.285 ± 0.072	2.167 ± 0.056
MOC-G0.5	3.364 ± 0.074	2.214 ± 0.058
MOC-CNT0.1	3.201 ± 0.080	2.012 ± 0.052
MOC-CNT0.3	3.174 ± 0.070	2.094 ± 0.054
MOC-CNT0.5	3.249 ± 0.071	2.161 ± 0.056
MOC-S0.1	3.279 ± 0.072	2.082 ± 0.054
MOC-S0.3	3.310 ± 0.073	2.116 ± 0.055
MOC-S0.5	3.376 ± 0.074	2.268 ± 0.058

The cost-effectivity of MOC mortars is presented in the Tab. 53. and Fig. 89. The results show, if the dosage of individual nano-additives is compared, that the most cost-effective dose was always 0.1% dose. MOC-G0.1 and MOC-CNT0.1 obtained similar cost-effectivity for each dose. The overall best results, and several times that were exceeded by both already mentioned modifications (GNs and MWCNTs), were obtained by CSs modification due to its extraordinary enhancement effect and low cost, compared to other modifications. Thus, the 0.1 wt% dispersed in a tannic acid solution is the most suitable variant.

Table 53: MOC mixtures: Cost-effectivity of the additive.

Mixture	Additional cost per m ³ (€)	Flexural strength <i>f_f</i> (MPa)	Compressive strength <i>f_c</i> (MPa)	Cost-effectivity in comparison of:	
				<i>f_f</i> (kPa·€ ⁻¹)	<i>f_c</i> (kPa·€ ⁻¹)
MOC-REF	-	22.32	68.20	-	-
MOC-G0.1	380	24.93	73.86	6.87	14.90
MOC-G0.3	1139	26.25	75.24	3.44	6.18
MOC-G0.5	1899	25.15	65.10	1.49	-1.63
MOC-CNT0.1	259	24.31	71.89	7.67	14.22
MOC-CNT0.3	769	23.12	72.73	1.04	5.89
MOC-CNT0.5	1278	21.36	69.41	-0.75	0.95
MOC-S0.1	129	31.20	81.29	68.62	101.16
MOC-S0.3	391	33.23	82.95	27.92	37.74
MOC-S0.5	652	33.25	69.85	16.76	2.53

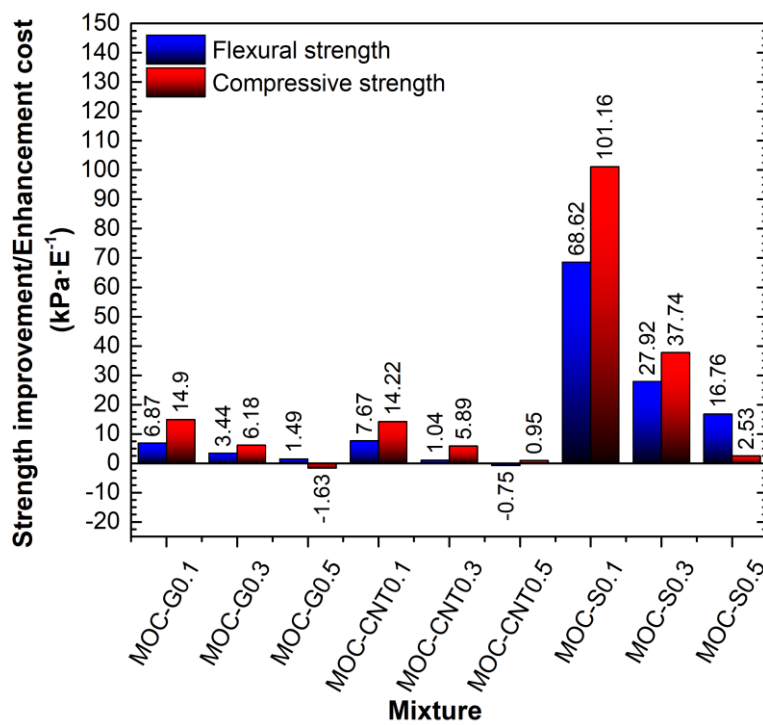


Figure 89: MOC mixtures: Cost-effectivity ratio.

5.2.2 Hydrated Lime Mortars (CL)

The chemical composition of CL compounds obtained by SEM/EDS with the electron microscope Phenom XL G2 is presented in Figs. 90-92. It shows the presence of the main elements Ca and O. The small concentration of the Si aggregate was also measured. The carbon concentration as a result of carbonation is also assumed, but it was too small, and the instrument did not detect it.

In addition, traces of carbon have already been detected in NMs modified mixtures. As can be seen, for example, in the elemental maps of the CL-CNT0.5 (Fig. 91) and CL-S0.3 (Fig. 92), the particles form visible clusters of C that can affect the final physical characteristics, especially the mechanical strength.

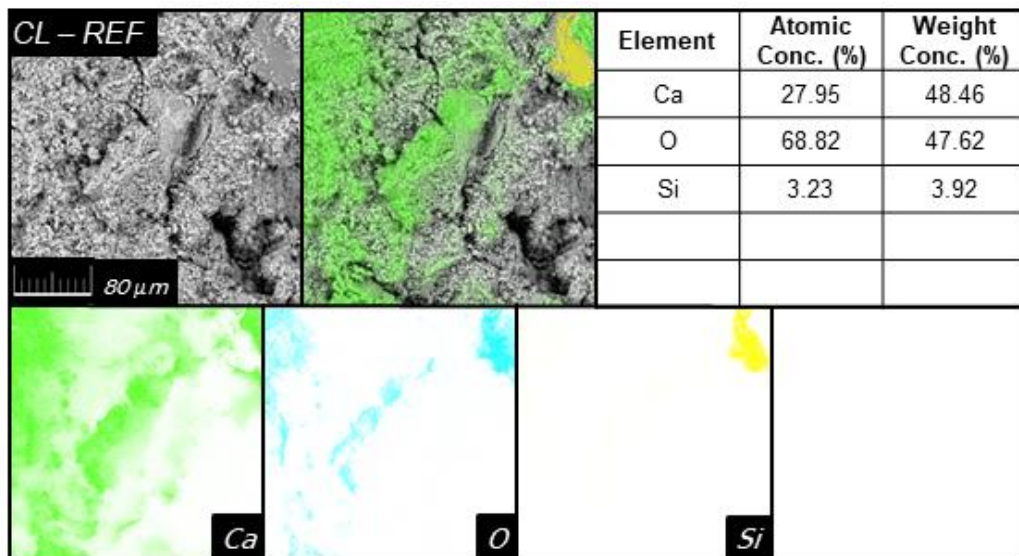


Figure 90: Elemental maps of the CL-REF mixture.

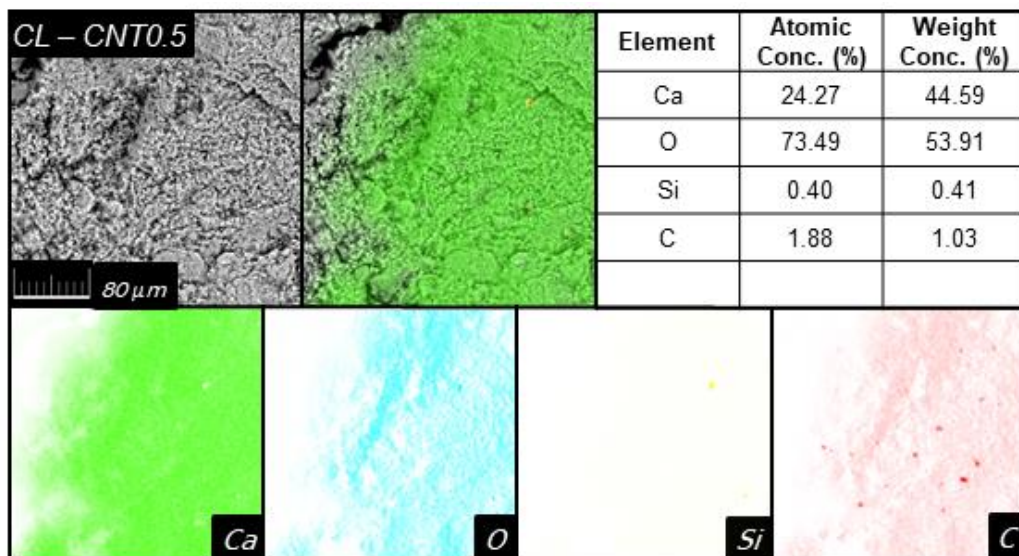


Figure 91: Elemental maps of the CL-CNT0.5 mixture.

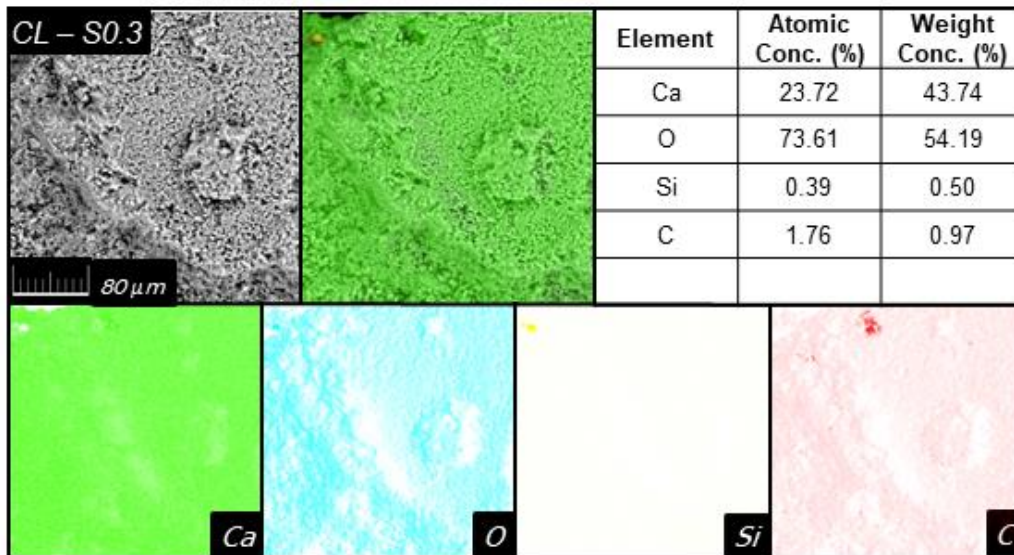


Figure 92: Elemental maps of the CL-S0.3 mixture.

The basic properties of hardened CL mixtures can be seen in Tab. 54. The bulk density of the individual mixtures is in the range of 1566-1673 kg·m⁻³. When GNs and CSs were used, the change of bulk density and specific density compared to the reference mixture was minimal in all cases, within the range of total combined uncertainty. On the other hand, when CNTs were applied with chemical reagents, there was a decrease in bulk density, most of 5% in the case of CL-CNT0.1. Therefore, a higher total porosity was calculated compared to the control mixture. By 3.3 % for CL-CNT0.1, 1.4 % for CL-CNT0.3 and 2 % for CL-CNT0.5.

Table 54: CL mixtures: Basic structural properties.

Mixture	Bulk density ρ_b (kg·m ⁻³)	Specific density ρ_s (kg·m ⁻³)	Porosity ψ (%)
CL-REF	1656 ± 23	2545 ± 31	34.9 ± 0.7
CL-G0.1	1647 ± 23	2545 ± 31	34.7 ± 0.7
CL-G0.3	1669 ± 23	2538 ± 35	34.6 ± 0.7
CL-G0.5	1641 ± 23	2536 ± 22	35.3 ± 0.7
CL-CNT0.1	1566 ± 22	2535 ± 30	38.2 ± 0.8
CL-CNT0.3	1618 ± 23	2538 ± 30	36.3 ± 0.7
CL-CNT0.5	1601 ± 22	2538 ± 30	36.9 ± 0.7
CL-S0.1	1673 ± 23	2542 ± 30	35.6 ± 0.7
CL-S0.3	1655 ± 23	2542 ± 30	34.9 ± 0.7
CL-S0.5	1663 ± 23	2541 ± 30	34.6 ± 0.7

Table 55: CL mixtures: Mechanical strength characteristics.

Mixture	Flexural strength f_r (MPa)	Compressive strength f_c (MPa)	Dynamic modulus of elasticity E (GPa)
CL-REF	0.47 ± 0.01	0.56 ± 0.01	4.22 ± 0.10
CL-G0.1	0.70 ± 0.01	0.75 ± 0.01	4.80 ± 0.11
CL-G0.3	0.63 ± 0.01	0.85 ± 0.01	4.74 ± 0.11
CL-G0.5	0.63 ± 0.01	0.82 ± 0.01	4.57 ± 0.11
CL-CNT0.1	0.46 ± 0.01	0.55 ± 0.01	3.33 ± 0.08
CL-CNT0.3	0.49 ± 0.01	0.69 ± 0.01	3.49 ± 0.08
CL-CNT0.5	0.34 ± 0.01	0.44 ± 0.01	3.24 ± 0.07
CL-S0.1	0.53 ± 0.01	0.72 ± 0.01	3.61 ± 0.08
CL-S0.3	0.49 ± 0.01	0.66 ± 0.01	3.73 ± 0.09
CL-S0.5	0.41 ± 0.01	0.51 ± 0.01	3.51 ± 0.08

The mechanical strength characteristics of the hardened CL mortars are presented in Tab. 55. The application of GNs resulted in a slight increase in the dynamic modulus of elasticity. However, both MWCNTs and CSs enhanced mixtures show a decrease. The change in the case of CL-CNT mixtures occurred as a result of the increase in porosity.

As shown in Tab.55 and Fig.93. The highest flexural strength was obtained by CL-G0.1. The 0.3% and 0.5% dose reached a higher flexural strength compared to CL-REF, however, not as high as CL-G0.1. Despite the assumption, CL-CNTs obtained the lowest flexural strength among the modified mixtures. The increase was recorded only for CL-CNT0.3. Regarding total combined uncertainty, the 0.1% dosage of MWCNTs had no effect on strength. However, 0.5 wt% of NM negatively affect the strength. CSs modification increased flexural strength by 13 %, but higher doses further decreased strength.

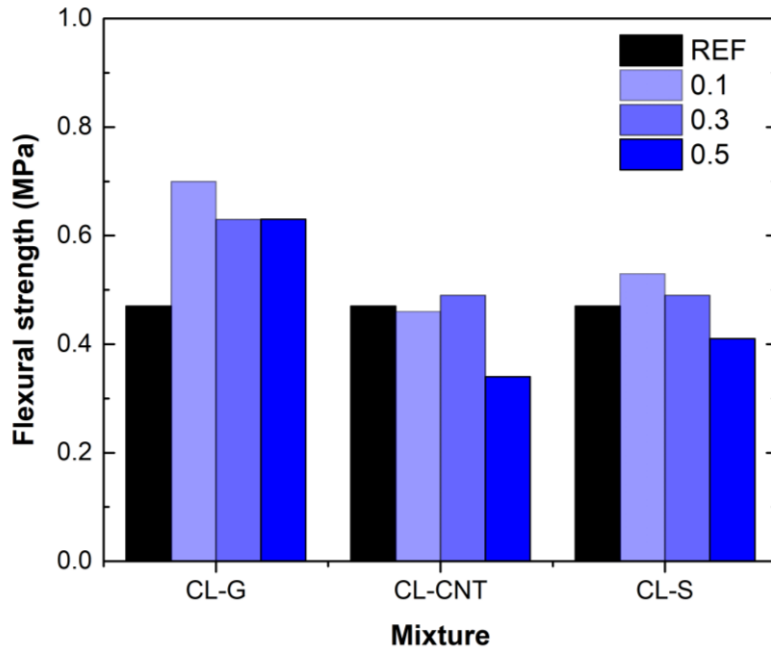


Figure 93: CL mixtures: Flexural strength parameters.

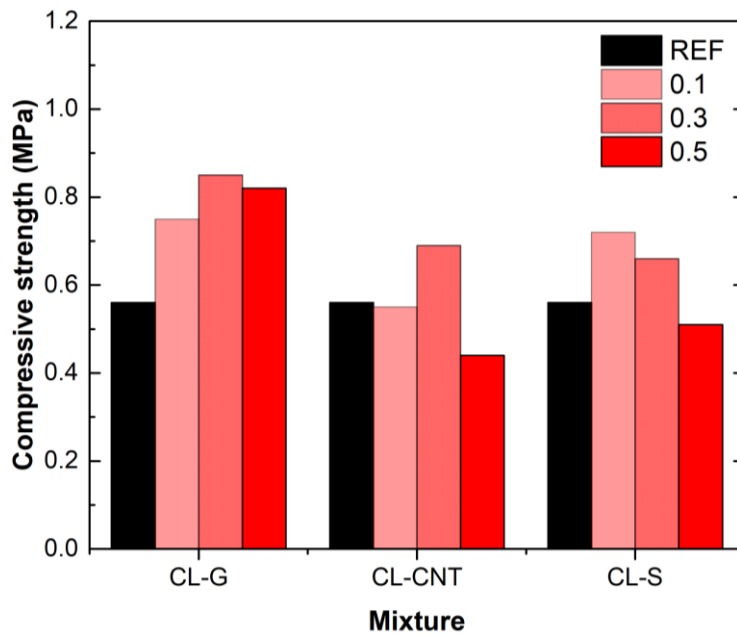


Figure 94: CL mixtures: Compressive strength parameters.

The dependence of compressive strength on the volume of NM dosage is shown in Fig. 94. The best strength obtained CL-G0.3 with a nearly 52 % increase. A higher Nm volume further decreases the strength. When CL is modified with MWCNTs, the 0.1% dose increase in the strength increase of 0.1% dosage was not significant; the increase (23.2 %) was recorded for CL-CNT0.3. CL-S0.1 and CL-S0.3 had a strength of 28.6 % and 17.9 % higher compared to CL-REF. In the case of both CL-CNT and CL-S mixtures, the higher dosage (0.5 wt%) resulted in a decrease in strength, even to a value lower

than the value of the control mixture. From the measured values, it can be seen that the best modification for hydrated lime-based mortars was the use of GNs.

The heat transfer properties, shown in Tab.56, were also affected by NM modification. The addition of NMs to lime-based mortar resulted in an increase in both thermal conductivity and thermal capacity, and the higher the applied volume was. This is most noticeable from the results of CL-CNT. Even when the porosity of CL-CNT0.5 was higher compared to CL-REF, the resulting thermal conductivity was higher due to the addition of a high-conductive material to the material matrix. The highest thermal conductivity (increased by 12.4 %) and heat capacity (increased by 28.1 %) among all tested samples obtained CL-G0.5.

Table 56: CL mixtures: Heat transfer characteristics.

Mixture	Thermal conductivity λ ($W \cdot m^{-1} \cdot K^{-1}$)	Volumetric heat capacity $C_v \times 10^6$ ($J \cdot m^{-3} \cdot K^{-1}$)
CL-REF	1.125 ± 0.025	1.176 ± 0.030
CL-G0.3	1.111 ± 0.024	1.108 ± 0.029
CL-G0.3	1.196 ± 0.026	1.139 ± 0.030
CL-G0.5	1.265 ± 0.028	1.340 ± 0.035
CL-CNT0.1	1.036 ± 0.023	1.153 ± 0.030
CL-CNT0.3	1.094 ± 0.024	1.182 ± 0.031
CL-CNT0.5	1.189 ± 0.026	1.241 ± 0.032
CL-S0.1	1.175 ± 0.026	1.278 ± 0.033
CL-S0.3	1.050 ± 0.023	1.239 ± 0.032
CL-S0.5	1.106 ± 0.024	1.288 ± 0.033

The cost-effectivity of CL mortars is presented in the Tab. 57 and Fig. 95. The results indicate the decreasing cost effectivity of a higher volume of applied NMs due to higher additional costs, even when the CL-G0.3 strength was higher compared to the CL-G0.1. The best cost-effectivity of all additives was reached by CL-S0.1, thus modifying with 0.1 wt% CSs dispersed in tannic acid solution. The second best was CL-G0.1 with a higher flexural strength to cost ratio, but a nearly three-time lower ratio with respect to compressive strength. This was due to the high price of the used GNs. It must be noted that the cost value of CSs modification was based on the assumption that the material was sold at the same price as industrial-grade MWCNTs. The actual price was not determinable because this type of NMs was supplied as waste material. However, the modified mixture of GNs reached the highest total compressive strength.

Table 57: CL mixtures: Cost-effectivity of the additive.

Mixture	Additional cost per m ³ (€)	Flexural strength f_t (MPa)	Compressive strength f_c (MPa)	Cost-effectivity in comparison of:	
				f_t (kPa·€ ⁻¹)	f_c (kPa·€ ⁻¹)
CL-REF	-	0.47	0.56	-	-
CL-G0.1	347	0.70	0.75	0.66	0.55
CL-G0.3	1041	0.63	0.85	0.15	0.28
CL-G0.5	1735	0.63	0.82	0.09	0.15
CL-CNT0.1	230	0.46	0.55	-0.04	-0.04
CL-CNT0.3	691	0.49	0.69	0.03	0.19
CL-CNT0.5	1152	0.34	0.44	-0.11	-0.10
CL-S0.1	112	0.53	0.72	0.53	1.42
CL-S0.3	337	0.49	0.66	0.06	0.30
CL-S0.5	562	0.41	0.51	-0.11	-0.09

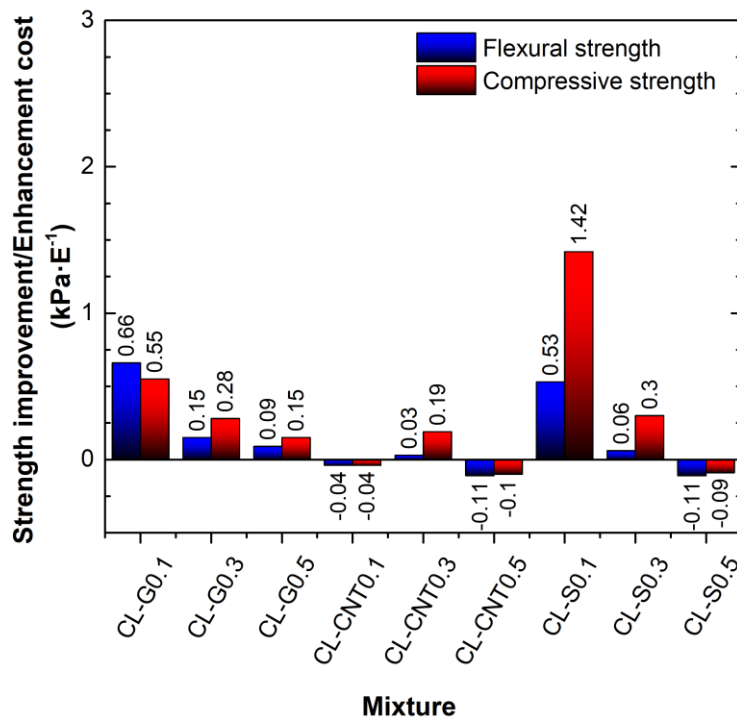


Figure 95: CL mixtures: Cost-effectivity ratio.

5.2.3 Natural Hydraulic Lime Mortars (HL)

The chemical composition of HL composites obtained by SEM/EDS with the electron microscope Phenom XL G2 is presented in Figs. 96 and 92. It shows the presence of the main mortar elements Ca, O, Al, Na, and K. The concentration of Si aggregate was also recorded.

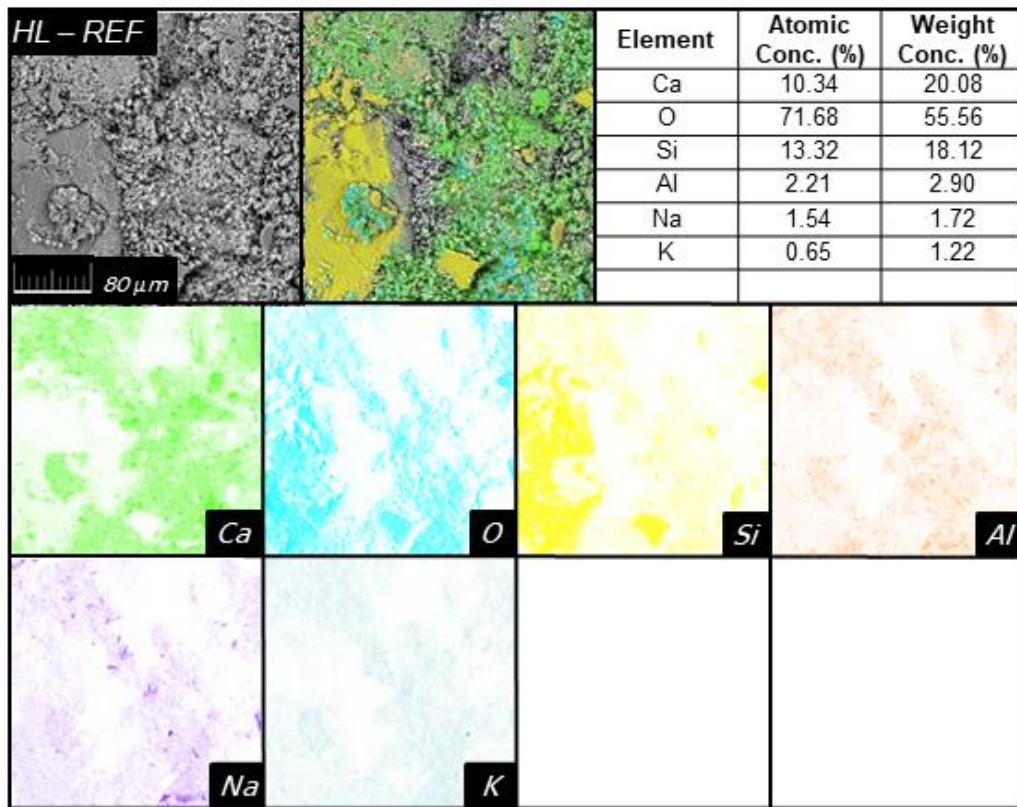


Figure 96: Elemental maps of the HL-REF mixture.

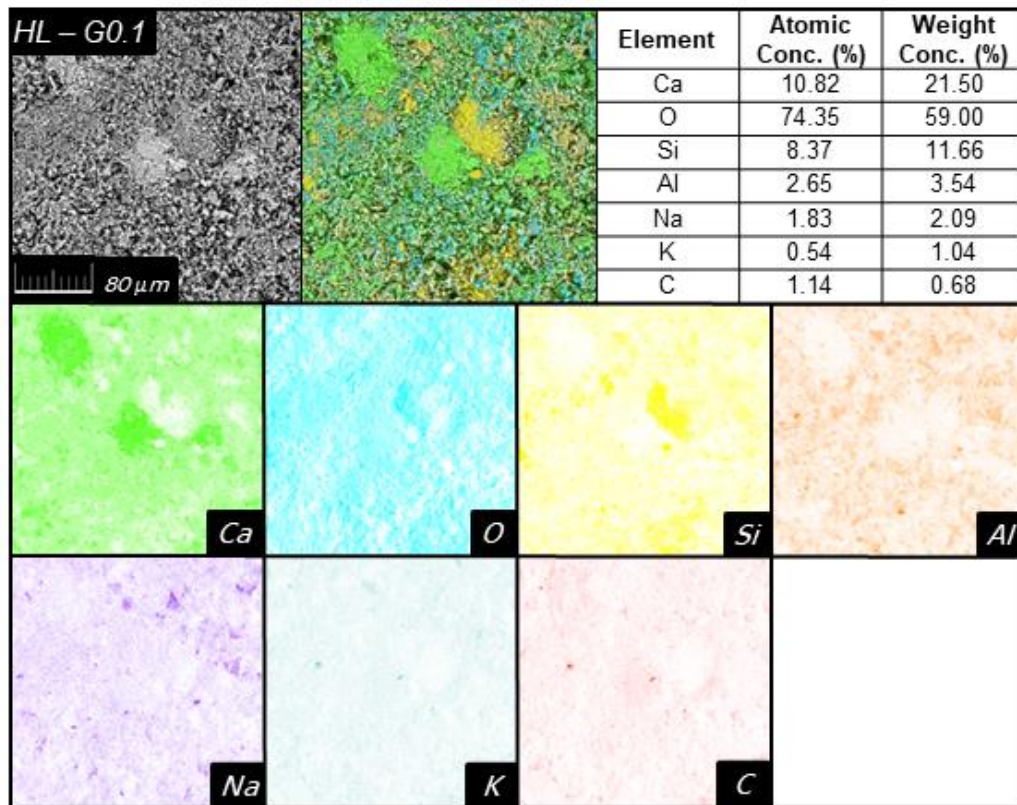


Figure 97: Elemental maps of the HL-G0.1 mixture.

Similarly, to CL mixtures, the carbon concentration formed during carbonation was not detectable in the case of the control mixture (HL-REF). For the elemental maps of NMs modified mixtures, the traces of C are shown throughout the cross section. Additionally, the results show a lower amount of clusters being formed compared to CL mixtures. The example, HL-G0.1 is shown in Fig. 91. This can result in a higher efficiency of the resulting mechanical properties.

Table 58: HL mixtures: Basic structural properties.

Mixture	Bulk density	Specific density	Porosity
	ρ_b ($\text{kg}\cdot\text{m}^{-3}$)	ρ_s ($\text{kg}\cdot\text{m}^{-3}$)	ψ (%)
HL-REF	1741 ± 24	2575 ± 31	32.4 ± 0.6
HL-G0.1	1913 ± 27	2572 ± 31	25.6 ± 0.5
HL-G0.3	1903 ± 27	2564 ± 31	25.8 ± 0.5
HL-G0.5	1870 ± 26	2531 ± 31	26.1 ± 0.5
HL-CNT0.1	1900 ± 27	2578 ± 31	26.3 ± 0.5
HL-CNT0.3	1893 ± 26	2563 ± 31	26.2 ± 0.5
HL-CNT0.5	1881 ± 26	2548 ± 31	26.2 ± 0.5
HL-S0.1	1815 ± 31	2542 ± 30	29.1 ± 0.6
HL-S0.3	1822 ± 31	2542 ± 30	29.6 ± 0.6
HL-S0.5	1825 ± 31	2541 ± 30	30.2 ± 0.6

The basic properties of the HI composites can be seen in Tab. 58. The bulk density range was higher compared to the CL. Although the control sample had a bulk density of 1741 $\text{kg}\cdot\text{m}^{-3}$ and a porosity of 32.4 %, all enhanced mixtures reached a higher bulk density followed by a reduction in total porosity. The application of GNs reduced porosity by more than 6 %. When a higher dose was used, the greater the reduction. On the other hand, HL enhanced with MWCNTs had nearly identical porosity, independent of the size of the NMs and the dosage of chemicals. The highest porosity of the enhanced mixtures had HL-S0.3, only 2.2 % lower compared to the control mixture. Changes in specific density were again only marginal, within total combined uncertainty.

The mechanical strength characteristics of HL mortars are presented in Tab. 59. The application of NMs resulted in a decrease in the dynamic modulus of elasticity despite the lower porosity of all tested mixtures.

Table 59: HL mixtures: Mechanical strength characteristics.

Mixture	Flexural strength f_f (MPa)	Compressive strength f_c (MPa)	Dynamic modulus of elasticity E (GPa)
HL-REF	1.97 ± 0.03	7.03 ± 0.10	13.40 ± 0.31
HL-G0.1	2.01 ± 0.03	11.01 ± 0.15	11.79 ± 0.27
HL-G0.3	2.25 ± 0.03	10.67 ± 0.15	10.41 ± 0.24
HL-G0.5	1.75 ± 0.02	9.59 ± 0.13	8.56 ± 0.20
HL-CNT0.1	5.04 ± 0.07	10.63 ± 0.15	12.03 ± 0.28
HL-CNT0.3	5.74 ± 0.07	10.96 ± 0.15	11.94 ± 0.27
HL-CNT0.5	5.84 ± 0.08	10.56 ± 0.13	11.50 ± 0.26
HL-S0.1	2.00 ± 0.03	5.08 ± 0.07	8.73 ± 0.08
HL-S0.3	0.64 ± 0.01	1.39 ± 0.02	3.91 ± 0.09
HL-S0.5	0.48 ± 0.01	0.83 ± 0.01	3.44 ± 0.08

Fig. 98. shows the extraordinary effect of MWCNTs nano-additive on HL mortar. The strength increase was more than two times greater than the strength of the control mixture. The trend of increasing remains even when 0.5% dose was used. Other samples show a less enhancing effect. The GNs additive in 0.3% dose increases flexural strength by 14 %.

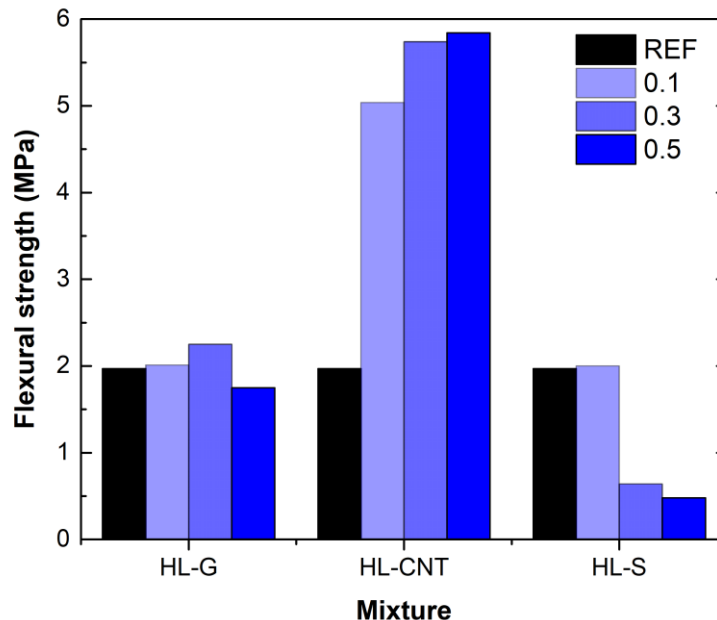


Figure 98: HL mixtures: Flexural strength parameters.

The application of CSs resulted in a slightly higher strength when 0.1 of NM was applied with a further decrease with higher dosages. A huge drop in the compressive

strength of the HL-S mixtures was also observed despite the lower porosity of these mixtures. This was probably due to the chemical reaction of mortar with CSs in combination with tannic acid. However, preliminary tests of HL mortar with tannic acid only resulted in an increase in both flexural (by 45 %) and compressive strengths (by 26 %), therefore, these changes must be further studied.

The best compressive strength was obtained again when 0.1 wt% of GNs were used. This enhances the strength by 56.6 %. Higher dose of 0.3 wt% resulted in a 51.8% increase, while 0.5% dose reached only a 36.4% increase. The decreasing trend with higher NM volume is evident. However, the three MWCNT-modified mixed mixtures studied had a strength greater than 10.5 MPa, with a MOC-CNT0.3 strength of nearly 11 MPa, as shown in Fig. 99.

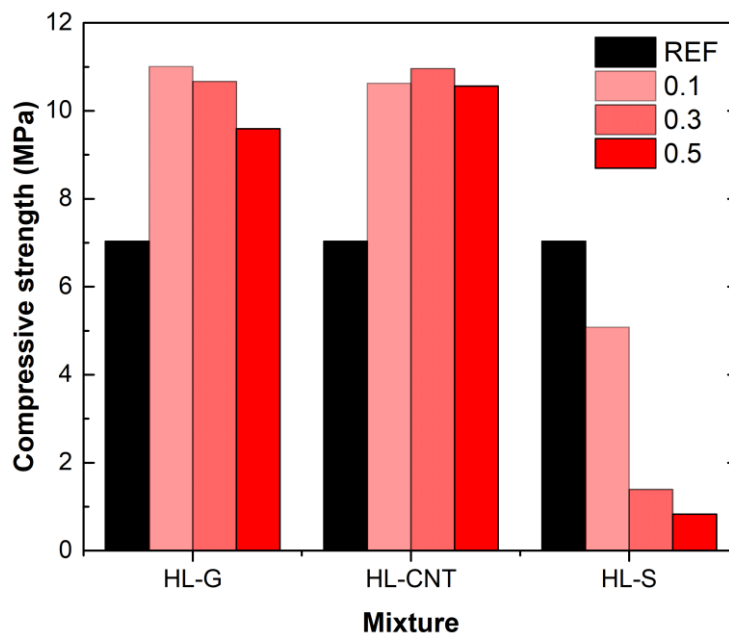


Figure 99: HL mixtures: Compressive strength parameters.

The heat transfer properties are shown in the Tab. 60, were consistent with the results of the total porosity of the HL mortars. The addition of GNs and MWCNTs with surfactants to the lime-based mortar resulted in an increase in both thermal conductivity and heat capacity, with a higher ratio compared to that of the CL mortars. The highest thermal conductivity and heat capacity was obtained by HL-G0.3. The increase was 33.3 % and 25.0 % in thermal conductivity and heat capacity, respectively. When GNs with tannic acid were applied, the thermal conductivity remained similar to that of the HL-Ref value, and the heat capacity increased. However, with higher dosage, the thermal conductivity decreased despite an increase in porosity of 1% and a high volume of conductive NMs. This was again probably due to chemical reactions of tannic acid, which changed the properties of the HL matrix, which must be further studied.

Table 60: HL mixtures: Heat transfer characteristics.

Mixture	Thermal conductivity λ ($\text{W}\cdot\text{m}^{-1}\cdot\text{K}^{-1}$)	Volumetric heat capacity $C_v \times 10^6$ ($\text{J}\cdot\text{m}^{-3}\cdot\text{K}^{-1}$)
HL-REF	1.097 ± 0.024	1.270 ± 0.033
HL-G0.1	1.430 ± 0.024	1.566 ± 0.041
HL-G0.3	1.462 ± 0.026	1.587 ± 0.041
HL-G0.5	1.181 ± 0.028	1.370 ± 0.036
HL-CNT0.1	1.148 ± 0.025	1.250 ± 0.033
HL-CNT0.3	1.280 ± 0.028	1.323 ± 0.034
HL-CNT0.5	1.256 ± 0.028	1.395 ± 0.037
HL-S0.1	1.092 ± 0.024	1.427 ± 0.037
HL-S0.3	0.803 ± 0.018	1.342 ± 0.035
HL-S0.5	0.629 ± 0.014	1.838 ± 0.022

The cost-effectivity of HL mortars is presented in Tab. 61. The results show the decreasing trend of cost-effectivity, higher volume of applied NMs, especially in comparison to compressive strength. The results of HL mixtures except the modified mixture with GNs are presented in Fig. 100. Due to the small changes in the flexural strength of the HL-G mixtures, the effectivity reached a value of 0.

Table 61: HL mixtures: Cost-effectivity of the additive.

Mixture	Additional cost per m^3 (€)	Flexural strength f_f (MPa)	Compressive strength f_c (MPa)	Cost-effectivity in comparison of:	
				f_f ($\text{kPa}\cdot\text{€}^{-1}$)	f_c ($\text{kPa}\cdot\text{€}^{-1}$)
CL-REF	-	1.97	7.03	-	-
CL-G0.1	347	2.01	11.01	0.12	11.50
CL-G0.3	1041	2.25	10.67	0.27	3.51
CL-G0.5	1735	1.75	9.59	-0.13	1.47
CL-CNT0.1	230	5.04	10.63	11.92	13.98
CL-CNT0.3	691	5.74	10.96	4.88	5.09
CL-CNT0.5	1152	5.84	10.56	3.01	2.74
CL-S0.1	112	2.00	5.08	0.27	-17.36
CL-S0.3	337	0.64	1.39	-3.95	-16.74
CL-S0.5	562	0.48	0.83	-2.65	-11.04

However, compared to compressive strength, 0.1 wt% of GNs was the most effective among modified samples. The HL-CNT samples reached extraordinary flexural strength and compressive strength, reaching 11 MPa. Although total compressive strength has been observed on HL-G0.1, the HL-CNT-0.1 obtained better effectivity, regarding the cost of NM addition. Thus, it is the most suitable among the combinations investigated. In case of HL-S mixtures, the cost effectivity reached a negative value, due to their low performance, and was not plotted in Fig. 94.

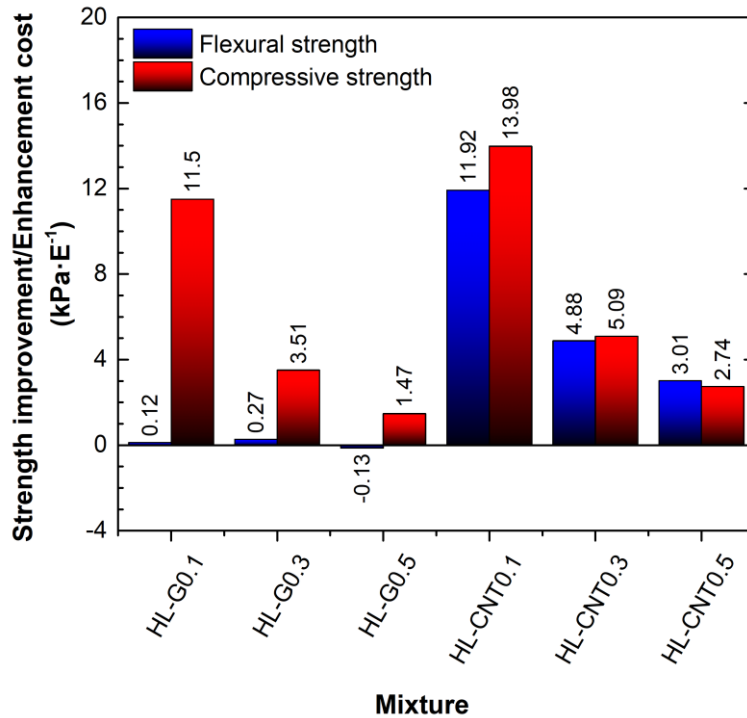


Figure 100: HL mixtures: Cost-effectivity ratio.

In view of the results of this chapter, the following can be concluded. Homogenisation of NMs using an ultrasonic bath was used as the dispersion method in all cases. At the same time, for all mixtures, an additive of 0.1 wt% was the most optimal, considering the mechanical resistance performance and cost.

Two additives, GNs without any chemical agent and CSs dispersed in tannic acid solution, were chosen for the lime hydrate-based mortar. Although CSs performed best with respect to the cost-effective ratio, GNs additive achieved overall higher strength. For the MOC-based mortar, the highest improvement occurred using CSs dispersed in tannic acid solution. Among the natural hydraulic lime mortars, the highest performance was obtained by enhancement using MWCNTs dispersed in a combination of surfactant and antifoamer. This mortar has achieved an extraordinary improvement in flexural strength.

The summary of optimum combination of NM type, dispersion technique, and volume of applied dosage for the most efficient utilisation of NM excellent properties for the composite material characteristics focusing on mechanical durability and cost-effectivity of individual mortar types with standardised composition are presented in Tab. 62.

Table 62: Optimal nano-additive for individual mortars.

Material Variable	Magnesium Oxychloride Cement	Lime Hydrate	Natural Hydraulic Lime
Dispersion Technique	Ultrasonic bath	Ultrasonic bath	Ultrasonic bath
Nanomaterial	Carbon Spheres	Graphene, Carbon Spheres	Multi-walled Carbon Nanotubes
Chemical Additive	Tannic acid	GNs: none CSs: Tannic acid	Triton X100 + Antifoamer
Nanomaterial Dosage	0.1 wt%	GNs: 0.1 wt% CSs: 0.1 wt%	0.1 wt%

6 Conclusion

The application of selected types of nanomaterials for the improvement of light-burnt magnesium oxide and lime-based composites represents one of the suitable methods for the improvement of such materials, especially with regard to their mechanical strength, stiffness and durability. The theoretical part of the work focused on surveying the preparation and use of nanomaterials in the construction industry. In the experimental part, the studied materials were first characterised in detail, then the methodology of preparation and application of nanomaterials was determined, and finally, influence of selected nanomaterials on the characteristics of different types of composites was studied.

The results of the experimental study were divided into several parts, dealing with a composite based on light-burnt MOC consisting of pure MgO phase and mortars designed and prepared according to standard.

From the results of the MOC research, following findings and conclusion were highlighted. A study of the effect of homogenisation techniques on magnesium oxychloride cement (MOC)-based paste with the addition of graphene nanoplatelets showed that a two-step homogenisation process, i.e. homogenisation prior to mixing the mixture and subsequent homogenisation of the fresh mixture, demonstrated exceptional efficiency in uniformly dispersing graphene throughout the material matrix. This fine dispersion resulted in a reduction in porosity and a significant improvement in mechanical resistance. The study showed that the two-stage mixing technique outperformed the one-stage method, offering improved structural and mechanical performance. These results were taken into account in further studies. It should be noted that this method could only be applied in the case of magnesium pastes. The design of the homogeniser did not enable two-stage dispersion of materials containing larger aggregate particles.

A comprehensive analysis of the effect of the specific surface area of graphene on the properties of MOC paste showed that the addition of graphene, with a higher specific surface area, resulted in a significant reduction in porosity and an increase in mechanical strength compared to that of plain MOC paste. GNs C-750 demonstrated superior performance due to a higher specific surface area and smaller particle size. Similar results were obtained using waste carbon spheres.

In the case of investigating the effect of the volume of applied nanomaterial on the MOC paste, a decrease in porosity with increasing NMs dosage was observed. This reduction, together with the excellent properties of GNs resulted in a huge increase in mechanical resistance even at high doses, such as 1.0%. The two-stage homogenisation helped to ensure that this dose of NMs was uniformly incorporated into the fresh mix of the material, thus material matrix.

The combination of different types of nanomaterials, especially 1D and 2D, had a positive effect on the properties of the pastes. In addition to the changes in the macrostructure, the tensile strength was improved, especially when functionalised nanomaterials were used. The resulting strength, mainly influenced by nanotubes, was almost doubled. In terms of compressive strength, the combination of non-functionalised functionalised GNs and MWCNTs was the best. This option was also more cost effective due to the several times higher price of the coated NMs.

The mortar modified with waste carbon spheres also showed exceptionally good properties. In the present example, the low initial cost of the waste nanomaterial and the consequent higher cost-effectivity is another advantageous aspect.

Comparable results were obtained when the standardised mortars were measured. In this part of the thesis, the effect of the dosage of NMs, specifically graphene nanoplatelets (GNs), multiwalled carbon nanotubes (MWCNTs) and carbon spheres (CSs) at doses of 0.1 wt%, 0.3 wt% and 0.5 wt% of binder was investigated.

From the results of the study of standardised mortars, it can be concluded that the modification of MOC mortars based on light-burnt industrial MgO gave similar results in terms of improved strength properties when using 0.1 % of GNs and MWCNTs. However, the use of 0.1 wt% of CSs dispersed in tannic acid outperformed both previous modifications and appears to be the most optimal in terms of both performance and cost-effectivity.

In the case of lime hydrate-based mortars, there was an improvement at lower NM volumes, up to 0.3 by weight. However, due to the high porosity and the low initial strength, the compressive strength did not exceed 1.0 MPa even with the highest improvement rate (52 %) for the CL-G mixture. In terms of the best strength improvements, CL modified with 0.1 % GNs seems to be the most effective. However, modification with CSs achieved lower strength, compared to the latter, but in terms of material price, this combination appears to be a more cost-effective option.

Modification of hydraulic lime-based mortars significantly reduced the porosity of all mixtures. In contrast to the previous example (CL mortars) a rapid increase in flexural strength was obtained by modifying HL with 0.1% of MWCNTs. Together with the increase in compressive strength, modification with MWCNTs appears to be the best in terms of improvement and cost-effectivity among the combinations investigated. The use of CS with tannic acid solution resulted in chemical reactions affecting the material properties and material degradation at higher doses. The subsequent research will focus on this effect as well as on the determination of other material characteristics, such as hygroscopic properties, which, as well as mechanical resistance, are crucial for the use of mortars in building construction.

Based on the results achieved, it was concluded that the use of nano-additives has significant potential in the design and development of advanced composite pastes and mortars with enhanced performance. The results focused on the methodology and ways to determine the best possible method for dispersing and applying of NMs to composite materials. In this work, the positive effect of each additive was demonstrated, as well as the variation in the efficacy of the improvement and its effect on the material characteristics, such as increased or decreased porosity, mechanical durability, etc., depending on the type of modified composite. Therefore, the final properties need to be considered in detail for each type of material base and NM type.

Future research should focus on further possibilities to make more effective NM dispersion. Use of other chemicals, dispersion methods and their effect on industrial grade quality NMs, to achieve favourable results at lower overall nano-additive prices, will be of the particular importance. Furthermore, the excellent thermal and electrical conductivity properties can be utilised in future research to develop new advanced high performance composite materials for the building industry.

References

- [1] SUDHA, Parappurath N; SANGEETHA, Kirubanandam; VIJAYALAKSHMI, Kumar and BARHOUM, Ahmed. Chapter 12 - Nanomaterials history, classification, unique properties, production and market. In: Ahmed BARHOUM a Abdel Salam Hamdy MAKHLOUF (ed.) *Emerging Applications of Nanoparticles and Architecture Nanostructures* [online]. Elsevier, 2018, p. 341–384. ISBN 978-0-323-51254-1. Available from: <https://doi.org/10.1016/B978-0-323-51254-1.00012-9>
- [2] BARHOUM, Ahmed; GARCÍA-BETANCOURT, María Luisa; JEEVANANDAM Jaison; HUSSIEN, Eman A.; MEKKAWY, Sara A. et al. Review on Natural, Incidental, Bioinspired, and Engineered Nanomaterials: History, Definitions, Classifications, Synthesis, Properties, Market, Toxicities, Risks, and Regulations. *Nanomaterials* [online]. 2022, vol. **12**(2), no. 177. ISSN 2079-4991. Available from: <https://doi.org/10.3390/nano12020177>
- [3] FEYNMAN, Richard P. There's plenty of room at the bottom. *Resonance* [online]. 2011, vol. **16**(9), 890–905. ISSN 0973-712X. Available from: <https://doi.org/10.1007/s12045-011-0109-x>
- [4] NELSON, Bradley J. and DONG, Lixin. *Springer Handbook of Nanotechnology, Chapter 18. Nanorobotics* [online]. Berlin, Heidelberg: Springer Berlin Heidelberg, 2017. ISBN 978-3-662-54355-9. Available from: <https://doi.org/10.1007/978-3-662-54357-3>
- [5] EIGLER, D.M. and SCHWEIZER, E.K. Positioning single atoms with a scanning tunnelling microscope. *Nature* [online]. 1990, vol. **344**(6266), p. 524–526. ISSN 1476-4687. Available from: <https://doi.org/10.1038/344524a0>
- [6] THE EUROPEAN COMMISSION. Commission Recommendation of 18 October 2011 on the definition of nanomaterial Text with EEA relevance. *Official Journal of the European Union* [online]. 2011, vol. **275**, p. 38–40. Available from: <https://op.europa.eu/en/publication-detail/-/publication/17af73d9-da70-4a46-a421-c62e3d1df6ce/language-en>
- [7] SHARMA, Virender K.; FILIP, Jan; ZBORIL, Radek and VARMA Rajender S. Natural inorganic nanoparticles – formation, fate, and toxicity in the environment. *Chemical Society Reviews* [online]. 2015, vol. **44**(23), p. 8410–8423. ISSN 0306-0012. Available from: <https://doi.org/10.1039/C5CS00236B>
- [8] JEEVANANDAM, Jaison; BARHOUM, Ahmed; CHAN, Yen S; DUFRESNE, Alain and DANQUAH, Michael K. Review on nanoparticles and nanostructured materials: history, sources, toxicity and regulations. *Beilstein Journal of*

- Nanotechnology* [online]. 2018, vol. **9**, p. 1050–1074. ISSN 2190-4286. Available from: <https://doi.org/10.3762/bjnano.9.98>
- [9] WAGNER, Stephan, GONDIKAS, Andreas; NEUBAUER, Elisabeth; HOFMANN, Thilo and VON DER KAMMER, Frank. Spot the Difference: Engineered and Natural Nanoparticles in the Environment—Release, Behavior, and Fate. *Angewandte Chemie International Edition* [online]. 2014, vol. **53**(46), p. 12398–12419. ISSN 1433-7851. Available from: <https://doi.org/10.1002/anie.201405050>
- [10] MOHAJERANI, Abbas; BURNETT, Lucas; SMITH, John V.; KURMUS, Halenur; MILAS, John et al. Nanoparticles in Construction Materials and Other Applications, and Implications of Nanoparticle Use. *Materials* [online]. 2019, vol. **12**(19), no. 3052. ISSN 1996-1944. Available from: <https://doi.org/10.3390/ma12193052>
- [11] MALAKAR, Arindam, KANEL, Sushil R.; RAY, Chittaranjan; SNOW, Daniel D. and NADAGOUDA, Mallikarjuna N. Nanomaterials in the environment, human exposure pathway, and health effects: A review. *Science of The Total Environment* [online]. 2021, vol. **759**, no. 143470. ISSN 00489697. Available from: <https://doi.org/10.1016/j.scitotenv.2020.143470>
- [12] JOUDEH, Nadeem and LINKE, Dirk. Chapter 5 - Nanoparticle classification, physicochemical properties, characterization, and applications: a comprehensive review for biologists. *Journal of Nanobiotechnology* [online]. 2022, vol. **20**(1), no. 262. ISSN 1477-3155. Available from: <https://doi.org/10.1186/s12951-022-01477-8>
- [13] MAJHI, Kartick Chandra and YADAV, Mahendra. Synthesis of inorganic nanomaterials using carbohydrates. In: INMUDDIN; BODDULA, Rajender; AHMED, Mohd Imran; ASIRI, Abdullah M. (ed.) *Green Sustainable Process for Chemical and Environmental Engineering and Science* [online]. Elsevier, 2021, p. 109–135. ISBN 9780128218877. Available from: <https://doi.org/10.1016/B978-0-12-821887-7.00003-3>
- [14] DALAL, Sejal P. and DALAL, Purvang. Experimental Investigation on Strength and Durability of Graphene Nanoengineered Concrete. *Construction and Building Materials* [online]. 2021, vol. **276**, no. 122236. ISSN 0950-0618. Available from: <https://doi.org/10.1016/j.conbuildmat.2020.122236>
- [15] OGANOV, Artem R.; HEMLEY, Russell J.; HAZEN Robert M., and JONES, Adrian P. Structure, Bonding, and Mineralogy of Carbon at Extreme Conditions. *Reviews in Mineralogy and Geochemistry* [online]. 2013, vol. **75**(1), p. 47–77. ISSN 1529-6466. Available from: <https://doi.org/10.2138/rmg.2013.75.3>

- [16] SMITH, Andrew T.; LACHANCE, Anna Marie; ZENG, Songshan; LIU, Bin and SUN, Luyi. Synthesis, properties, and applications of graphene oxide/reduced graphene oxide and their nanocomposites. *Nano Materials Science* [online]. 2019, vol. **1**(1), p. 31–47. ISSN 25899651.
Available from: <https://doi.org/10.1016/j.nanoms.2019.02.004>.
- [17] ZHANG, Ruiyu; YU, Xin; YANG, Qiwu; CUI, Gan and LI, Zili. The role of graphene in anti-corrosion coatings: A review. *Construction and Building Materials* [online]. 2021, vol. **294**, no. 123613. ISSN 09500618.
Available from: <https://doi.org/10.1016/j.conbuildmat.2021.123613>
- [18] CZERNIAK-RECZULSKA, M.; NIEDZIELSKA, A. and JĘDRZEJCZAK, A. Graphene as a Material for Solar Cells Applications. *Advances in Materials Science* [online]. 2015, vol. **15**(4), no. 67–81. ISSN 2083-4799. Available from: <https://doi.org/10.1515/adms-2015-0024>
- [19] SUN, Ling. Structure and synthesis of graphene oxide. *Chinese Journal of Chemical Engineering* [online]. 2019, vol. **27**(10), p. 2251–2260. ISSN 10049541.
Available from: <https://doi.org/10.1016/j.cjche.2019.05.003>
- [20] MBAYACHI, Vestince B.; NDAYIRAGIJE, Euphrem; SAMMANI, Thirasara; TAJ, Sunaina; MBUTA Elice R. et al. Graphene synthesis, characterization and its applications: A review. *Results in Chemistry* [online]. 2021, vol. **3**, no. 100163. ISSN 22117156. Available from: <https://doi.org/10.1016/j.rechem.2021.100163>
- [21] YAN, Yuxin; NASHATH, Fathima Zahra; CHEN, Sharon; MANICKAM, Sivakumar; LIM, Siew Shee et al. Synthesis of graphene: Potential carbon precursors and approaches. *Nanotechnology Reviews* [online]. 2020, vol. **9**(1), p. 1284–1314. ISSN 2191-9097. Available from: <https://doi.org/10.1515/ntrev-2020-0100>
- [22] KAIRI, Muhammad Izhar; DAYOU, Sebastian; KAIRI, Nurul Izni; BAKAR, Suriani Abu; VIGOLO, Brigitte et al. Toward high production of graphene flakes – a review on recent developments in their synthesis methods and scalability. *Journal of Materials Chemistry A* [online]. 2018, vol. **6**(31), p. 15010–15026. ISSN 2050-7488. Available from: <https://doi.org/10.1039/C8TA04255A>
- [23] NIARAKI ASLI, Amir Ehsan; GUO, Jingshuai; LAI, Pei Lun; MONTAZAMI, Reza and HASHEMI, Nicole N. High-Yield Production of Aqueous Graphene for Electrohydrodynamic Drop-on-Demand Printing of Biocompatible Conductive Patterns. *Biosensors* [online]. 2020, vol. **10**(1), no. 6. ISSN 2079-6374. Available from: <https://doi.org/10.3390/bios10010006>
- [24] CHEN, Jinfeng; DUAN, Miao and CHEN, Guohua. Continuous mechanical exfoliation of graphene sheets via three-roll mill. *Journal of Materials Chemistry*

- [online]. 2012, vol. **22**(37), no. 19625. ISSN 0959-9428. Available from: <https://doi.org/10.1039/c2jm33740a>
- [25] JAYASENA, Buddhika and SUBBIAH, Sathyan. A novel mechanical cleavage method for synthesizing few-layer graphenes. *Nanoscale Research Letters* [online]. 2011, vol. **6**(1), no. 95. ISSN 1556-276X. Available from: <https://doi.org/10.1186/1556-276X-6-95>
- [26] XU, Yanyan; CAO, Huizhe; XUE, Yanqin; LI, Biao and CAI, Weihua. Liquid-Phase Exfoliation of Graphene: An Overview on Exfoliation Media, Techniques, and Challenges. *Nanomaterials* [online]. 2018, vol. **8**(11), no. 942. ISSN 2079-4991. Available from: <https://doi.org/10.3390/nano8110942>
- [27] SUN, Zhenyu; FAN, Qun; ZHANG, Mingli; LIU, Shizhen; TAO, Hengcong et al. Supercritical Fluid-Facilitated Exfoliation and Processing of 2D Materials. *Advanced Science* [online]. 2019, vol. **6**(18). ISSN 2198-3844. Available from: <https://doi.org/10.1002/advs.201901084>
- [28] YU, Pei; LOWE, Sean E.; SIMON, George P. and ZHONG, Yu Lin. Electrochemical exfoliation of graphite and production of functional graphene. *Current Opinion in Colloid & Interface Science* [online]. 2015, vol. **20**(5–6), p. 329–338. ISSN 13590294. Available from: <https://doi.org/10.1016/j.cocis.2015.10.00>
- [29] LOWE, Sean E.; SHI, Ge; ZHANG, Yubai; QIN, Jiadong; JIANG, Lixue et al. The role of electrolyte acid concentration in the electrochemical exfoliation of graphite: Mechanism and synthesis of electrochemical graphene oxide. *Nano Materials Science* [online]. 2019, vol. **1**(3), p. 215–223. ISSN 25899651. Available from: <https://doi.org/10.1016/j.nanoms.2019.07.001>
- [30] MISHRA, Neeraj; BOECKL, John; MOTTA, Nunzio and IACOPI, Francesca. Graphene growth on silicon carbide: A review. *physica status solidi (a)* [online]. 2016, vol. **213**(9), p. 2277–2289. ISSN 1862-6300. Available from: <https://doi.org/10.1002/pssa.201600091>
- [31] SAEED, Maryam; ALSHAMMARI, Yousef; MAJEED, Shereen A. and AL-NASRALLAH, Eissa. Chemical Vapour Deposition of Graphene—Synthesis, Characterisation, and Applications: A Review. *Molecules* [online]. 2020, vol. **25**(17), no. 3856. ISSN 1420-3049. Available from: <https://doi.org/10.3390/molecules25173856>
- [32] ZHANG, Yi; ZHANG, Luyao and ZHOU, Chongwu. Review of Chemical Vapor Deposition of Graphene and Related Applications. *Accounts of Chemical Research* [online]. 2013, vol. **46**(10), p. 2329–2339. ISSN 0001-4842. Available from: <https://doi.org/10.1021/ar300203n>

- [33] MIAO, Congqin; ZHENG, Churan; LIANG, Owen and XIE, Ya-Hong. Chemical Vapor Deposition of Graphene. In: *Physics and Applications of Graphene - Experiments* [online]. InTech, 2011.
Available from: <https://doi.org/10.5772/15543>
- [34] WARNER, Jamie H.; SCHÄFFEL, Franziska; BACHMATIUK, Alicja and RÜMMELI, Mark H. Methods for Obtaining Graphene. In: *Graphene* [online]. Elsevier, 2013, p. 129–228. Available from: <https://doi.org/10.1016/B978-0-12-394593-8.00004-7>
- [35] YANG, Xiaohua; ZHANG, Gaixia; PRAKASH, Jai; CHEN, Zhangsen; GAUTHIER, Marc et al. Chemical vapour deposition of graphene: layer control, the transfer process, characterisation, and related applications. *International Reviews in Physical Chemistry* [online]. 2019, vol. **38**(2), p. 149–199. ISSN 0144-235X. Available from: <https://doi.org/10.1080/0144235X.2019.1634319>
- [36] ESMAEILPOUR, Meysam; BÜGEL, Patrick; FINK, Karin; STUDDT, Felix; WENZEL, Wolfgang et al. Multiscale Model of CVD Growth of Graphene on Cu(111) Surface. *International Journal of Molecular Sciences* [online]. 2023, vol. **24**(10), no. 8563. ISSN 1422-0067.
Available from: <https://doi.org/10.3390/ijms24108563>
- [37] RATHINAVEL, S.; PRIYADHARSHINI K. and PANDA, Dhananjaya. A review on carbon nanotube: An overview of synthesis, properties, functionalization, characterization, and the application. *Materials Science and Engineering: B* [online]. 2021, vol. **268**, no. 115095. ISSN 09215107. Available from: <https://doi.org/10.1016/j.mseb.2021.115095>
- [38] EATEMADI, Ali; DARAEE, Hadis; KARIMKHANLOO, Hamzeh; KOUHI, Mohammad; ZARGHAMI, Nosratollah et al. Carbon nanotubes: properties, synthesis, purification, and medical applications. *Nanoscale Research Letters* [online]. 2014, vol. **9**(1), no. 393. ISSN 1556-276X. Available from: <https://doi.org/10.1186/1556-276X-9-393>
- [39] ASLAM, Mian Muhammad-Ahson; KUO, Hsion-Wen; DEN, Walter; USMAN, Muhammad; SULTAN Muhammad et al. Functionalized Carbon Nanotubes (CNTs) for Water and Wastewater Treatment: Preparation to Application. *Sustainability* [online]. 2021, vol. **13**(10), no. 5717. ISSN 2071-1050. Available from: <https://doi.org/10.3390/su13105717>
- [40] IHSANULLAH; ABBAS, Aamir; AL-AMER, Adnan M.; LAOUI, Tahar; AL-MARRI, Mohammed J. et al. Heavy metal removal from aqueous solution by advanced carbon nanotubes: Critical review of adsorption applications. *Separation and*

- Purification Technology* [online]. 2016, col. **157**, p. 141–161. ISSN 13835866. Available from: <https://doi.org/10.1016/j.seppur.2015.11.039>
- [41] SHEIKHPOUR, Mojgan; NAGHINEJAD, Maryam; KASAEIAN, Alibakhsh; LOHRASBI, Armaghan; SHAHRAEINI, Seyed Sadegh et al. The Applications of Carbon Nanotubes in the Diagnosis and Treatment of Lung Cancer: A Critical Review. *International Journal of Nanomedicine* [online]. 2020, vol. **15**, p. 7063–7078. ISSN 1178-2013. Available from: <https://doi.org/10.2147/IJN.S263238>
- [42] KUMAR JAGADEESAN, Aravind; THANGAVELU, Krithiga and DHANANJEYAN, Venkatesan. Carbon Nanotubes: Synthesis, Properties and Applications. In: *21st Century Surface Science - a Handbook* [online]. IntechOpen, 2020. Available from: <https://doi.org/10.5772/intechopen.92995>
- [43] VAJTAI, R.; WEI, B. Q.; and AJAYAN, P. M. Controlled growth of carbon nanotubes. *Philosophical Transactions of the Royal Society of London. Series A: Mathematical, Physical and Engineering Sciences* [online]. 2004, vol. **362**(1823), p. 2143–2160. ISSN 1364-503X. Available from: <https://doi.org/10.1098/rsta.2004.1433>
- [44] SHOUKAT, Rizwan and KHAN, Muhammad Imran. Carbon nanotubes: a review on properties, synthesis methods and applications in micro and nanotechnology. *Microsystem Technologies* [online]. 2021, vol. **27**(12), p. 4183–4192. ISSN 0946-7076. Available from: <https://doi.org/10.1007/s00542-021-05211-6>
- [45] LIU, Zheng-Guang; HE, Xiang-Xi; ZHAO, Jia-Hua; XU, Chun-Mei; QIAO, Yun et al. Carbon nanosphere synthesis and applications for rechargeable batteries. *Chemical Communications* [online]. 2023, vol. **59**(29), p. 4257–4273. ISSN 1359-7345. Available from: <https://doi.org/10.1039/D3CC00402C>
- [46] YAO, Yaqi; XU, Jinming; HUANG, Yanqiang and ZHANG, Tao. Synthesis and applications of carbon nanospheres: A review. *Particuology* [online]. 2024, vol. **87**, p. 325–338. ISSN 16742001. Available from: <https://doi.org/10.1016/j.partic.2023.09.007>
- [47] CHANG, Pei-Yi; BINDUMADHAVAN, Kartick and DOONG, Ruey-An. Size Effect of Ordered Mesoporous Carbon Nanospheres for Anodes in Li-Ion Battery. *Nanomaterials* [online]. 2015, vol. **5**(4), p. 2348–2358. ISSN 2079-4991. Available from: <https://doi.org/10.3390/nano5042348>
- [48] BA, Thong Le; BOHUS, Marcell; LUKÁCS, István Endre; WONGWISES, Somchai; GRÓF, Gyula et al. Comparative Study of Carbon Nanosphere and Carbon Nanopowder on Viscosity and Thermal Conductivity of Nanofluids. *Nanomaterials* [online]. 2021, vol. **11**(3), no. 608. ISSN 2079-4991. Available from: <https://doi.org/10.3390/nano11030608>

- [49] HERCZEG, Márton; MCKINNON, David; MILIOS, Leonidas; BAKAS, Ioannis; Erik KLAASSENS, Erik et al. *Resource efficiency in the building sector: Final report*. 2014.
- [50] UNITED NATIONS ENVIRONMENT PROGRAMME (2021). *2021 Global Status Report for Buildings and Construction: Towards a Zero-emission, Efficient and Resilient Buildings and Construction Sector* [online]. 2021 [accessed 2023-11-18]. Available from: <https://globalabc.org/resources/publications/2021-global-status-report-buildings-and-construction>
- [51] IEA (2018). *Technology Roadmap - Low-Carbon Transition in the Cement Industry* [online]. 2018 [accessed 2023-11-18]. Available from: <https://www.iea.org/reports/technology-roadmap-low-carbon-transition-in-the-cement-industry>
- [52] WTA Merkblatt 2-9-04/D: *Sanierputzsysteme, Wissenschaftlich-Technische Arbeitsgemeinschaft für Bauwerkserhaltung und Denkmalpflege. Pfaffenhofen an der Ilm*. Germany: WTA Publications. 2005.
- [53] NGUYEN, Van Son; ROUXEL, Didier and VINCENT, Brice. Dispersion of nanoparticles: From organic solvents to polymer solutions. *Ultrasonics Sonochemistry* [online]. 2014, vol. **21**(1), p. 149–153. ISSN 13504177. Available from: <https://doi.org/10.1016/j.ultsonch.2013.07.015>
- [54] ZAWRAH, M.F.; KHATTAB, R.M.; EL-KHESHEN, A.A. and FADALY, Ezzat EL. Sintering and properties of borosilicate glass/Li-Na-K-feldspar composites for electronic applications. *Ceramics International* [online]. 2017, vol. **43**(17), p. 15068–15073. ISSN 02728842. Available from: <https://doi.org/10.1016/j.ceramint.2017.08.033>
- [55] ZHOU, Lingyun; ZHANG, Hui; ZHANG, Hui and ZHANG, Zhong. Homogeneous nanoparticle dispersion prepared with impurity-free dispersant by the ball mill technique. *Particuology* [online]. 2013, vol. **11**(4), p. 441–447. ISSN 16742001. Available from: <https://doi.org/10.1016/j.partic.2013.01.001>
- [56] KUMAR, Manish; XIONG, Xinni; WAN, Zhonghao; SUN, Yuqing; TSANG, Daniel C.W. et al. Ball milling as a mechanochemical technology for fabrication of novel biochar nanomaterials. *Bioresource Technology* [online]. 2020, vol. **312**, no. 123613. ISSN 09608524. Available from: <https://doi.org/10.1016/j.biortech.2020.123613>
- [57] GAO, Ziqi; HAN, Quanjiabao; LIU, Jianbang; ZHAO, Kangbo; YU, Yin et al. Dispersion of Carbon Nanotubes Improved by Ball Milling to Prepare Functional Epoxy Nanocomposites. *Coatings* [online]. 2023, vol. **13**(3), no. 649. ISSN 2079-6412. Available from: <https://doi.org/10.3390/coatings13030649>

- [58] MANIER, Nicolas; GARAUD, Maël; DELALAIN, Patrice; AGUERRE-CHARIOL, Olivier and PANDARD, Pascal. Behaviour of ceria nanoparticles in standardized test media – influence on the results of ecotoxicological tests. *Journal of Physics: Conference Series* [online]. 2011, vol. **304**, no. 012058. ISSN 1742-6596. Available from: <https://doi.org/10.1088/1742-6596/304/1/012058>
- [59] LABAN, Geoff; NIES, Loring F.; TURCO, Ronald F.; BICKHAM John W. and SEPÚLVEDA, Maria S. The effects of silver nanoparticles on fathead minnow (*Pimephales promelas*) embryos. *Ecotoxicology* [online]. 2010, vol. **19**(1), p. 185–195. ISSN 0963-9292. Available from: <https://doi.org/10.1007/s10646-009-0404-4>
- [60] TEANMETAWONG, S; CHANTARAMANEE, T.; LHOSUPASIRIRAT, S.; WONGARIYAKAWEE, A. and SRIKHIRIN, T. A Comparison Study of Magnetic Stirrer and Sonicator Technique to Disperse 1% Span20 Treated Layered Double Hydroxides (LDHs). *IOP Conference Series: Materials Science and Engineering* [online]. 2019, vol. **654**(1), no. 012005. ISSN 1757-8981. Available from: <https://doi.org/10.1088/1757-899X/654/1/012005>
- [61] DEBBARMA, Khumber; DEBNATH, Barnali and SARKAR, Partha Pratim. A comprehensive review on the usage of nanomaterials in asphalt mixes. *Construction and Building Materials* [online]. 2022, vol. **361**, no. 129634. ISSN 09500618. Available from: <https://doi.org/10.1016/j.conbuildmat.2022.129634>
- [62] ZHOU, Nan; WANG, Shuncaï and WALSH, Frank C. Effective particle dispersion via high-shear mixing of the electrolyte for electroplating a nickel-molybdenum disulphide composite. *Electrochimica Acta* [online]. 2018, vol. **283**, p. 568–577. ISSN 00134686. Available from: <https://doi.org/10.1016/j.electacta.2018.06.187>
- [63] BAŁDYGA, Jerzy; ORCIUCH, Wojciech; MAKOWSKI, Łukasz; MALIK, Katarzyna; ÖZCAN-TAŞKIN, Gül et al. Dispersion of Nanoparticle Clusters in a Rotor–Stator Mixer. *Industrial & Engineering Chemistry Research* [online]. 2008, vol. **47**(10), p. 3652–3663. ISSN 0888-5885. Available from: <https://doi.org/10.1021/ie070899u>
- [64] KAUR, Inder; ELLIS, Laura-Jayne; ROMER, Isabella; TANTRA, Ratna; CARRIERE, Marie et al. Dispersion of Nanomaterials in Aqueous Media: Towards Protocol Optimization. *Journal of Visualized Experiments* [online]. 2017, vol. **130**, no. 56074. ISSN 1940-087X. Available from: <https://doi.org/10.3791/56074>
- [65] ALAM, A.K.M. Moshiul. Methods of nanoparticle dispersion in the polymer matrix. In: *Nanoparticle-Based Polymer Composites* [online]. Elsevier, 2022, p. 469–479. Available from: <https://doi.org/10.1016/B978-0-12-824272-8.00008-7>

- [66] TANTRA, R.; OKSEL, C.; ROBINSON, K.N.; SIKORA, A. ; WANG, X.Z. et al. A method for assessing nanomaterial dispersion quality based on principal component analysis of particle size distribution data. *Particuology* [online]. 2015, vol. **22**, p. 30–38. ISSN 16742001.
Available from: <https://doi.org/10.1016/j.partic.2014.10.004>
- [67] KOO, Doheon; SUNG, Jaebum; SUH, Heongwon; BAE, Sungchul and SO, Hongyun. Comprehensive analysis of CNT/NS/GO composites: Dispersion effect of graphene oxide for environmental sensor application. *Composites Part A: Applied Science and Manufacturing* [online]. 2023, vol. **173**, no. 107639. ISSN 1359835X.
Available from: <https://doi.org/10.1016/j.compositesa.2023.107639>
- [68] LAU, Kin-tak; LU, Mei.; LAM, Chun-ki; CHEUNG, Hoi-yan.; SHENG, Fen-Lin et al. Thermal and mechanical properties of single-walled carbon nanotube bundle-reinforced epoxy nanocomposites: the role of solvent for nanotube dispersion. *Composites Science and Technology* [online]. 2005, vol. **65**(5), p. 719–725. ISSN 02663538.
Available from: <https://doi.org/10.1016/j.compscitech.2004.10.005>
- [69] ZHENG, Nianben; WANG, Long and SUN, Zhiqiang. The effects of ultrasonication power and time on the dispersion stability of few-layer graphene nanofluids under the constant ultrasonic energy consumption condition. *Ultrasonics Sonochemistry* [online]. 2021, vol. **80**, no. 105816. ISSN 13504177. Available from: <https://doi.org/10.1016/j.ultsonch.2021.105816>
- [70] ASADI, Amin; ALARIFI, Ibrahim M.; ALI, Vakkar and NGUYEN, Hoang M. An experimental investigation on the effects of ultrasonication time on stability and thermal conductivity of MWCNT-water nanofluid: Finding the optimum ultrasonication time. *Ultrasonics Sonochemistry* [online]. 2019, vol. **58**, no. 104639. ISSN 13504177.
Available from: <https://doi.org/10.1016/j.ultsonch.2019.104639>
- [71] ASADI, Amin; POURFATTAH, Farzad; MIKLÓS SZILÁGYI, Imre; AFRAND, Masoud; ŻYŁA, Gawel et al. Effect of sonication characteristics on stability, thermophysical properties, and heat transfer of nanofluids: A comprehensive review. *Ultrasonics Sonochemistry* [online]. 2019, vol. **58**, no. 104701. ISSN 13504177.
Available from: <https://doi.org/10.1016/j.ultsonch.2019.104701>
- [72] HÅKANSSON, Andreas and RAYNER, Marilyn. General Principles of Nanoemulsion Formation by High-Energy Mechanical Methods.

- In: *Nanoemulsions* [online]. Elsevier, 2018, p. 103–139. Available from: <https://doi.org/10.1016/B978-0-12-811838-2.00005-9>
- [73] HARTMANN, Nanna B.; JENSEN, Keld Alstrup; BAUN, Anders; RASMUSSEN, Kirsten; RAUSCHER, Hubert et al. Techniques and Protocols for Dispersing Nanoparticle Powders in Aqueous Media—Is there a Rationale for Harmonization? *Journal of Toxicology and Environmental Health, Part B* [online]. 2015, vol. **18**(6), p. 299–326. ISSN 1093-7404. Available from: <https://doi.org/10.1080/10937404.2015.1074969>
- [74] CORTÉS, Hernán; HERNÁNDEZ-PARRA, Héctor; BERNAL-CHÁVEZ, Sergio A.; PRADO-AUDELO, María L. Del; CABALLERO-FLORÁN, Isaac H. et al. Non-Ionic Surfactants for Stabilization of Polymeric Nanoparticles for Biomedical Uses. *Materials* [online]. 2021, vol. **14**(12), no. 3197. ISSN 1996-1944. Available from: <https://doi.org/10.3390/ma14123197>
- [75] YU, Fan; CHEN, Yingying; LIANG, Xingbo; XU, Jiale; LEE, Chiahsun et al. Dispersion stability of thermal nanofluids. *Progress in Natural Science: Materials International* [online]. 2017, vol. **27**(5), p. 531–542. ISSN 10020071 Available from: <https://doi.org/10.1016/j.pnsc.2017.08.010>
- [76] RIZVI, Marziya; GERENGI, Husnu and GUPTA, Preeti. Chapter 1 - Functionalization of Nanomaterials: Synthesis and Characterization. In: VERMA, Chandrabhan, HUSSAIN, Chaudhery Mustansar and QURAIISHI, Mumtaz A. (ed.) *Functionalized Nanomaterials for Corrosion Mitigation: Synthesis, Characterization, and Applications. ACS Symposium Series* [online]. American Chemical Society, 2022, vol. **1418**, p. 1–26. ISBN: 978-0-841-29759-3. Available from: <https://doi.org/10.1021/bk-2022-1418.ch001>
- [77] BAIG, Nadeem; KAMMAKAKAM, Irshad and FALATH, Wail. Nanomaterials: a review of synthesis methods, properties, recent progress, and challenges. *Materials Advances* [online]. 2021, vol. **2**(6), p. 1821–1871. ISSN 2633-5409. Available from: <https://doi.org/10.1039/D0MA00807A>
- [78] CARDENAS-BENITEZ, Braulio; DJORDJEVIC, Ivan; HOSSEINI, Samira; MADOU Marc J. and MARTINEZ-CHAPA, Sergio O. Review—Covalent Functionalization of Carbon Nanomaterials for Biosensor Applications: An Update. *Journal of The Electrochemical Society* [online]. 2018, vol. **165**(3), no. B103. ISSN 0013-4651. Available from: <https://doi.org/10.1149/2.0381803jes>
- [79] ALOSIME, Eid M. A review on surface functionalization of carbon nanotubes: methods and applications. *Discover Nano* [online]. 2023, vol. **18**(1), no. 12. ISSN 2731-9229. Available from: <https://doi.org/10.1186/s11671-023-03789-6>

- [80] IVANCIC, Tomislav; THOMPSON, Michael R.; PAWLAK, John L. and LAWTON, David J.W. Influence of anionic and non-ionic surfactants on nanoparticle synthesis by solvent-free extrusion emulsification. *Colloids and Surfaces A: Physicochemical and Engineering Aspects* [online]. 2020, vol. **587**, no. 124328. ISSN 09277757.
Available from: <https://doi.org/10.1016/j.colsurfa.2019.124328>
- [81] MADHU BABU, K.; TAMBE, Pankaj and SIVANAGARAJU, N. Surfactant assisted dispersion of graphene: A review. *Materials Today: Proceedings* [online]. 2023. ISSN 22147853. Available from: <https://doi.org/10.1016/j.matpr.2023.04.336>
- [82] RAHMAN, Md. Mahfuzur; YOUNES, Hammad; SUBRAMANIAN, Navaladian and AL GHAFERI, Amal. Optimizing the Dispersion Conditions of SWCNTs in Aqueous Solution of Surfactants and Organic Solvents. *Journal of Nanomaterials* [online]. 2014, vol. **2014**, p. 1–11. ISSN 1687-4110. Available from: <https://doi.org/10.1155/2014/102621>
- [83] ALEXANDER, Kevin; SHESHRAO GAJGHATE, Sameer; SHANKAR KATARKAR, Anil; MAJUMDER, Abhik and BHAUMIK, Swapan. Role of nanomaterials and surfactants for the preparation of graphene nanofluid: A review. *Materials Today: Proceedings* [online]. 2021, vol. **44**, p. 1136–1143. ISSN 22147853. Available from: <https://doi.org/10.1016/j.matpr.2020.11.231>
- [84] YANG, HeeBong; NEAL, Neil; FLORES, Elijah Earl; ADRONOV, Alex and KIM, Na Young. Role and impact of surfactants in carbon nanotube dispersions and sorting. *Journal of Surfactants and Detergents* [online]. 2023, vol. **26**(5), p. 607–622. ISSN 1097-3958. Available from: <https://doi.org/10.1002/jsde.12702>
- [85] SELVAM, C.; MOHAN LAL, D. and HARISH, Sivasankaran. Enhanced heat transfer performance of an automobile radiator with graphene based suspensions. *Applied Thermal Engineering* [online]. 2017, vol. **123**, p. 50–60. ISSN 13594311. Available from: <https://doi.org/10.1016/j.applthermaleng.2017.05.076>
- [86] DAS, Sidhartha; GIRI, Asis; SAMANTA, Sutanu and KANAGARAJ, S. Role of graphene nanofluids on heat transfer enhancement in thermosyphon. *Journal of Science: Advanced Materials and Devices* [online]. 2019, vol. **4**(1), p. 163–169. ISSN 24682179. Available from: <https://doi.org/10.1016/j.jsamd.2019.01.005>
- [87] MEHRALI, Mohammad; SADEGHINEZHAD, Emad; ROSEN, Marc A.; AKHIANI, Amir Reza; TAHAN LATIBARI, Sara et al. Experimental investigation of thermophysical properties, entropy generation and convective heat transfer for a nitrogen-doped graphene nanofluid in a laminar flow regime. *Advanced Powder Technology* [online]. 2016, vol. **27**(2), p. 717–727. ISSN 09218831. Available from: <https://doi.org/10.1016/j.appt.2016.02.028>

- [88] AGARWAL, Deepak Kumar; VAIDYANATHAN, Aravind and SUNIL KUMAR, S.. Experimental investigation on thermal performance of kerosene–graphene nanofluid. *Experimental Thermal and Fluid Science* [online]. 2016, vol. **71**, p. 126–137. ISSN 08941777.
Available from: <https://doi.org/10.1016/j.expthermflusci.2015.10.028>
- [89] ILYAS, Suhaib Umer; RIDHA, Syahrir and ABDUL KAREEM, Firas Ayad. Dispersion stability and surface tension of SDS-Stabilized saline nanofluids with graphene nanoplatelets. *Colloids and Surfaces A: Physicochemical and Engineering Aspects* [online]. 2020, vol. **592**, no. 124584. ISSN 09277757.
Available from: <https://doi.org/10.1016/j.colsurfa.2020.124584>
- [90] ZAMAN, Ali Can; KAYA, Figen and KAYA, Cengiz. A study on optimum surfactant to multiwalled carbon nanotube ratio in alcoholic stable suspensions via UV–Vis absorption spectroscopy and zeta potential analysis. *Ceramics International* [online]. 2020, vol. **46**(18), p. 29120–29129. ISSN 02728842. Available from: <https://doi.org/10.1016/j.ceramint.2020.08.085>
- [91] DE ALMEIDA CARÍSIO, Pedro; DOS SANTOS MENDONÇA, Yasmim Gabriela; SOARES, Carlos Fernando Teodósio; REALES, Oscar Aurelio Mendoza; DE MORAES REGO FAIRBAIRN, Eduardo et al. Dispersion of Carbon Nanotubes with Different Types of Superplasticizer as a Dispersing Agent for Self-Sensing Cementitious Materials. *Applied Sciences* [online]. 2021, vol. **11**(18), no. 8452. ISSN 2076-3417. Available from: <https://doi.org/10.3390/app11188452>
- [92] YALCIN, B. and CAKMAK, M. The role of plasticizer on the exfoliation and dispersion and fracture behavior of clay particles in PVC matrix: a comprehensive morphological study. *Polymer* [online]. 2004, vol. **45**(19), p. 6623–6638. ISSN 00323861. Available from: <https://doi.org/10.1016/j.polymer.2004.06.061>
- [93] SATHYAN, Dhanya and ANAND, Kalpathy Balakrishnan. Influence of superplasticizer family on the durability characteristics of fly ash incorporated cement concrete. *Construction and Building Materials* [online]. 2019, vol. **204**, p. 864–874. ISSN 09500618.
Available from: <https://doi.org/10.1016/j.conbuildmat.2019.01.171>
- [94] MA, Guowei and WANG, Li. A critical review of preparation design and workability measurement of concrete material for largescale 3D printing. *Frontiers of Structural and Civil Engineering* [online]. 2018, vol. **12**(3), p. 382–400. ISSN 2095-2430. Available from: <https://doi.org/10.1007/s11709-017-0430-x>
- [95] CHEN, Yu; LI, Xingchen; LI, Chuangchuang; ZHANG, Nana; LIU, Ronggui et al. Improvement of Flexural and Compressive Strength of Cement Mortar by

- Graphene Nanoplatelets. *The Open Civil Engineering Journal* [online]. 2021, vol. **15**(1), p. 165–171. ISSN 1874-1495.
Available from: <https://doi.org/10.2174/1874149502115010165>
- [96] SONG, Xiaobin; SHANG, Susu; CHEN, Dandan and GU, Xianglin. Multi-walled carbon nanotube reinforced mortar-aggregate interfacial properties. *Construction and Building Materials* [online]. 2017, vol. **133**, p. 57–64. ISSN 09500618.
Available from: <https://doi.org/10.1016/j.conbuildmat.2016.12.034>
- [97] DALLA, Panagiota T.; TRAGAZIKIS, Ilias K.; TRAKAKIS, George; GALIOTIS, Costas; DASSIOS, Konstantinos G. et al. Multifunctional Cement Mortars Enhanced with Graphene Nanoplatelets and Carbon Nanotubes. *Sensors* [online]. 2021, vol. **21**(3), no. 933. ISSN 1424-8220. Available from: <https://doi.org/10.3390/s21030933>
- [98] DONG, Wenkui; LI, Wengui; WANG, Kejin; HAN, Baoguo; SHENG, Daichao et al. Investigation on physicochemical and piezoresistive properties of smart MWCNT/cementitious composite exposed to elevated temperatures. *Cement and Concrete Composites* [online]. 2020, vol. **112**, no. 103675. ISSN 09589465.
Available from: <https://doi.org/10.1016/j.cemconcomp.2020.103675>
- [99] MANZUR, Tanvir; YAZDANI, Nur and EMON, Md. Abul Bashar. Potential of Carbon Nanotube Reinforced Cement Composites as Concrete Repair Material. *Journal of Nanomaterials* [online]. 2016, vol. **2016**, p. 1–10. ISSN 1687-4110.
Available from: <https://doi.org/10.1155/2016/1421959>
- [100] CHAIPANICH, Arnon; NOCHAIYA, Thanongsak; WONGKEO, Watcharapong and TORKITTIKUL, Pincha. Compressive strength and microstructure of carbon nanotubes–fly ash cement composites. *Materials Science and Engineering: A* [online]. 2010, vol. **527**(4–5), p. 1063–1067. ISSN 09215093. Available from: <https://doi.org/10.1016/j.msea.2009.09.039>
- [101] GE, Zhi; QIN, Jin; SUN, Renjuan; GUAN, Yanhua; ZHANG, Hongzhi et al. The Effect of the Addition of Graphene Nanoplatelets on the Selected Properties of Cementitious Composites. *Frontiers in Built Environment* [online]. 2021, vol. **7**, no. 673346. ISSN 2297-3362.
Available from: <https://doi.org/10.3389/fbuil.2021.673346>
- [102] JEEVANAGOUDAR, Yashavant V; KRISHNA, R. Hari; GOWDA, Raje; PREETHAM, R. and PRABHAKARA, R. Improved mechanical properties and piezoresistive sensitivity evaluation of MWCNTs reinforced cement mortars. *Construction and Building Materials* [online]. 2017, vol. **144**, p. 188–194. ISSN 09500618.
Available from: <https://doi.org/10.1016/j.conbuildmat.2017.03.139>

- [103] ALAFOGIANNI, P.; DASSIOS, K.; TSAKIROGLOU, C.D.; MATIKAS, T.E. and BARKOULA, N.M. Effect of CNT addition and dispersive agents on the transport properties and microstructure of cement mortars. *Construction and Building Materials* [online]. 2019, vol. **197**, p. 251–261. ISSN 09500618. Available from: <https://doi.org/10.1016/j.conbuildmat.2018.11.169>
- [104] GHOLAMPOUR, Aliakbar; KIAMAHALLEH, Meisam Valizadeh; TRAN, Diana N. H.; OZBAKKALOGLU, Togay and LOSIC, Dusan. Revealing the dependence of the physiochemical and mechanical properties of cement composites on graphene oxide concentration. *RSC Advances* [online]. 2017, vol. **7**(87), p. 55148–55156. ISSN 2046-2069.
Available from: <https://doi.org/10.1039/C7RA10066C>
- [105] PAVLOPOULOU, Lydia-Chara; DIMOU, Angeliki-Eirini; STOGIA, Maria-Evangelia; METAXA, Zoi S.; KOURKOULIS, Stavros K. et al. Lime-based nanocomposites for masonry restoration: Towards the implementation of small-scale restoration. *Materials Today: Proceedings* [online]. 2023, vol. **93**, p. 761–766. ISSN 22147853. Available from: <https://doi.org/10.1016/j.matpr.2023.06.348>
- [106] DIMOU, Angeliki-Eirini; METAXA, Zoi S.; ALEXOPOULOS, Nikolaos D. and KOURKOULIS, Stavros K. Assessing the potential of nano-reinforced blended lime-cement pastes as self-sensing materials for restoration applications. *Materials Today: Proceedings* [online]. 2022, vol. **62**, p. 2482–2487. ISSN 22147853. Available from: <https://doi.org/10.1016/j.matpr.2022.02.623>
- [107] DIMOU, Angeliki-Eirini; CHARALAMPIDOU, Christina-Margarita; METAXA, Zoi S.; KOURKOULIS, Stavros K.; KARATASIOS, Ioannis et al. Mechanical and electrical properties of hydraulic lime pastes reinforced with carbon nanomaterials. *Procedia Structural Integrity* [online]. 2020, vol. **28**, p. 1694–1701. ISSN 24523216. Available from: <https://doi.org/10.1016/j.prostr.2020.10.144>
- [108] HENRIQUE NALON, Gustavo; LOPES RIBEIRO, José Carlos; GONÇALVES PEDROTI, Leonardo; MARCIO DA SILVA, Roberto; NERY DUARTE DE ARAÚJO, Eduardo et al. Smart laying mortars for masonry structures: effects of lime/cement ratio and carbon nanomaterials content on self-sensing behavior. *Cement and Concrete Composites* [online]. 2024, vol. **145**, no. 105351. ISSN 09589465.
Available from: <https://doi.org/10.1016/j.cemconcomp.2023.105351>
- [109] FARIA, Paulina; DUARTE, Paulo; BARBOSA, Davide and FERREIRA, Isabel. New composite of natural hydraulic lime mortar with graphene oxide. *Construction and Building Materials* [online]. 2017, vol. **156**, p. 1150–1157. ISSN 09500618. Available from: <https://doi.org/10.1016/j.conbuildmat.2017.09.072>

- [110] LAUERMANNOVÁ, Anna-Marie; JANKOVSKÝ, Ondřej; SEDMIDUBSKÝ, David; LOJKA, Michal; PAVLÍKOVÁ, Milena et al. Case study on MOC composites enriched by foamed glass and ground glass waste: Experimental assessment of material properties and performance. *Case Studies in Construction Materials* [online]. 2023, vol. **18**, no. e01836. ISSN 22145095. Available from: <https://doi.org/10.1016/j.cscm.2023.e01836>
- [111] EN 1015-1. *Methods of test for mortar for masonry - Part 1: Determination of particle size distribution (by sieve analysis)*. Brussels: European Committee for Standardization. 1999.
- [112] SIGMA ALDRICH. *Carbon Nanomaterials* [online]. 2023 [accessed 2023-12-18]. Available from: <https://www.sigmaaldrich.com/DE/en/products/materials-science/electronic-materials/carbon-nanomaterials>
- [113] ACS MATERIAL. *Graphene Oxide Products* [online]. 2023 [accessed 2023-12-18]. Available from: <https://www.acsmaterial.com/materials/graphene-series/graphene-oxide.html>
- [114] TIMES NANO. *Industrial Multi-wall CNTs* [online]. 2023 [accessed 2023-12-18]. Available from: <http://www.timesnano.com/en/product.php?prt=3,30,87>
- [115] PAVLÍKOVÁ, Milena; KAPICOVÁ, Adéla; ZÁLESKÁ, Martina; PIVÁK, Adam; JANKOVSKÝ, Ondřej et al. Ultra-high strength multicomponent composites based on reactive magnesia: Tailoring of material properties by addition of 1D and 2D carbon nanoadditives. *Journal of Building Engineering* [online]. 2022, vol. **50**, no. 104122. ISSN 23527102. Available from: <https://doi.org/10.1016/j.jobe.2022.104122>
- [116] *Institute of Plasma Physics of the Czech Academy of Sciences (IPP CAS)* [online]. [accessed. 2023-12-18]. Available from: <https://www.ipp.cas.cz/>
- [117] JIŘÍČKOVÁ, Adéla; LAUERMANNOVÁ, Anna-Marie; JANKOVSKÝ, Ondřej; FATHI, Jafar; ZÁLESKÁ, Martina et al. Utilization of waste carbon spheres in magnesium oxychloride cement. *Case Studies in Construction Materials* [online]. 2023, vol. **19**, no. e02374. ISSN 22145095. Available from: <https://doi.org/10.1016/j.cscm.2023.e02374>
- [118] MERCK KGaA. *Tween 80* [online]. 2023 [accessed 2023-12-18]. Available from: <https://www.sigmaaldrich.com/DE/en/substance/123459005656>
- [119] P-LAB a.s. *Tween 80* [online]. 2023 [accessed 2023-12-18]. Available from: <https://www.p-lab.cz/tweensupsup-80>
- [120] CARL ROTH GmbH + Co. KG. *Triton X 100* [online]. 2023 [accessed 2023-12-18]. Available from: <https://www.p-lab.cz/tweensupsup-80>

- [121] MERCK KGaA. *Triton X 100* [online]. 2023 [accessed 2023-12-18]. Available from: <https://www.sigmaaldrich.com/DE/en/search/triton-x-100?focus=products&page=1&perpage=30&sort=relevance&term=triton%20x%20100&type=product>
- [122] CARL ROTH GmbH + Co. KG. *Tannic acid* [online]. 2023 [accessed 2023-12-18]. Available from: <https://www.carlroth.com/com/en/a-to-z/tannic-acid/p/2726.2>
- [123] MERCK KGAA. *Tannic acid* [online]. 2023 [accessed 2023-12-18]. Available from: <https://www.sigmaaldrich.com/DE/en/substance/tannicacid1701201401554>
- [124] WANG, Tao; JING, Li-Chao; ZHU, Qingxia; SAGADEVAN ETHIRAJ, Anita; FAN, Xiaowei et al. Tannic acid modified graphene/CNT three-dimensional conductive network for preparing high-performance transparent flexible heaters. *Journal of Colloid and Interface Science* [online]. 2020, vol. **577**, p. 300–310. ISSN 00219797. Available from: <https://doi.org/10.1016/j.jcis.2020.05.084>
- [125] SAN ANDRÉS, María Paz; BAÑOS-CABRERA, Marina; GUTIÉRREZ-FERNÁNDEZ, Lucía; DÍEZ-PASCUAL, Ana María a VERA-LÓPEZ, Soledad. Fluorescence Study of Riboflavin Interactions with Graphene Dispersed in Bioactive Tannic Acid. *International Journal of Molecular Sciences* [online]. 2021, vol. **22**(10), no. 5270. ISSN 1422-0067. Available from: <https://doi.org/10.3390/ijms22105270>
- [126] DEOTALE, Shweta M.; DUTTA, Sayantani; MOSES, J. A. and ANANDHARAMAKRISHNAN, C. Foaming and defoaming—concepts and their significance in food and allied industries: a review. *Discover Chemical Engineering* [online]. 2023, vol. **3**(1), no. 9. ISSN 2730-7700. Available from: <https://doi.org/10.1007/s43938-023-00025-6>
- [127] DENKOV, Nikolai D. and MARINOVA, Krastanka G. Antifoam Effects of Solid Particles, Oil Drops and Oil—Solid Compounds in Aqueous Foams. In: *Colloidal Particles at Liquid Interfaces* [online]. Cambridge University Press, 2006, p. 383–444. Available from: <https://doi.org/10.1017/CBO9780511536670.011>
- [128] ZÁLESKÁ, Martina; PAVLÍKOVÁ, Milena; PIVÁK, Adam; MARUŠIAK, Šimon; JANKOVSKÝ, Ondřej et al. MOC Doped with Graphene Nanoplatelets: The Influence of the Mixture Preparation Technology on Its Properties. *Materials* [online]. 2021, vol. **14**(6), no. 1450. ISSN 1996-1944. Available from: <https://doi.org/10.3390/ma14061450>
- [129] LAUERMANNOVÁ, Anna-Marie; LOJKA, Michal; JANKOVSKÝ, Ondřej; FALTYSOVÁ, Ivana; SEDMIDUBSKÝ, David et al. The influence of graphene specific surface on material properties of MOC-based composites for construction

- use. *Journal of Building Engineering* [online]. 2021, vol. **43**, no. 103193. ISSN 23527102. Available from: <https://doi.org/10.1016/j.jobbe.2021.103193>
- [130] LAUERMANNNOVÁ, Anna-Marie; LOJKA, Michal; SKLENKA, Jan; ZÁLESKÁ, Martina; PAVLÍKOVÁ, Milena et al. Magnesium oxychloride-graphene composites: Towards high strength and water resistant materials for construction industry. *FlatChem* [online]. 2021, vol. **29**, no. 100284. ISSN 24522627. Available from: <https://doi.org/10.1016/j.flatc.2021.100284>
- [131] LAUERMANNNOVÁ, Anna-Marie; JANKOVSKÝ, Ondřej; LOJKA, Michal; FALTYSOVÁ, Ivana; SLÁMOVÁ, Julie et al. Co-Doped Magnesium Oxychloride Composites with Unique Flexural Strength for Construction Use. *Materials* [online]. 2022, vol. **15**(2), no. 604. ISSN 1996-1944. Available from: <https://doi.org/10.3390/ma15020604>
- [132] EN 459-2. *Building lime - Part 2: Test methods*. Brussels: European Committee for Standardization. 2021.
- [133] KAPICOVÁ, Adéla; PIVÁK, Adam; ZÁLESKÁ, Martina; PAVLÍKOVÁ Milena and PAVLÍK, Zbyšek. Influence of different surfactants on hydrated lime pastes modified with CNTs. *AIP Conference Proceedings* [online]. 2023, no. 130006. Available from: <https://doi.org/10.1063/5.0162199>
- [134] PETKOVA, B.; TCHOLAKOVA, S. and DENKOV, N. Foamability of surfactant solutions: Interplay between adsorption and hydrodynamic conditions. *Colloids and Surfaces A: Physicochemical and Engineering Aspects* [online]. 2021, vol. **626**, no. 127009. ISSN 0927-7757. Available from: <https://doi.org/10.1016/j.colsurfa.2021.127009>
- [135] EN 196-6. *METHODS OF TESTING CEMENT – PART 6: DETERMINATION OF FINENESS*. Brussels: European Committee for Standardization. 2019.
- [136] SINGH, Avanish; KUMAR, Rakesh and GOEL, Pankaj. Factors influencing strength of magnesium oxychloride cement. *Construction and Building Materials* [online]. 2021, vol. **303**, no. 124571. ISSN 09500618. Available from: <https://doi.org/10.1016/j.conbuildmat.2021.124571>
- [137] EN 933-2. *Tests for geometrical properties of aggregates - Part 2: Determination of particle size distribution - Test sieves, nominal size of apertures, nominal size of apertures*. Brussels: European Committee for Standardization. 2021.
- [138] EN 1015-3. *Methods of test for mortar for masonry - Part 3: Determination of consistence of fresh mortar (by flow table)*. Brussels: European Committee for Standardization. 2000.

- [139] EN 1015-10. *Methods of test for mortar for masonry - Part 10: Determination of dry bulk density of hardened mortar*. Brussels: European Committee for Standardization. 2000.
- [140] EN 1015-11. *Methods of test for mortar for masonry - Part 11: Determination of flexural and compressive strength of hardened mortar*. Brussels: European Committee for Standardization. 1999.
- [141] EN 12504-4. *Testing concrete in structures - Part 4: Determination of ultrasonic pulse velocity*. Brussels: European Committee for Standardization. 2022.
- [142] EN 1015-18. *Methods of test for mortar for masonry - Part 18: Determination of water absorption coefficient due to capillary action of hardened mortar*. Brussels: European Committee for Standardization. 2003.
- [143] PAN, Jin; FENG, Kun; WANG, Pengju; CHEN Haiming a YANG, Wenqian. Retardation and compressive strength enhancement effect of upcycling waste carrot as bio-admixture for cement mortars. *Journal of Building Engineering* [online]. 2022, vol. **62**, no. 105402. ISSN 23527102. Available from: <https://doi.org/10.1016/j.job.2022.105402>
- [144] MAHZUZ, H. M. A.; CHOUDHURY, Mohammed Ridwan; AHMED, Anindya Rakib and RAY, Sourav. Effect of material strength on the cost of RCC building frames. *SN Applied Sciences* [online]. 2020, vol. **2**(1), no. 46. ISSN 2523-3963. Available from: <https://doi.org/10.1007/s42452-019-1830-4>
- [145] JANKOVSKÝ, Ondřej; LOJKA, Michal; LAUERMANNOVÁ, Anna-Marie; ANTONČÍK, Filip; PAVLÍKOVÁ, Milena et al. Carbon Dioxide Uptake by MOC-Based Materials. *Applied Sciences* [online]. 2020, vol. **10**(7), no. 2254. ISSN 2076-3417. Available from: <https://doi.org/10.3390/app10072254>
- [146] GÓCHEZ, Roque; WAMBAUGH, Jim; ROCHNER, Brett and KITCHENS, Christopher L. Kinetic study of the magnesium oxychloride cement cure reaction. *Journal of Materials Science* [online]. 2017, vol. **52**(13), p. 7637–7646. ISSN 0022-2461. Available from: <https://doi.org/10.1007/s10853-017-1013-x>
- [147] MISRA, A. K. and MATHUR, Renu. Magnesium oxychloride cement concrete. *Bulletin of Materials Science* [online]. 2007, vol. **30**(3), p. 239–246. ISSN 0250-4707. Available from: <https://doi.org/10.1007/s12034-007-0043-4>
- [148] GUO, Yingying; ZHANG, Yixia; SOE, Khin and PULHAM, Mark. Recent development in magnesium oxychloride cement. *Structural Concrete* [online]. 2018, vol. **19**(5), p. 1290–1300. ISSN 1464-4177. Available from: <https://doi.org/10.1002/suco.201800077>

- [149] MATKOVIC, BORIS and YOUNG, J. F. Microstructure of Magnesium Oxychloride Cements. *Nature Physical Science* [online]. 1973, vol. **246**(153), p. 79–80. ISSN 0300-8746. Available from: <https://doi.org/10.1038/physci246079a0>
- [150] KING, Julia A.; KLIMEK, Danielle R.; MISKIOGLU, Ibrahim and ODEGARD, Greg M. Mechanical properties of graphene nanoplatelet/epoxy composites. *Journal of Applied Polymer Science* [online]. 2013, vol. **128**(6), p. 4217–4223. ISSN 0021-8995. Available from: <https://doi.org/10.1002/app.38645>
- [151] HUANG, Qing. THE EFFECT OF SILICA FUME ON THE DURABILITY OF MAGNESIUM OXYCHLORIDE CEMENT. *Ceramics - Silikaty* [online]. 2019, p. 338–346. ISSN 1804-5847. Available from: <https://doi.org/10.13168/cs.2019.0029>
- [152] MINDESS, Sidney. *Developments in the Formulation and Reinforcement of Concrete* [online]. Elsevier, 2019. ISBN 978-0-08-102616-8. Available from: <https://doi.org/10.1016/C2017-0-03347-5>
- [153] FENG, Chi; GUIMARÃES, Ana Sofia; RAMOS, Nuno; SUN, Lixin; GAWIN, Dariusz et al. Hygric properties of porous building materials (VI): A round robin campaign. *Building and Environment* [online]. 2020, vol. **185**, no. 107242. ISSN 03601323. Available from: <https://doi.org/10.1016/j.buildenv.2020.107242>
- [154] KIM, Seong Yun; NOH, Ye Ji and YU, Jaesang. Thermal conductivity of graphene nanoplatelets filled composites fabricated by solvent-free processing for the excellent filler dispersion and a theoretical approach for the composites containing the geometrized fillers. *Composites Part A: Applied Science and Manufacturing* [online]. 2015, vol. **69**, p. 219–225. ISSN 1359835X. Available from: <https://doi.org/10.1016/j.compositesa.2014.11.018>
- [155] ELSAID, Khaled; ABDELKAREEM, Mohammad Ali; MAGHRABIE, Hussein M.; SAYED, Enas Taha; WILBERFORCE, Tabbi et al. Thermophysical properties of graphene-based nanofluids. *International Journal of Thermofluids* [online]. 2021, vol. **10**, no. 100073. ISSN 26662027. Available from: <https://doi.org/10.1016/j.ijft.2021.100073>

List of Figures

Figure 1: Timeline summarising the use of nanomaterials during ancient times [2].....	14
Figure 2: SEM image of the IBM logo composed of xenon atoms [5].....	15
Figure 3: Dimensionality classification of nanostructures [12].....	19
Figure 4: Schematic of hexagonal graphene lattice [15].	21
Figure 5: Exfoliation of graphene sheets [23].....	22
Figure 6: Example of the CVD procedure for graphene synthesis [36].....	24
Figure 7: Example of the CVD procedure for graphene synthesis [41].....	25
Figure 8: Controlled nanotube structures: A) aligned CNT arrays; B) 3D MWCNT pattern – Daisies [43].	26
Figure 9: Scheme of the electric-arc method [42].	27
Figure 10: Scheme of the laser ablation method [42].....	27
Figure 11: Scanning electron microscopy (SEM) images of porous CN [47].	28
Figure 12: Agglomeration of CNTs in aqueous solution.	29
Figure 13: Principle of the ball milling technique [56].	30
Figure 14: Schematic of rotor-stator type homogenizer [72].	31
Figure 15: Schematic showing non-covalent and covalent surface modification of carbon nanomaterials [75].....	32
Figure 16: Structure of surfactants [74].....	33
Figure 17: Variation of compressive strength of GO-cement mortar with different GO contents (0-0.5 %) [104].	37
Figure 18: Particle size distribution measured by laser diffraction.....	45
Figure 19: Particle size distribution of silica sand aggregate.....	46
Figure 20. TEM micrograph of MWCNTs and GNs [115].	47
Figure 21: TEM micrograph of CSs [117].....	48
Figure 22: Schematic of the antifoams bridging-stretching mechanism [127].....	50
Figure 23: Preparation of composites: A) graphene dispersion in MgCl ₂ solution; B) mixing of paste; C) second step of homogenization using Ultra-Turrax.	51
Figure 24: Photograph of the prepared prismatic specimens of a) MOC-REF; b) MOC-G0.2; c) MOCG0.5 and d) MOC-G1.0.	53
Figure 25: A) CSs powder; B) hardened prismatic samples of MOC mortars.....	55
Figure 26: Absorbance spectra of GNs with different specific surface areas.....	56
Figure 27: Agglomeration of suspension of A) non-modified and B, C) modified MWCNTs.....	57
Figure 28: Results of the foamability test.	59

Figure 29: Absorbance spectra of GNs dispersed with an ultrasonic bath.	60
Figure 30: Absorbance spectra of GNs dispersed with a high-shear mixer.	60
Figure 31: Absorbance spectra of MWCNTs dispersed with an ultrasonic bath.	61
Figure 32: Absorbance spectra of MWCNTs dispersed with a high-shear mixer.	61
Figure 33: Absorbance spectra of CSs dispersed with an ultrasonic bath.	62
Figure 34: Absorbance spectra of CSs dispersed with a high-shear mixer.	62
Figure 35: Photograph of HL-CNT samples.	67
Figure 36: Analysette 22 Micro Tec plus particle size distribution analyser.	69
Figure 37: Automatic Blain’s air permeability apparatus.	70
Figure 38: ARLTM QUANT’X EDXRF Spectrometer, Thermo Scientific.	71
Figure 39: UV-Vis spectrophotometer (A) and cuvettes (B).	73
Figure 40: Foam formation during foamability test (A) and foam-free solution (B).	73
Figure 41: X-Ray powder diffraction apparatus.	75
Figure 42: FTIR spectrometer Nicolet 6700.	75
Figure 43: Flow table test.	77
Figure 44: Helium pycnometer Pycnomatic ATC.	78
Figure 45: MIP apparatus Pascal 140 and 440.	79
Figure 46: Flexural strength A) and compressive strength B) testing setup.	80
Figure 47: Ultrasonic data logger – Vikasonic.	81
Figure 48: Hot-Disk apparatus setup.	82
Figure 49: Water absorption measurement.	83
Figure 50: XRD analysis: A) MOC-REF, B) MOC-G, and C) MOC-G-H.	86
Figure 51: Micrographs of samples: A) MOC-REF, B) MOC-G, and C) MOC-G-H.	87
Figure 52: EDS elemental maps of the samples: A) MOC-REF, B) MOC-G, and C) MOC-G-H.	88
Figure 53: The MIR (Mid-infrared) spectra of MOC-REF, MOC-G3 and MOC-G-H.	89
Figure 54: Two-step homogenization: Incremental pore volume distribution for 14-day composites.	91
Figure 55: Two-step homogenization: Cumulative distribution of the pore volume for 14-day composites.	92
Figure 56: Mechanical strength: A) compressive strength of 7-day samples; B) compressive strength of 28-day samples; C) flexural strength of 7-day samples; D) flexural strength of 28-day samples.	93
Figure 57: Two-step homogenization: Cost-effectivity ratio.	94
Figure 58: XRD analysis: A) MOC-REF; B) MOC-G300 and C) MOC-G750.	95
Figure 59: Micrographs of samples: MOC-REF, MOC-G300, and MOC-G750.	96

Figure 60: EDS elemental maps of the samples: MOC-REF, MOC-G300 and MOC-G750.	97
Figure 61: NM's specific surface area: Incremental pore volume distribution for 14-day composites.	99
Figure 62: NM's specific surface area: Cumulative distribution of the pore volume for 14-day composites.	99
Figure 63: Mechanical strength: A) compressive strength of 7-day samples; B) compressive strength of 28-day samples; C) flexural strength of 7-day samples; D) flexural strength of 28-day samples.	100
Figure 64: NM's specific surface area: Cost-effectivity ratio.....	101
Figure 65: XRD analysis: A) MOC-REF, B) MOC-G0.2, and C) MOC-G0.5 and D) MOC-G1.0.	102
Figure 66: Micrographs of samples: MOC-REF, MOC-G0.2; MOC-G0.5 and MOC-G1.0.	103
Figure 67: EDS elemental maps of the samples: MOC-REF, MOC-G0.2; MOC-G0.5 and MOC-G1.0.....	104
Figure 68: The MIR (Mid-infrared) spectra of MOC-REF, MOC-G0.2; MOC-G0.5 and MOC-G1.0.....	105
Figure 69: NM's volume: Cumulative (top) and incremental (bottom) pore size distribution curves.	106
Figure 70: NM's volume: Flexural strength of hardened composites.....	107
Figure 71: NM's volume: Compressive strength of hardened composites.....	108
Figure 72: NM's volume: Cost-effectivity ratio.....	109
Figure 73: The elemental composition: MOC co-doped with non-functionalized NMs:	110
Figure 74: The elemental composition: MOC co-doped with functionalized NMs:.....	110
Figure 75: The elemental maps of MOC surface modified with functionalized NMs. .	111
Figure 76: Co-doped MOC: Mechanical strength of hardened composites.	112
Figure 77: Co-doped MOC: Cost-effectivity ratio.	114
Figure 78: SEM/EDS analysis of Carbon Spheres (CSs).....	115
Figure 79: The MIR (Mid-infrared) spectra of MOC-CS pastes.	115
Figure 80: SEM micrograph of MOC-REF and MOC-CS-3.0	116
Figure 81: Carbon spheres additive: a) Cumulative and b) incremental pore size distribution curves.	117
Figure 82: Carbon spheres additive: Compressive strength of hardened mortars.....	118
Figure 83: Carbon spheres additive: Cost-effectivity ratio.....	119
Figure 84: Elemental maps of the MOC-REF mixture.	121

Figure 85: Elemental maps of the MOC-G0.3 mixture.	122
Figure 86: Elemental maps of the MOC-S0.3 mixture.....	122
Figure 87: MOC mixtures: Flexural strength parameters.	124
Figure 88: MOC mixtures: Compressive strength parameters.	124
Figure 89: MOC mixtures: Cost-effectivity ratio.	126
Figure 90: Elemental maps of the CL-REF mixture.....	127
Figure 91: Elemental maps of the CL-CNT0.5 mixture.	127
Figure 92: Elemental maps of the CL-S0.3 mixture.	128
Figure 93: CL mixtures: Flexural strength parameters.	130
Figure 94: CL mixtures: Compressive strength parameters.	130
Figure 95: CL mixtures: Cost-effectivity ratio.	132
Figure 96: Elemental maps of the HL-REF mixture.....	133
Figure 97: Elemental maps of the HL-G0.1 mixture.....	133
Figure 98: HL mixtures: Flexural strength parameters.	135
Figure 99: HL mixtures: Compressive strength parameters.	136
Figure 100: HL mixtures: Cost-effectivity ratio.	138

List of Tables

Table 1: Overview of the most common methods of nanomaterial dispersion techniques.	30
Table 2: A selection of studies dealing with surfactant-aided NM dispersion.	34
Table 3: A selection of studies dealing with cement-based composites with variable concentration of NMs.	36
Table 4: A selection of studies dealing with nano-modified lime-based mortars.	38
Table 5: Chemical composition of the studied binders.	44
Table 6: Specifications of studied graphene NMs [112, 113].	46
Table 7: Specifications of studied MWCNTs [114].	47
Table 8: Specifications of studied CSs [116].	48
Table 9: Specification of used surfactants [118–123].	49
Table 10: Two-step homogenization - mixture composition (in $\text{kg}\cdot\text{m}^{-3}$).	52
Table 11: Specific surface area - mixture composition (in $\text{kg}\cdot\text{m}^{-3}$).	52
Table 12: Nanomaterial dosage - mixture composition (in $\text{kg}\cdot\text{m}^{-3}$).	53
Table 13: Co-doped non-functionalized NMs - mixture composition (in $\text{kg}\cdot\text{m}^{-3}$).	54
Table 14: Co-doped functionalized NMs - mixture composition (in $\text{kg}\cdot\text{m}^{-3}$).	54
Table 15: Carbon spheres nano-additive - mixture composition (in $\text{kg}\cdot\text{m}^{-3}$).	55
Table 16: Characteristics of lime pastes with different surface modifications [133].	58
Table 17: Foamability test results.	58
Table 18: Solutions designed for NM dispersion (in g).	59
Table 19: Characteristics of composites with varying volumes of MOC paste volume.	64
Table 20: Composition of magnesium oxychloride cement (MOC) mortars.	64
Table 21: Composition of hydrated lime (CL) mixtures (in $\text{kg}\cdot\text{m}^{-3}$).	65
Table 22: Composition of natural hydraulic lime (HL) mixtures (in $\text{kg}\cdot\text{m}^{-3}$).	66
Table 23: Methodology of raw materials tests performed.	68
Table 24: Methodology of performed NM suspension tests.	72
Table 25: List of the experimental tests performed.	74
Table 26: Assignments of the major absorption bands of MOC composites.	90
Table 27: Two-step homogenization: Basic structural parameters of 7-days cured pastes.	90
Table 28: Two-step homogenization: Basic structural parameters of 14-days cured pastes.	91
Table 29: Two-step homogenization: Microstructural parameters of the 14-day composites.	92

Table 30: Two-step homogenization: Cost-effectivity of additive.....	94
Table 31: NM's specific surface area: Basic structural parameters of 7-days cured pastes.	98
Table 32: NM's specific surface area: Basic structural parameters of 14-days cured pastes.	98
Table 33: NM's specific surface area: Microstructural parameters of the 14-day composites.	98
Table 34: NM's specific surface area: Cost-effectivity of additive.....	101
Table 35: NM's volume: Basic structural parameters of pastes.....	105
Table 36: NM's volume: Microstructural parameters of hardened composites.	107
Table 37: NM's volume: Mechanical strength of hardened composites.....	107
Table 38: NM's volume: Hygric and thermal properties of hardened composites.	108
Table 39: NM's volume: Cost-effectivity of additive.....	109
Table 40: Co-doped MOC: Basic structural properties of pastes.	111
Table 41: Co-doped MOC: Mechanical strength parameters.	112
Table 42: Co-doped MOC: Hygric properties of hardened composites.	113
Table 43: Co-doped MOC: Thermal properties of hardened composites.	113
Table 44: Co-doped MOC: Cost-effectivity of additive.	114
Table 45: Carbon spheres additive: Basic structural properties of composites.	117
Table 46: Carbon spheres additive: Microstructural parameters of hardened composites.	117
Table 47: Carbon spheres additive: Mechanical strength characteristics.	118
Table 48: Carbon spheres additive: Hygric properties of hardened composites.....	119
Table 49: Carbon spheres additive: Cost-effectivity of the additive.....	120
Table 50: MOC mixtures: Basic structural properties.....	123
Table 51: MOC mixtures: Mechanical strength characteristics.	123
Table 52: MOC mixtures: Heat transfer characteristics.....	125
Table 53: MOC mixtures: Cost-effectivity of the additive.....	126
Table 54: CL mixtures: Basic structural properties.....	128
Table 55: CL mixtures: Mechanical strength characteristics.	129
Table 56: CL mixtures: Heat transfer characteristics.	131
Table 57: CL mixtures: Cost-effectivity of the additive.	132
Table 58: HL mixtures: Basic structural properties.....	134
Table 59: HL mixtures: Mechanical strength characteristics.	135
Table 60: HL mixtures: Heat transfer characteristics.	137
Table 61: HL mixtures: Cost-effectivity of the additive.	137
Table 62: Optimal nano-additive for individual mortars.	139

List of published papers within the researched projects

- [1] LAUERMANNOVÁ, A.-M. et al. MOC Composites for Construction: Improvement in Water Resistance by Addition of Nanodopants and Polyphenol. *Polymers*, **15**, 2023. ISSN 2073-4360.
DOI: 10.3390/polym15214300
- [2] ZÁLESKÁ, M. et al. The Influence of 1D and 2D Carbon Nanomaterials on Properties of Magnesium Oxychloride Cement Mortars. *Proceedings of 23rd International Multidisciplinary Scientific GeoConference SGEM 2023*, vol. **23**, Albena, 2023. ISSN 1314-2704. ISBN 978-619-7603-61-3.
DOI: 10.5593/sgem2023/6.1/s26.43
- [3] JANKOVSKÝ, O. et al. Case study on nanoscale modification of MOC-based construction composites: Introduction of molybdenum disulfide. *Case Studies in Construction Materials*, **19**, 2023. ISSN 2214-5095.
DOI: 10.1016/j.cscm.2023.e02495
- [4] PIVÁK, A. et al. Effect of Water Vapor Adsorption Capacity on Thermal Properties of Lime Mortars doped with Graphene Nanoplatelets. *AIP Conference Proceedings. Thermophysics 2022, Dalešice, 2023*. ISBN 9780735446557.
DOI: 10.1063/5.0163721
- [5] Lauermannova, A.-M.; Lojka, M.; Faltysová, I.; Pavlík, Z.; Pavlíková, M.; Pivák, A.; Záleská, M.; Jankovský, O. Magnesium Oxychloride Cement Composites Filled with Martian Soil Simulant. *AIP Conference Proceedings*, **1**, 2023.
DOI: 10.1063/5.0163742
- [6] KAPICOVÁ, A. et al. Influence of different surfactants on hydrated lime pastes modified with CNTs. *International Conference of Numerical Analysis and Applied Mathematics ICNAAM 2021*. Rhodes, 2023. ISSN 1551-7616. ISBN 978-0-7354-4589-5.
DOI: 10.1063/5.0162199
- [7] PIVÁK, A. et al. Lime mortars doped with graphene nanoplatelets. *International Conference of Numerical Analysis and Applied Mathematics ICNAAM 2021*. Rhodes, 2023. ISSN 1551-7616. ISBN 978-0-7354-4589-5.
DOI 10.1063/5.0162234
- [8] JIŘIČKOVÁ, A. et al. Utilization of waste carbon spheres in magnesium oxychloride cement. *Case Studies in Construction Materials*. **19**, 2023. ISSN 2214-5095.
DOI: 10.1016/j.cscm.2023.e02374

- [9] PAVLÍK, Z. et al. Utilization of extracted carbonaceous shale waste in eco-friendly cementitious blends. *Construction and Building Materials*, **394**, 2023. ISSN 0950-0618. DOI: 10.1016/j.conbuildmat.2023.132069
- [10] LAUERMANNNOVA, A.-M. et al. Magnesium oxychloride cement-based composites for latent heat storage: The effect of the introduction of multi-walled carbon nanotubes. *Journal of Building Engineering*. **72**, 2023. ISSN 2352-7102. DOI: 10.1016/j.job.2023.106604
- [11] PAVLÍKOVÁ, M. et al. High-Performance MOC Composite Doped with Carbon-Based Nanoadditive. *Proceedings of 22nd International Multidisciplinary Scientific GeoConference SGEM 2022*. Albena, 2022. ISSN 1314-2704. DOI: 10.5593/sgem2022/6.1/s26.21
- [12] PIVÁK, A. et al. Macro-Mechanical and Micro-Mechanical Properties of Nano-Enhanced Magnesium Oxychloride Cement. *Proceedings of 22nd International Multidisciplinary Scientific GeoConference SGEM 2022*, Albena, 2022. ISSN 1314-2704. DOI: 10.5593/sgem2022/6.1/s26.22
- [13] LAUERMANNNOVÁ, A.-M. et al. Graphene- and MWCNT-reinforced magnesium oxychloride composite modified by tannic acid. *FlatChem*, **37**, 2023. ISSN 2452-2627. DOI: 10.1016/j.flatc.2022.100459
- [14] PAVLÍK, Z. et al. Enhancement of Structural and Mechanical Properties of Magnesium Oxychloride Cement Due to Graphene Addition. *INTERNATIONAL CONFERENCE OF NUMERICAL ANALYSIS AND APPLIED MATHEMATICS ICNAAM 2020*, Rhodes, 2022. ISSN 1551-7616. ISBN 978-0-7354-4182-8. DOI 10.1063/5.0081391
- [15] LAUERMANNNOVÁ, A.-M. et al. Magnesium oxychloride-graphene composites: Towards high strength and water resistant materials for construction industry. *FlatChem*, **29**, 2021. ISSN 2452-2627. DOI: 10.1016/j.flatc.2021.100284
- [16] PAVLÍKOVÁ, M. et al. Ultra-high strength multicomponent composites based on reactive magnesia: Tailoring of material properties by addition of 1D and 2D carbon nanoadditives. *Journal of Building Engineering*, **50**, 2022. ISSN 2352-7102. DOI: 10.1016/j.job.2022.104122
- [17] LAUERMANNNOVÁ, A.-M. et al. Co-Doped Magnesium Oxychloride Composites with Unique Flexural Strength for Construction Use. *Materials*, **15**, 2022. ISSN 1996-1944. DOI: 10.3390/ma15020604

- [18] PAVLÍKOVÁ, M. et al. Effect of mixture preparation technique on properties of graphene doped MOC. *21th International Multidisciplinary Scientific Geoconference SGEM 2021 Conference Proceedings*, 2021, Albena. ISSN 1314-2704. ISBN 978-619-7603-30-9.
DOI: 10.5593/sgem2021/6.1/s26.44.
- [19] LAUERMANNNOVÁ, A.M. et al. The influence of graphene specific surface on material properties of MOC-based composites for construction use. *Journal of Building Engineering*, **43**, 2021. ISSN 2352-7102.
DOI: 10.1016/j.jobbe.2021.103193
- [20] ZÁLESKÁ, M. et al. MOC Doped with Graphene Nanoplatelets: The Influence of the Mixture Preparation Technology on Its Properties. *Materials*, **14**, 2021. ISSN 1996-1944. DOI: 10.3390/ma14061450
- [21] LAUERMANNNOVÁ, A.M. et al. Regolith-based magnesium oxychloride composites doped by graphene: Novel high-performance building materials for lunar constructions. *FlatChem*, **26**, 2021. ISSN 2452-2627.
DOI: 10.1016/j.flatc.2021.100234
- [22] LAUERMANNNOVÁ, A.M. et al. Graphene- and graphite oxide-reinforced magnesium oxychloride cement composites for the construction use. *Ceramics-Silikáty*, **65**, 2021. ISSN 1804-5847.
DOI: 10.13168/cs.2020.0040
- [23] LOJKA, M. et al. Magnesium Oxychloride Cement Composites with MWCNT for the Construction Applications. *Materials*, **14**, 2021. ISSN 1996-1944.
DOI: 10.3390/ma14030484
- [24] JANKOVSKÝ, O. et al. Towards novel building materials: High-strength nanocomposites based on graphene, graphite oxide and magnesium oxychloride. *Applied Materials Today*, **20**, 2020, ISSN 2352-9407.
DOI: 10.1016/j.apmt.2020.100766
- [25] ZÁLESKÁ, M. et al. Influence of Graphite Oxide Addition on the Properties of Magnesium Oxychloride Cement Composites. *IOP Conference Series: Materials Science and Engineering. 5th World Multidisciplinary Civil Engineering-Architecture-Urban Planning Symposium – WMCAUS*, Prague, 2020. ISSN 1757-899X.
DOI: 10.1088/1757-899X/960/2/022080
- [26] LAUERMANNNOVÁ, A.-M. et al. The impact of graphene and diatomite admixtures on the performance and properties of high-performance magnesium oxychloride cement composites. *Materials*, **13**, 2020. ISSN 1996-1944.
DOI: 10.3390/ma13245708